
Numerical Methods for 3D Magneto-Rotational Core-Collapse Supernova Simulation with Jet Formation

Inauguraldissertation

zur

Erlangung der Würde eines Doktors der Philosophie
vorgelegt der
Philosophisch-Naturwissenschaftlichen Fakultät
der Universität Basel

von

Roger Yves Käppeli

aus Wynau, BE

Basel, 2013

Originaldokument gespeichert auf dem Dokumentenserver der Universität Basel
edoc.unibas.ch



Dieses Werk ist unter dem Vertrag „Creative Commons Namensnennung-Keine
kommerzielle Nutzung-Keine Bearbeitung 2.5 Schweiz“ lizenziert. Die vollständige Lizenz
kann unter

creativecommons.org/licenses/by-nc-nd/2.5/ch
eingesehen werden.

Genehmigt von der Philosophisch-Naturwissenschaftlichen Fakultät
auf Antrag von

Prof. Dr. Friedrich-Karl Thielemann

Prof. Dr. Matthias Liebendörfer

Prof. Dr. Siddartha Mishra

Basel, den 15. November 2011

Prof. Dr. Martin Spiess



Namensnennung-Keine kommerzielle Nutzung-Keine Bearbeitung 2.5 Schweiz

Sie dürfen:



das Werk vervielfältigen, verbreiten und öffentlich zugänglich machen

Zu den folgenden Bedingungen:

Namensnennung. Sie müssen den Namen des Autors/Rechteinhabers in der von ihm festgelegten Weise nennen (wodurch aber nicht der Eindruck entstehen darf, Sie oder die Nutzung des Werkes durch Sie würden entlohnt).

Keine kommerzielle Nutzung. Dieses Werk darf nicht für kommerzielle Zwecke verwendet werden.

Keine Bearbeitung. Dieses Werk darf nicht bearbeitet oder in anderer Weise verändert werden.

- Im Falle einer Verbreitung müssen Sie anderen die Lizenzbedingungen, unter welche dieses Werk fällt, mitteilen. Am Einfachsten ist es, einen Link auf diese Seite einzubinden.
- Jede der vorgenannten Bedingungen kann aufgehoben werden, sofern Sie die Einwilligung des Rechteinhabers dazu erhalten.
- Diese Lizenz lässt die Urheberpersönlichkeitsrechte unberührt.

Die gesetzlichen Schranken des Urheberrechts bleiben hiervon unberührt.

Die Commons Deed ist eine Zusammenfassung des Lizenzvertrags in allgemeinverständlicher Sprache: <http://creativecommons.org/licenses/by-nc-nd/2.5/ch/legalcode.de>

Haftungsausschluss:

Die Commons Deed ist kein Lizenzvertrag. Sie ist lediglich ein Referenztext, der den zugrundeliegenden Lizenzvertrag übersichtlich und in allgemeinverständlicher Sprache wiedergibt. Die Deed selbst entfaltet keine juristische Wirkung und erscheint im eigentlichen Lizenzvertrag nicht. Creative Commons ist keine Rechtsanwalts-gesellschaft und leistet keine Rechtsberatung. Die Weitergabe und Verlinkung des Commons Deeds führt zu keinem Mandatsverhältnis.

Dedicated to my mother Maya, father Max, brother Pascal and my dogs Jones & Benji

Abstract

The work presented in this thesis is devoted to the development of a numerical model for the three dimensional simulation of magneto-rotational core-collapse supernovae (MHD-CCSNe) with jet formation. The numerical model then suggests that MHD-CCSNe naturally provide a possible site for the strong rapid neutron capture process in agreement with observations of the early Galactic chemical evolution.

In the first part of this thesis, we develop several numerical methods and describe thoroughly their efficient implementations on current high-performance computer architectures. We develop a fast and simple computer code FISH that solves the equations of magnetohydrodynamics. The code is parallelized with an optimal combination of shared and distributed memory paradigms and scales to several thousands processes on high-performance computer clusters. We develop a novel well-balanced numerical scheme for the Euler equations with gravitational source terms to preserve a discrete hydrostatic equilibrium exactly. Being able to accurately represent hydrostatic equilibria is of particular interest for the simulation of CCSN, because a large part of the newly forming neutron star evolves in a quasi-hydrostatic manner. We include an approximate and computationally efficient treatment of neutrino physics in the form of a spectral leakage scheme. It enables us to capture approximately the most important neutrino cooling effects, which are responsible for the shock stall and for the neutronisation of matter behind the shock. The latter is crucial for the nucleosynthesis yields. To fit into our multidimensional MHD-CCSN model, the spectral leakage scheme is implemented in a ray-by-ray approach.

In the second part of this thesis, we apply our three-dimensional numerical model to the study of the MHD-CCSN explosion mechanism. We investigate a series of models with poloidal magnetic field and varying initial angular momentum distribution through the collapse, bounce and jet formation phase. For all computed models, we investigate the process of magnetic field amplification, angular momentum redistribution and the formation and driving mechanism of the bipolar outflow.

In a representative model we follow the jet for a longer time and larger distance. We find that the bipolar outflow features a significant amount of very neutron rich matter and is therefore a promising site for the rapid neutron capture process (r-process). The computations show that under the prevailing conditions in the bipolarly ejected matter the global solar r-process pattern could be reproduced. The computed amount of ejected matter and peculiarity of the progenitor (featuring large enough rotation and magnetic fields to induce MHD-CCSN explosion mechanism) indicates that only a fraction (perhaps 0.1 - 1%) of CCSN explode with the MHD mechanism. This is also in agreement with the observed large star-to-star scatter of r-process element abundances in very old halo stars indicating the scarcity of these events in the early Galactic chemical evolution.

Contents

1	Introduction	1
1.1	Supernovae	1
1.2	Core-collapse Supernovae	2
1.2.1	Stellar evolution and progenitor structure	2
1.2.2	Core collapse and core bounce	5
1.2.3	From core bounce to explosion	6
1.3	Physical and mathematical model description of the problem	8
2	Numerical methods & implementations	15
2.1	Numerical solution of the ideal MHD equations: the FISH code	15
2.1.1	The equations of ideal MHD	15
2.1.2	Numerical solution of the MHD equations	16
2.1.3	Solving the fluid MHD equations	17
2.1.4	Divergence preserving advection of the magnetic field	20
2.1.5	Gravitational source terms integration	23
2.1.6	Generalisation to non-uniform meshes	24
2.1.7	Efficient parallel implementation	25
2.1.8	Numerical results	32
2.2	Well-balanced methods for hydrostatic equilibrium	43
2.2.1	First order one-dimensional schemes	45
2.2.2	Numerical fluxes: approximate solution of the Riemann problem	46
2.2.3	Well-balanced local hydrostatic reconstruction and source term discretisation	48
2.2.4	Second order one-dimensional schemes: higher order hydrostatic reconstruction	51
2.2.5	Extension beyond one dimension	52
2.2.6	Extension to general equation of states and MHD: approximately-balanced schemes	54
2.2.7	Numerical results	55
2.3	Gravitation	62
2.3.1	Gravity in spherical symmetry and general relativistic corrections	63
2.3.2	Gravity in cylindrical coordinates and axisymmetry	65
2.4	Tracer particles	67
2.4.1	Time integration	68
2.4.2	Spatial interpolation	68
2.4.3	Verification	69
2.4.4	Parallel implementation	70

2.5	Angular momentum and magnetic field boundary conditions	71
2.5.1	Evolution of rotation	72
2.5.2	Evolution of the magnetic field	74
2.6	Electron neutrino leakage scheme in 3D	76
2.6.1	Verification of the implementation	78
3	Simulation of Magneto-Rotational Core-Collapse	83
3.1	Introduction	83
3.2	Initial setup and model parameters	84
3.3	Numerical results	87
3.3.1	Global dynamics	87
3.3.2	Magnetic field amplification	90
3.3.3	Formation and driving mechanism of bipolar outflow	95
3.3.4	Explosion energy, ejected mass and its composition	97
4	Summary and conclusions	101
	Bibliography	105
	Curriculum Vitae	117
	Acknowledgements	119

Chapter 1

Introduction

1.1 Supernovae

Supernovae (SNe) are among nature's most spectacular and energetic events. In the course of such an event, a single star can briefly outshine its entire host galaxy. Owing to their brightness, early astronomers have observed nearby SNe by the naked eye. They have been termed as 'guest stars' due to their sudden appearance and fade out. Two prominent examples being the SN of Tycho Brahe in AD 1572 and Johannes Keppler in AD 1604. Their detailed observation led to the conclusion that they were beyond the moon's orbit, contributing to the overthrow of the Aristotelian worldview that included immutable heavens. These so-called 'historical' SNe are also the last ones observed in our galaxy.

In 1934, the fact that two energy scales became apparent in the observation of new stars or novae, a sudden burst in luminosity that slowly decays, led the two astronomers Walter Baade and Fritz Zwicky introduce the distinguishing terminology of common novae and SNe [9, 10]. The later being orders of magnitudes brighter and much less frequent. The high luminosities of SNe and the broad lines in their spectra brought them to the correct conclusion that SNe were very energetic explosions. Even further, the physicist hypothesized that "... a super-nova represents the transition of an ordinary star into a neutron star" [9]. This picture turned out to be correct and is still in the fundamentals of modern theoretical models of SNe resulting from the gravitational collapse of massive stars. The fact that this hypothesis emerged only shortly after the discovery of the neutron by James Chadwick in 1932 [36] further underlines its remarkable character.

From an observational point of view, SNe have been divided into two distinct types by R. Minkowski in the early forties of last century. SNe are distinguished by the absence (Type I) or presence (Type II) of hydrogen Balmer lines in their spectra. Since then, with an increasing number of observations and more sophisticated photometry, sub-types were introduced (see figure 1.1):

Type Ia: Type Ia SNe spectra are distinguished by a strong absorption attributed to Si II and absent hydrogen Balmer lines.

Type Ib: Type Ib SNe are characterized by spectra with no evident hydrogen Balmer lines, weak or absent Si II lines and strong He I lines.

Type Ic: Type Ic SNe are distinguished by weak or absent hydrogen Balmer lines, weak or absent Si II lines and weak or absent helium lines.

Type II: Type II SNe have prominent hydrogen Balmer lines.

Further classification of SNe is also performed on their light curve. See e.g. [47, 60, 163] and references therein for further details. Type II, Ib and Ic occur near star forming regions and have never been observed in elliptical galaxies (with no or negligible star formation). On the other hand, type Ia SNe are observed in all types of galaxies [60]. A distinguishing feature of type Ia SNe is the similarity of their light curves which can be standardised according to the Philips relation [129]. This makes them candidates for so-called standard candles which can be used for measuring distances and probing the curvature of the universe.

From a theoretical point of view, two fundamentally different SN types can be distinguished based on the physical mechanism of the explosion: core-collapse and thermonuclear SNe. The lifetime and the final fate of a star is intimately linked to its mass and chemical composition at birth. Massive stars with $M \gtrsim 8M_{\odot}$ go through all nuclear burning stages up to iron beyond which nuclear fusion would be endothermic. Having exhausted the nuclear fuel in their centres, massive stars undergo gravitational collapse of their cores, leaving behind compact remnants in the form of neutron stars or black holes, and expel their envelopes in a grand explosion. The gravitational energy liberated during the core's collapse is the energy source for the explosion.

Stars with masses $M \lesssim 8M_{\odot}$ are not massive enough to ignite carbon/oxygen burning and become carbon-oxygen white dwarfs. A small subset of white dwarfs may be situated in tight binaries with a normal stellar or white dwarf companion [68]. If sufficient matter originating from a companion star is accreted onto the white dwarf to push it over the Chandrasekhar mass limit for a relativistic degenerate electron gas, then a contraction is issued. This contraction ignites the carbon and oxygen leading to a thermonuclear incineration of the white dwarf. No remnant is left behind.

SNe are also crucial for the dynamical and the chemical evolution of the Universe. Indeed, many elements necessary for the development of life are synthesised during these explosive events. For example, the oxygen ejected during core-collapse supernovae is the dominant source of that element in the universe [29].

In this thesis we will exclusively be concerned with core-collapse SNe (hereafter CCSN), i.e. type Ib, Ic and II SNe.

1.2 Core-collapse Supernovae

1.2.1 Stellar evolution and progenitor structure

Much like living beings, stars are born, have a shiny nuclear burning life, and die, leaving behind tiny fossils. A star's life begins as a cloud of material with a mass $\gtrsim 0.075M_{\odot}$ [35, 31], composed primarily of hydrogen, along with helium and traces of heavier elements, collapsing under the pull of its self-gravity/own gravitational force. As the cloud collapses the density increases, the gravitational energy is converted into heat and the temperature rises. Eventually, the temperature reaches values above 2×10^7 K igniting hydrogen burning. The onset of nuclear burning then halts further compression by gravity and hydrostatic equilibrium sets in. With the exhaustion of core hydrogen burning, most stars transition to shell hydrogen burning and eventually the core is compressed enough to start helium fusion. The ashes of helium burning are mostly carbon and oxygen.

So far, the exhaustion of one fuel, led to the ignition of the next. However, low initial mass stars ($\lesssim 6-8M_{\odot}$) are not massive enough to contract to sufficiently high densities and

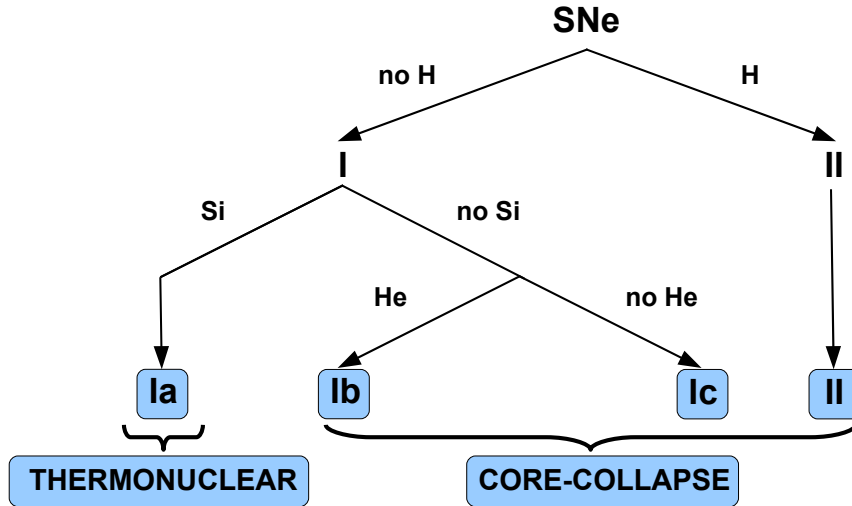


Figure 1.1: Classification scheme for Supernovae [47, 60, 163]. The two main classes are discerned on the basis of the absence (Type I) or presence (Type II) of hydrogen Balmer lines in their spectra. Class I is then further subdivided based on the presence (Ia) or absence (Ib, Ic) of Si lines. Type Ib and Ic are distinguished by the occurrence of He I lines (Ib) or not (Ic.) Regardless of the spectral signature, two fundamentally different SN types can be distinguished based on the driving mechanism of the explosion: core-collapse (SN II,Ib/c) and thermonuclear (SN Ia).

temperatures for carbon burning. This type of stars develop electron-degenerate carbon-oxygen (C/O) cores. After shedding of their envelopes, forming planetary nebulae, they leave behind their C/O cores, which form the remnant white dwarfs [63].

For more massive stars, contraction leads to the ignition of carbon burning which produces oxygen, neon and magnesium (O/Ne/Mg) ashes. For stars in the initial mass range of $8 - 10M_{\odot}$, core temperatures are too low to ignite subsequent nuclear burning stages. In this intermediate mass range, the stars either lose their envelopes and become O/Ne/Mg white dwarfs or proceed to core-collapse as described below for more massive stars [63].

Massive stars with initial masses higher than $10M_{\odot}$ are able by further contraction to ignite successive burning stages at their centres using the ashes of the previous stages as fuel for the next [177]. Three distinct burning stages follow carbon burning: neon, oxygen and silicon. Of these, only oxygen burning occurs by fusion reactions, while neon and silicon burning require the partial photo-disintegration of the fuel by thermal photons. Silicon burns to iron-group nuclei, where the nuclear binding energy per nucleon reaches its maximum (see e.g. [130]). Therefore, silicon burning is the last exothermic fusion reaction.

At the end of thermonuclear life, massive stars have an onion-skin like structure in which an iron core is nested within shells consisting of elements of successively lower atomic weight at gradually lower densities and temperatures. This is sketched in figure 1.2. A typical nesting of shells is Fe, Si, O/C, He and H. These shells are not pure, but are mixtures of several elements and isotopes, with the most abundant element giving the name.

Massive stars spend about 90% of their life time burning hydrogen and most of the rest burning helium. For a typical $15M_{\odot}$ star, hydrogen burning lasts 10 million years and

helium burning 1 million years. In contrast, the final silicon burning lasts only about 20 days. After helium burning, neutrino losses become increasingly important for the energy budget. In fact, the late burning stages of massive stars can be thought of as a neutrino mediated Kelvin-Helmholtz contraction of a carbon-oxygen core [177].

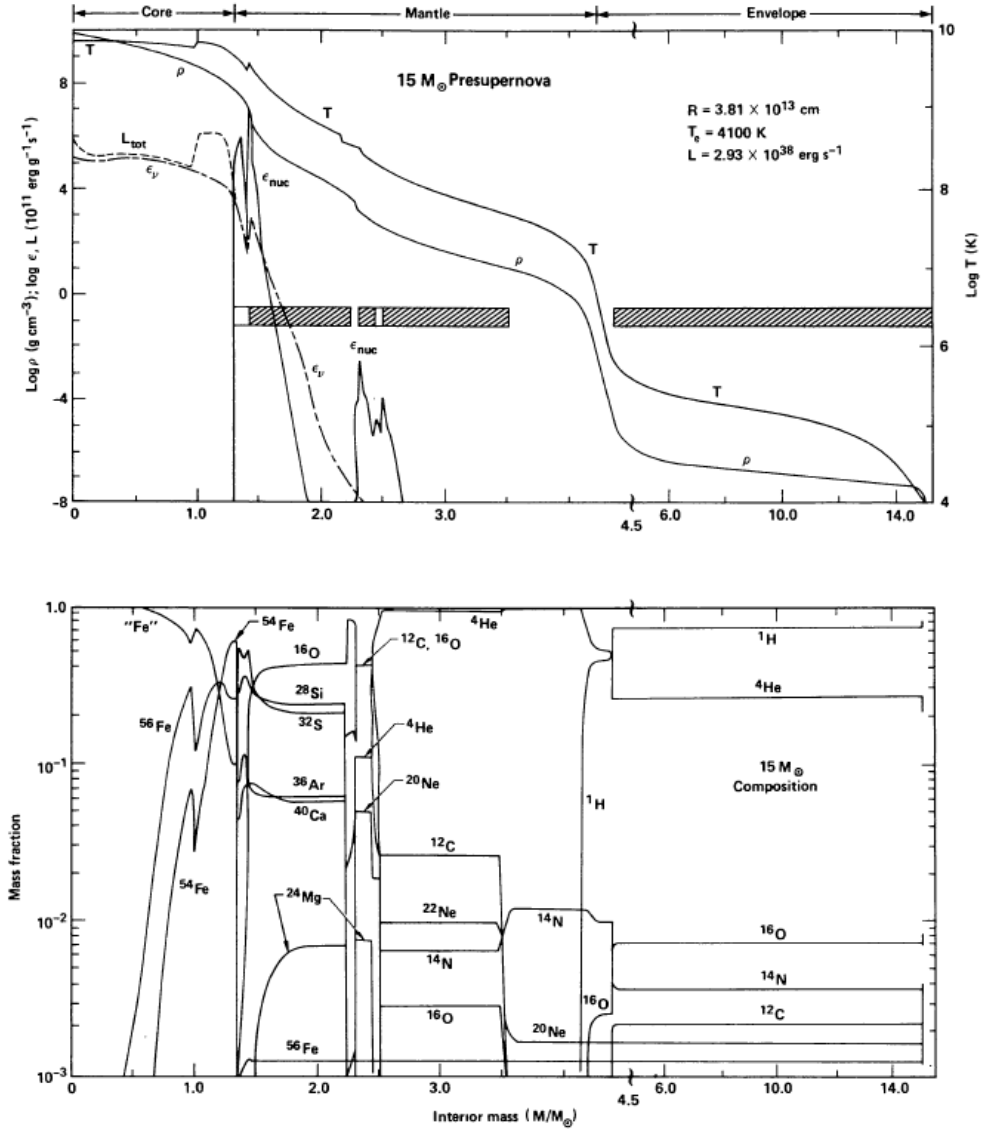


Figure 1.2: Structure of a $15M_{\odot}$ star at the onset of collapse, taken from [178]. In the upper panel, the temperature and density profiles are displayed. The energy budget is also shown, where L_{tot} is the total energy loss together with the individual contributions from neutrino emission ϵ_{ν} and from nuclear energy generation ϵ_{nuc} . The lower panel displays the composition profile, showing the onion-skin like structure of progressively lighter elements surrounding the iron core.

1.2.2 Core collapse and core bounce

As silicon core burning proceeds, its ashes, iron-group nuclei, accumulate at the centre of the star. When silicon is mostly exhausted in the centre, silicon core burning transitions into silicon shell burning.

The pile up of the ashes of silicon burning at the centre of the star produces the so-called iron core (because it mostly consists of iron-group nuclei). The iron core's resistance against gravity stems mostly from the pressure of relativistic and degenerate electrons ($\gtrsim 90\%$ [17]). This sets an upper limit to the iron core's mass for the stability against collapse: the Chandrasekhar mass limit [37]. The effective Chandrasekhar mass, corrected for non-zero temperature effects [15, 144], is given by

$$M_{\text{Ch}} = 5.83 \bar{Y}_e^2 \left(1 + \frac{\bar{s}_e}{\pi \bar{Y}_e} \right) M_{\odot}, \quad (1.1)$$

where \bar{Y}_e and \bar{s}_e are average values of electron fraction, i.e. the number of electrons per baryon, and electronic entropy per baryon in the core. For typical values of $\bar{Y}_e = 0.45$ and $\bar{s}_e = 0.52$ for a $15M_{\odot}$ star, one obtains an effective Chandrasekhar mass of $1.34M_{\odot}$. This value is close to the one inferred from figure 1.2, which was obtained by numerical stellar evolution calculations.

Eventually the iron core overshoots its Chandrasekhar mass and becomes unstable to collapse. Under the thermodynamic conditions in the iron core, the onset of infall is accelerated by two other processes: electron capture and photo-disintegration. At typical densities ($\gtrsim 10^9 \text{ g/cm}^3$), electron capture on Fe nuclei occurs mostly by



because the Fermi energy of electrons $\mu_e = 11.1 \text{ MeV} (\rho_{10} Y_e)^{1/3}$ [78] exceeds the mass difference between the two nuclei $m_{\text{Mn}} - m_{\text{Fe}} = 3.7 \text{ MeV}$. Here ρ_{10} is the density in units of 10^{10} g/cm^3 . This saps electrons, which supply most of the pressure that holds the iron core up¹.

Concurrently, at the prevailing high temperatures ($\gtrsim 5 \times 10^9 \text{ K}$), radiation also begins to melt down some of the iron nuclei to helium



This endothermic reaction eats up $\sim 125 \text{ MeV}$ leading to a decrease in thermal pressure support. Additionally, the internal energy produced by core contraction is consumed by this reaction.

Hence, the collapse of the iron core is unavoidable and it contracts under the pull of its self-gravity on a free-fall time scale, which is of the order $\tau \sim (G\bar{\rho})^{-1/2} \sim 0.04 \text{ s } \bar{\rho}_{10}$ ($\bar{\rho}$ is an average density over the iron core). The outer shells take no notice of the inner collapse until the supernova shock wave generated in the core hits and ejects them.

However, an important change in the collapse dynamics arises once the densities reach $\sim 10^{12} \text{ g/cm}^3$: neutrino trapping [17]. The neutrino mean free path becomes much smaller than the size of the collapsing core and they are dragged in with the collapsing matter. This implies that the total lepton fraction ($Y_l = Y_e + Y_{\nu}$) stays constant and the collapse proceeds adiabatically. Similar to the photosphere in the sun a neutrinosphere can be

¹Neutrinos escape freely when $\rho \lesssim 10^{12} \text{ g/cm}^3$.

defined as the surface, where the optical depth

$$\tau(r, E_\nu) = \int_r^\infty \frac{dr}{\lambda_\nu}, \quad (1.4)$$

becomes $2/3$. Note that the location of the neutrinosphere depends on the neutrino energy. Inside the neutrinosphere, the trapped neutrinos thermalize by neutrino-electron scattering until β equilibrium is established, i.e. the weak reactions come into equilibrium and the chemical potentials (including rest mass) of the electrons, protons, neutrons and neutrinos fulfill $\mu_e + \mu_p = \mu_n + \mu_{\nu_e}$.

Analytical studies [57, 180] and numerical simulations show that the collapsing core consists of two parts: the inner core, which is homologously collapsing $v(r) \propto r$, and the outer core, which collapses supersonically. The matter inside the sonic point, i.e. the point where the infall speed equals the speed of sound, stays in communication and collapses homologously, and the matter outside collapses in quasi free-fall. It was shown in [57] that the mass of the inner core scales approximately as $M_{\text{ic}} \propto Y_e^2$.

When the central density exceeds nuclear matter density ($\sim 3 \times 10^{14}$ g/cm³), the repulsive nuclear forces generate a sudden increase in matter pressure. At this point the inner core is undergoing a phase transition from a two phase-system of nucleons and nuclei (of the iron-group) to a one-phase system of bulk nuclear matter, i.e. one may view the inner core as one giant nucleus. This stiffening of the equation of state allows the inner core to halt the collapse and to find an equilibrium configuration. Starting at the centre of the inner core, where the density is largest, successive mass shells are stopped. Pressure waves move outward in radius and accumulate near the sonic point, where they steepen into a shock wave. Due to its inertia, the inner core overshoots its equilibrium and rebounds behind the shock wave. This is the so-called core bounce. The core bounce halts the collapse on a very short timescale of ~ 1 ms.

1.2.3 From core bounce to explosion

The bounce of the inner core generates outward directed velocities at and below the shock: an explosion shock is born. Schematically, the explosion shock is launched and energised by the rebounding inner core "piston". Initially, the energy of the shock wave is a multiple of the final observed kinetic supernova explosion energy [25, 94]. If the shock wave were to proceed without stalling, thereby expelling the outer layers of the massive star, we would have what has been called a prompt explosion [40].

While the shock propagates through the still supersonically in-falling outer core, it loses its strength to the dissociation of outer core material into nucleons. This dissociation costs ~ 8.8 MeV per nucleon or $\sim 16 \times 10^{51}$ erg/ M_\odot [5, 17]. This change in composition behind the shock results in even more energy loss, because the electron capture rate on free protons $e^- + p \rightarrow n + \nu_e$ is significantly larger than on nuclei [72]. The electron neutrinos are initially trapped, but escape when the shock passes beyond the electron neutrinosphere resulting in a further energy loss. This gives rise to the electron neutrino or neutronisation burst, where peak luminosities can easily exceed several 10^{53} erg/s for several ms. It is also the first of three neutrino signals from CCSN. Due to these losses, the shock is weakened so much, that it finally stalls and turns into an accretion shock at a radius between 100 and 200 km within 10 – 20 ms after core bounce. All current state-of-the-art simulations of core-collapse agree so far that the prompt explosion is not taking place generally (see e.g. [72] and references therein).

At the time the shock stalls, there is a central radiating object, the proto-neutron star (PNS), rapidly growing by the accretion of the in-falling stellar material and evolving to a compact remnant. This compact remnant is either a neutron star or a black hole, depending on whether the progenitor star had a mass below or above $\sim 25M_{\odot}$ [63].

The ultimate energy source in a CCSN is the $\sim 10^{53}$ erg of gravitational binding energy associated with the formation of the neutron star (as hypothesised by Baade and Zwicky). This energy is released after core bounce over a time ~ 10 s in the form of a three flavour neutrino signal. While mostly electron neutrinos are produced during collapse by electron capture, after bounce, in the hot PNS mantle, all three flavours of neutrinos and their antineutrinos are produced and emitted as the mantle cools and contracts during its Kelvin-Helmholtz cooling phase. During this phase, the neutrino luminosities are maintained at average values $\sim 10^{52}$ erg/s by mass accretion onto the PNS. The kinetic energy of in-fall is converted into thermal energy when the material hits the PNS surface. This is the second phase in CCSN neutrino emission.

After the explosion is initiated (the mechanism to be discussed below), the accretion luminosity decreases drastically. During that, the neutrino signal enters its third and last phase marked by an exponential decay of the neutrino luminosities characteristic of neutron star formation and cooling.

It remains to specify the explosion mechanism by which the liberated gravitational binding energy is transferred to the matter above the PNS resulting in the star's explosion as observed with optical telescopes. The theorist's modern quest is to determine how the stalled accretion shock is revived and converted into a supernova explosion. Currently, there exist four SNe explosion mechanisms discussed in the literature: (a) the delayed neutrino-driven mechanism, (b) the magneto-rotational mechanism, (c) the acoustic mechanism and (d) the QCD phase transition mechanism.

The delayed neutrino-driven explosion mechanism (a) is based on the fact that most of the liberated gravitational binding energy ($\sim 10^{53}$ erg) is still contained in the PNS in the form of trapped neutrinos. The idea is then, that neutrinos streaming off the neutrinosphere deposit some of their energy in the layers between the PNS and the stalled accretion shock. This occurs predominantly by charged-current ν_e and $\bar{\nu}_e$ captures on free nucleons



The resulting heating then provides sufficient thermal pressure to blow off the outer layers of the star. This mechanism was considered theoretically by Colgate & White [39] in 1966 and was later discovered numerically by Wilson [18] in 1985. Because the heating process has to operate for a few 100 ms, in order to initiate the explosion, it was termed "delayed" explosion mechanism. The delayed neutrino-driven mechanism is the so far best studied mechanism.

However, in highly sophisticated spherically symmetric models this mechanism fails in general (see [100, 72] and references therein), and succeeds only for very peculiar progenitor stars [77].

As a matter of fact, recent multi-dimensional simulations indicate that fluid instabilities between the PNS and the stalled or standing accretion shock enhance the absorption of neutrino energy. These fluid instabilities include convection [67, 73] and the so-called standing-accretion shock instability (SASI, see e.g. [107, 28, 70, 119, 139]).

However, even though there is consensus among the research groups concerning the necessity and functionality of fluid instabilities, the recent outcomes of 2D simulations performed

by different groups, applying similar input physics, but different numerical methods, do not yet converge. Models from the Florida/Oak Ridge group predict explosions ~ 300 ms after bounce [111] and models from the Garching group predict weak explosions ~ 600 ms after bounce [107]. It appears that more detailed investigations need to be performed in this respect, with a possible extension to a 3D study of the phenomenon.

The magneto-rotational mechanism (b) triggers the explosion by extracting rotational energy with the help of magnetic fields. While first numerical simulations of this mechanism have been performed 40 years ago [87], the mechanism has not attracted much attention mainly because there was no observational support for the high magnetic field strength required to trigger the explosion. Since the discovery of magnetars [44] the situation has changed and magnetic fields might play an important role in CCSN, at least for a subset. The jet-like explosion character associated with this mechanism may be linked to the observational evidence of aspherical CCSN [168]. The explosion may reach hypernova energies ($\sim 10^{52}$ erg) [30] and the mechanism may also be relevant in the context of long-soft γ -ray bursts [175]. The jets may rise on a short time scale neutron rich material from the vicinity of the PNS to the outer layers and produce favourable conditions for r-process nucleosynthesis [7].

The acoustic mechanism (c) proposed by Burrows and collaborators [33, 32] draws its energy from large-amplitude PNS pulsations excited by convection and accretion down streams from the standing accretion shock instability (SASI). The PNS pulsation continuously lose energy by the emission of strong sound waves which dissipate and deposit their energy near the shock, driving the explosion. While this mechanism triggers the explosion at relatively late times ($t \gtrsim 1$ s after bounce), it appears to be sufficiently robust to explode most massive progenitor stars. However, this mechanism has so far not been confirmed by other research groups, and there exist even strong analytical arguments against its existence [170].

The phase transition explosion mechanism (d) involves a so-called QCD phase transition of the PNS from baryonic matter to quark matter. This liberates further gravitational binding energy which powers a secondary shock wave triggering a successful hydrodynamic explosion, as reported in [55, 152] and recently also in [138, 48]. This mechanism works in spherically symmetric simulations robustly for massive stars, but requires exotic input physics.

Up to the present, there is no general agreement among theorists on a unique CCSN explosion mechanism. As a matter of fact, it may well be that a combination of mechanisms, with varying relevance, are at work depending on the progenitor structure, rotation and magnetic field. Sophisticated 3D models including general relativistic radiation magneto-hydrodynamics as well as a micro-physical equation of state (describing stellar matter at extreme conditions) and multi-dimensional progenitor models including consistently rotation and magnetic fields may be necessary for the full understanding of the CCSN problem.

1.3 Physical and mathematical model description of the problem

The theoretical understanding of the CCSN explosion mechanism is crucial for the understanding of the stellar life cycle. By their dramatic death, massive stars influence their environment by feeding energy to the interstellar gas in star forming regions and enrich the Galaxy with heavy elements. The explosion mechanism and remnant involves all four

fundamental forces of nature at extreme conditions.

A CCSN is not accessible to any kind of manipulation. Therefore, no experiments can be performed and a particular event cannot be repeated. However, given the size of the visible Universe, many particular events can be observed. Hence, theoretical understanding of CCSN has to rely on the information one can receive via electromagnetic radiation, particle radiation (e.g. from neutrinos) and eventually gravitational waves (GWs).

A theoretical understanding of CCSN is, however, not straightforward for at least two reasons. First, the CCSN explosion mechanism is occurring deep inside the massive star and only secondary observables including the asymptotic explosion energy, ejecta morphology, nucleosynthesis yields, remnant mass and proper motion, and pulsar spin and magnetic field strength are accessible by traditional means. On the other hand, neutrinos and gravitational waves (GWs) are considered as primary observables that may give access to the innermost details of the explosion mechanism. Both neutrinos and GWs give pristine information on the dynamics from the lieu where the explosion is initiated, and are hardly affected by intervening material on their way to observers on Earth. Given the difficulty in measuring both neutrino and GW signals, observers need to know what signal has to be expected, which implies already a theoretical understanding of the event. Second, the explosion happens at extreme conditions which are experimentally inaccessible in the laboratory, implying that one has to rely on extrapolation of known physics into regimes which are far beyond our well-tested laboratory knowledge.

Now, how to proceed under the difficult circumstances just described? One can construct a theoretical model incorporating all the physical processes thought to be of importance in CCSNe. Most theoretical models then involve a series of degrees of freedom in the form of model parameters. The model can then be evolved by computational means and comparing the model prediction to observations allows one then to constrain the model parameters. Furthermore, the model can be improved to achieve better and better agreement with observation. Hence, the model then links known or extrapolated physics to astronomical observations. Model design, prediction, comparison to observation and model improvement is therefore an iterative process. As in any iterative process, the time it takes to evaluate a model with a given parameter set and the associated model prediction is a crucial quantity. Indeed, the insight one can get in a predetermined time from a model depends highly on the cost of one model evaluation. Therefore, a careful choice of the included physical processes and the the complexity of their mathematical description together with the evaluation procedure is crucial. The evaluation procedure generally involves the usage of massively parallel computing architectures.

Computational models of CCSN have a long history starting with [39, 109]. Numerical investigations in one-, two- and three-dimensions have shown that (1) neutrino transport, (2) fluid instabilities, (3) rotation and (4) magnetic fields, together with an adequate treatment of (5) the sub- and super-nuclear density stellar matter equation of state, (6) neutrino interactions and (7) gravity are important [113]. A viable model of CCSN should incorporate these ingredients, at least to some extent. Ingredients (2)-(4) require by definition a multi-dimensional treatment (if not included by phenomenological means).

Our aim in this work is to construct a three-dimensional model of magneto-rotational CCSN including the most important physical ingredients according to earlier models in the literature. The fundament of our CCSN model was laid in [99] by M. Liebendörfer and we shall describe it in the following together with some extensions.

Under the prevailing conditions in CCSNe, stellar matter can be described by a charge neutral ideal magnetised fluid [81]. Furthermore, we base our model on a non-relativistic

framework. The governing equations are then given by the equations of ideal magnetohydrodynamics (MHD), where all dissipative processes are neglected, i.e. there is no viscosity and the conductivity is assumed to be infinite. The equations of ideal MHD read [83]

$$\frac{\partial \rho}{\partial t} + \nabla \cdot (\rho \mathbf{v}) = 0 \quad (1.6)$$

$$\frac{\partial \rho \mathbf{v}}{\partial t} + \nabla \cdot (\mathbf{v} \rho \mathbf{v} - \mathbf{b} \mathbf{b}) + \nabla P_{tot} = -\rho \nabla \phi + (\rho \dot{\mathbf{v}})_\nu \quad (1.7)$$

$$\frac{\partial E}{\partial t} + \nabla \cdot [(E + P_{tot}) \mathbf{v} - \mathbf{b} (\mathbf{v} \cdot \mathbf{b})] = -\rho \mathbf{v} \cdot \nabla \phi + (\rho \dot{e})_\nu \quad (1.8)$$

$$\frac{\partial \mathbf{b}}{\partial t} - \nabla \times (\mathbf{v} \times \mathbf{b}) = 0, \quad (1.9)$$

expressing the conservation of mass, momentum, total energy and magnetic flux. Here ρ is the mass density, \mathbf{v} the velocity and $E = \rho e + \frac{\rho}{2} v^2 + \frac{b^2}{2}$ the total energy density, being the sum of internal, kinetic and magnetic energy density. The magnetic field is given by $\mathbf{B} = \sqrt{4\pi} \mathbf{b}$ and $P_{tot} = p + \frac{b^2}{2}$ is the total pressure, being the sum of the fluid pressure and the magnetic pressure. The source terms on the right hand side come from gravity and the neutrino transport and will be discussed below.

The system of ideal MHD equations must be closed by an equation of state (EoS) describing the thermodynamic properties of stellar matter. The high temperatures ($T \gtrsim 8 \times 10^9$ K) prevailing in the iron core guarantee that matter is in nuclear statistical equilibrium (NSE), i.e. the nuclear strong interaction is in equilibrium, and the thermodynamic state and the nuclear composition depends solely on temperature, density and electron fraction. The electron fraction has also to be evolved and therefore we need to supplement an advection equation to the model

$$\frac{\partial \rho Y_e}{\partial t} + \nabla \cdot (\rho Y_e \mathbf{v}) = (\rho \dot{Y}_e), \quad (1.10)$$

where the source term depends on the inclusion of the neutrino transport. The EoS must be able to describe the stiffening of nuclear matter around nuclear matter density and this under yet experimentally unreachable conditions. The computation of EoSs from microphysical finite-temperature nuclear models is involved and a research field on its own. EoS evaluations are too expensive on-the-fly during simulations, therefore we rely on tabulated values. We have included the EoS of Lattimer and Swesty [86] and several EoSs from Hempel et al. [66].

Neutrinos dominate the energetics of the system as they represent $\sim 99\%$ of the liberated gravitational energy. Furthermore, neutrinos also influence the neutron to proton ratio of the in the explosion ejected matter which then crucially affects the production of the elements. Hence, the treatment of neutrinos is a corner stone of a CCSN model. Neutrinos propagate through the PNS and interact with the stellar fluid. Deep inside the PNS (at high densities), the neutrinos and the fluid are tightly coupled (almost in equilibrium). Their mean free path is much smaller than the size of the PNS and the neutrinos evolve in an advective-diffuse manner. On the other hand, at lower densities, the neutrino mean free path is much larger than the size of the core and neutrinos leave the star without any interaction. They are in a free streaming regime.

In an intermediate semi-transparent regime, the neutrinos are not transported by diffusion-advection, nor are they free streaming. In this regime, the neutrinos should ideally be described with the full kinetic theory given by the Boltzmann transport equation. Moreover,

the neutrino interactions and their associated cross sections are energy and flavour dependent. The Boltzmann transport equation describes the time evolution of the neutrino distribution $f(t, \mathbf{x}, E_\nu, \mathbf{p}/p)$, which, at each instant of time and each location gives the neutrino distribution in direction \mathbf{p}/p and energy E_ν . Hence the Boltzmann equation is a phase-space equation, which in three spatial dimensions results in a six-dimensional time dependent problem.

Due to the complexity of the problem, the full Boltzmann transport equation is yet only solved in spherical symmetry (where it is already a 3D problem!) [72, 97, 113]. In general, multi-dimensional CCSN models must therefore rely on approximations of the neutrino physics. For our model, we have opted for a spectral neutrino leakage scheme developed by A. Perego in spherical symmetry. A neutrino leakage scheme provides an efficient and effective estimate of the influence of neutrino cooling. So far we have included in our model only electron neutrinos and anti-neutrinos. The scheme splits the advective-diffuse regime into an advective and a diffuse part. The neutrinos are considered as a separate component of the fluid and advected with it. This is the so-called trapped neutrino component. Furthermore, mechanical work acting on the neutrino fluid must change the neutrino mean specific energy according to the first law of thermodynamics. One then introduces a neutrino fraction Y_ν and a neutrino specific mean energy Z_ν , which are described by the following equations [102]:

$$\frac{\partial \rho Y_\nu}{\partial t} + \nabla \cdot (\rho Y_\nu \mathbf{v}) = (\rho \dot{Y}_\nu) \quad (1.11)$$

$$\frac{\partial (\rho Z_\nu)^{3/4}}{\partial t} + \nabla \cdot ((\rho Z_\nu)^{3/4} \mathbf{v}) = (\rho \dot{Z}_\nu)^{3/4}. \quad (1.12)$$

The source term of (1.10), (1.11) and (1.12) represent the local source or sink of trapped neutrinos and their influence on the electron fraction. Diffusion is then handled in a phenomenological manner by estimates of the diffusion timescale. In the free streaming regime, any created neutrino simply escapes and $Y_\nu \sim Z_\nu \sim 0$. In the intermediate semi-transparent regime, an effective rate of transport is computed by interpolation between the two extreme limits of diffusion and free streaming. The leakage scheme also provides the momentum and energy source terms $(\rho \dot{\mathbf{v}}_\nu)$, $(\rho \dot{e}_\nu)$ in the momentum (1.7) and energy (1.8) equations, respectively.

Gravity plays a key role in CCSN. The gravitational potential ϕ is determined by the Poisson equation

$$\nabla^2 \phi = 4\pi G \rho, \quad (1.13)$$

where G is the gravitational constant. The compactness of the PNS is sufficient to make general relativistic effects important. Therefore we include in our model an effective description of general relativistic effects which mimic the deeper gravitational well of the relativistic case [106].

The bipolar jets arising in the magneto-rotational explosion mechanism carry and eject a significant amount of neutron rich matter. These jets represent a promising site for the rapid neutron capture process (r-process) [7, 110, 120]. Because the needed nuclear network with thousands of isotopes is yet beyond current computational capabilities in multidimensional simulations, we include a Lagrangian component in the form of tracer particles to our model. The trajectories (in densities, temperature and electron fraction) are then analysed in a post-processing step [174].

The above outlined model and its mathematical description in the form of non-linear partial differential equations (PDEs) can only be evaluated by numerical means. First one

has to set the domain over which one has to solve the equations. Figure 1.3 shows our computational setup. The innermost regions of the massive star, where the explosion is supposed to set in, is covered by a 3D domain of size 600^3 km. In the 3D domain, the MHD equations are evolved with the `FISH` code together with the spectral leakage scheme. Because in the magneto-rotational CCSN context rotation is inducing an approximate symmetry of the density field² around the rotational axis, we solve the Poisson equation in axisymmetry. This greatly reduces the computational load since no (global) elliptic problem has to be solved over the full 3D domain. The 3D domain is embedded in a larger spherical symmetric domain encompassing the iron core and parts of the silicon shell. The spherically symmetric domain is evolved by the time-implicit hydrodynamics code `AGILE` [101].

As in any model, one has to commit some trade-offs. The major weakness of our model relies in the disregard of neutrino heating effects. However, the to date most microphysically complete study of magneto-rotational CCSN in 2D axisymmetry [30], employing a multi-group flux limited diffusion (MGFLD), has shown that neutrino heating participates only to 15-25% to the total explosion energy. Therefore, we think that it is reasonable to neglect neutrino heating effects, but instead relax the geometrical constraint of axisymmetry. In future studies, we will consider to complete our model with a multi-dimensional neutrino transport approximation: the isotropic diffusion source approximation (IDSA) developed in the Basel supernova group [102].

In the following chapter 2, we will describe in detail the used numerical methods and their efficient parallel implementation.

²And of course also other fields (pressure, Y_e , ...).

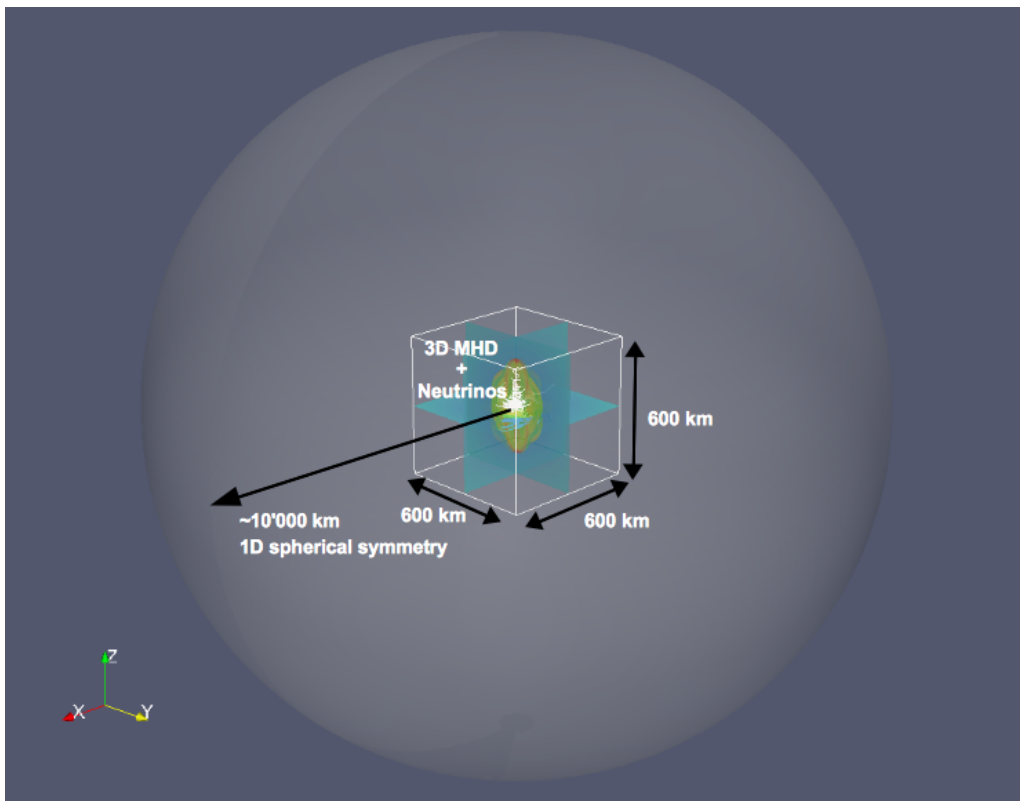


Figure 1.3: Schematic description of the computational domain: the 3D domain, encompassing the central 600^3 km of the massive star, is embedded in a larger spherically symmetric domain, encompassing the iron core and parts of the silicon shell.

Chapter 2

Numerical methods & implementations

2.1 Numerical solution of the ideal MHD equations: the FISH code

In this section we describe in detail the 3D ideal magnetohydrodynamics (MHD) code FISH. A condensed form of this section can also be found in Käppeli et al. 2011 [75].

FISH (Fast and Simple Ideal magneto-Hydrodynamics) is based on the publicly available serial version of a cosmological MHD code [126]. In this algorithm, the MHD equations are solved by rigorous application of the operator splitting technique. First, the MHD equations are split into a fluid and a magnetic part. The fluid part is then handled by a conservative finite volume scheme for an extended Euler system. The magnetic part, modelled by the magnetic induction equation, is handled by a magnetic flux conserving constrained transport method also thereby guaranteeing the divergence (of the magnetic field) constraint.

Compared to [126], our algorithm features the following modifications and innovations. The fluid evolution is modified to take into account local (to each cell) characteristic speed information instead of only global. This improves the solution accuracy significantly especially in cases where the characteristic speeds vary strongly in the computational domain (as is the case e.g. in core-collapse simulations). Further, the magnetic field evolution is modified for higher numerical stability, especially at high resolution.

2.1.1 The equations of ideal MHD

The equations of ideal MHD describe the movement of a compressible conducting fluid subject to magnetic fields. In ideal MHD all dissipative processes are neglected, meaning that the fluid possesses no viscosity and its conductivity is assumed to be infinite. The ideal MHD equations then read [83]

$$\frac{\partial \rho}{\partial t} + \nabla \cdot (\rho \mathbf{v}) = 0 \quad (2.1)$$

$$\frac{\partial \rho \mathbf{v}}{\partial t} + \nabla \cdot (\mathbf{v} \rho \mathbf{v} - \mathbf{b} \mathbf{b}) + \nabla P_{tot} = -\rho \nabla \phi \quad (2.2)$$

$$\frac{\partial E}{\partial t} + \nabla \cdot [(E + P_{tot}) \mathbf{v} - \mathbf{b} (\mathbf{v} \cdot \mathbf{b})] = -\rho \mathbf{v} \cdot \nabla \phi \quad (2.3)$$

$$\frac{\partial \mathbf{b}}{\partial t} - \nabla \times (\mathbf{v} \times \mathbf{b}) = 0, \quad (2.4)$$

expressing the conservation of mass, momentum, energy and magnetic flux, respectively. Here ρ is the mass density, \mathbf{v} the velocity and $E = \rho e + \frac{\rho}{2}v^2 + \frac{b^2}{2}$ the total energy density being the sum of internal, kinetic and magnetic energy densities. The magnetic field is given by $\mathbf{B} = \sqrt{4\pi}\mathbf{b}$ and $P_{tot} = p + \frac{b^2}{2}$ is the total pressure, being the sum of the gas pressure and the magnetic pressure. For the equation of state (EoS) we assume an ideal gas law

$$p = \rho e(\gamma - 1), \quad (2.5)$$

where γ is the ratio of specific heats. General EOSs can be included, which is especially important for the simulation of CCSN where the EoS has to describe stellar matter in the very broad range of conditions prevailing during this event. The right hand side of the momentum and energy conservation equations detail the effect of gravitational forces onto the conserved variables. We shall assume here the gravitational potential as given and fixed in time. The computation of the gravitational potential is discussed in section 2.3.

The MHD equations (2.1-2.4) conserve the divergence of the magnetic field so that an initial condition

$$\nabla \cdot \mathbf{b} = 0 \quad (2.6)$$

remains true, consistent with the physical fact that magnetic monopoles have never been observed.

2.1.2 Numerical solution of the MHD equations

The MHD equation form a set of non-linear hyperbolic equations, which can in general only be solved by numerical means. Before we start describing the individual solution operators, we first introduce our notation. We discretise time into discrete steps Δt^n and space into finite volumes or cells $V_{i,j,k}$ where n labels the different time levels and the triple (i, j, k) denotes a particular cell. The vector $\mathbf{u} = (\rho, \rho v_x, \rho v_y, \rho v_z, E)^T$ denotes the conserved fluid variables. The solution vector $\mathbf{u}_{i,j,k}^n$ contains the spatially averaged values of the conserved variables at time t in cell $V_{i,j,k}$

$$\mathbf{u}_{i,j,k} = \frac{1}{V_{i,j,k}} \int_{V_{i,j,k}} \mathbf{u}(\mathbf{x}, t) \, dx dy dz, \quad (2.7)$$

where the cell volume $V_{i,j,k} = \Delta x \Delta y \Delta z$ is given by the assumed constant cell dimensions $\Delta x = x_{i+1/2} - x_{i-1/2}$, $\Delta y = y_{j+1/2} - y_{j-1/2}$, $\Delta z = z_{k+1/2} - z_{k-1/2}$. Half-integer indices denote the intercell boundary. Further we define the cell face averaged magnetic field components at time t by

$$(b_x)_{i+1/2,j,k} = \frac{1}{S_{i+1/2,j,k}} \int_{S_{i+1/2,j,k}} b_x(\mathbf{x}, t) \, dy dz \quad (2.8)$$

$$(b_y)_{i,j+1/2,k} = \frac{1}{S_{i,j+1/2,k}} \int_{S_{i,j+1/2,k}} b_y(\mathbf{x}, t) \, dx dz \quad (2.9)$$

$$(b_z)_{i,j,k+1/2} = \frac{1}{S_{i,j,k+1/2}} \int_{S_{i,j,k+1/2}} b_z(\mathbf{x}, t) \, dx dy \quad (2.10)$$

where $S_{i+1/2,j,k} = \Delta y \Delta z$ denotes the cell face of cell $V_{i,j,k}$ located at $x_{i+1/2}$ and spanned by the zone increments Δy and Δz .

In an operator-split scheme the solution algorithm to the ideal MHD equations can be summarized as

$$\mathbf{u}^{n+2} = L_{\text{forward}} L_{\text{backward}} \mathbf{u}^n, \quad (2.11)$$

where

$$\begin{aligned} L_{\text{forward}} &= L_x(\Delta t) B_x^{yz}(\Delta t) L_y(\Delta t) B_y^{xz}(\Delta t) L_z(\Delta t) B_z^{xy}(\Delta t) \\ L_{\text{backward}} &= L_z(\Delta t) B_z^{xy}(\Delta t) L_y(\Delta t) B_y^{xz}(\Delta t) L_x(\Delta t) B_x^{yz}(\Delta t) \end{aligned} \quad (2.12)$$

are the forward and backward operator for one time step. The operators $L_{x,y,z}$ evolve the fluid and account for the source terms, while the B operators evolve the magnetic field. If the individual operators are second order accurate, then the application of the forward followed by the backward operator is second order accurate in time [149]. In the following subsections we shall detail the individual operators.

The numerical solution algorithm to the MHD equations is explicit. Hence we are restricted by the Courant, Friedrich and Lewy [41] (CFL) condition. Therefore we impose the following time step

$$\Delta t^n = k \cdot \min_{i,j,k} \left(\frac{\Delta x}{C_{i,j,k}^{n,x}}, \frac{\Delta y}{C_{i,j,k}^{n,y}}, \frac{\Delta z}{C_{i,j,k}^{n,z}} \right), \quad (2.13)$$

where

$$C_{i,j,k}^{n,d} = \max(v_{d,i,j,k}^n + c_{F,i,j,k}^n) \quad (2.14)$$

is the maximum speed at which information can travel in the whole computational domain in direction $d = x, y, z$, being the sum of the velocity component in d and the speed of the fast magnetosonic waves c_F . We typically set the CFL number k to 0.75.

2.1.3 Solving the fluid MHD equations

In this subsection we describe the evolution of the fluid variables \mathbf{u} in the x -direction. We neglect the source terms from gravity, which are treated in 2.1.5. During this process the magnetic field is held constant and interpolated to cell centers. Then mass, momentum and energy conservation in x -direction can be written as

$$\frac{\partial \mathbf{u}}{\partial t} + \frac{\partial \mathbf{F}}{\partial x} = 0, \quad (2.15)$$

where

$$\mathbf{F} = \begin{bmatrix} \rho v_x \\ \rho v_x^2 + P_{\text{tot}} - b_x^2 \\ \rho v_x v_y - b_x b_y \\ \rho v_x v_z - b_x b_z \\ (E + P_{\text{tot}}) v_x - b_x \mathbf{b} \cdot \mathbf{v} \end{bmatrix} \quad (2.16)$$

is the flux vector.

Integrating eq. (2.15) over a cell $V_{i,j,k}$ gives

$$\frac{\partial \mathbf{u}_{i,j,k}}{\partial t} + \frac{1}{\Delta x} (\mathbf{F}_{i+1/2,j,k} - \mathbf{F}_{i-1/2,j,k}) = 0, \quad (2.17)$$

where the definition of the cell averaged values (2.7) has been substituted and Gauss' theorem has been used. The numerical flux $\mathbf{F}_{i+1/2,j,k}$ represents an average flux of the conserved quantities through the surface $S_{i+1/2,j,k}$

$$\mathbf{F}_{i+1/2,j,k} = \frac{1}{S_{i+1/2,j,k}} \int_{S_{i+1/2,j,k}} \mathbf{F}(\mathbf{x}, t) dydz \quad (2.18)$$

at given time t . Eq. (2.17) is a semi-discrete conservative scheme for the conservation law (2.15). In the following we focus on obtaining the numerical fluxes in a stable and accurate manner. Time integration of the ordinary differential equation (2.17) will be addressed later in this subsection.

Many schemes for the stable and accurate computation of the numerical fluxes have been devised in the literature. Godunov type methods achieve this by solving either exact or approximate Riemann problems at cell interfaces [56, 85, 159]. Through solving the Riemann problem, these methods ensure an upwind discretisation of the conservation law and hence achieve causal consistency. Due to the difficulty of solving the Riemann problem in the ideal MHD case, the algorithm of [126] uses the relaxation scheme of [74]. For detailed information on these type of methods we refer to [74, 95] and the references therein.

The idea of the relaxation scheme is to replace a system like (2.15) by a larger system

$$\begin{aligned} \frac{\partial \mathbf{u}}{\partial t} + \frac{\partial \mathbf{w}}{\partial x} &= 0 \\ \frac{\partial \mathbf{w}}{\partial t} + D^2 \frac{\partial \mathbf{u}}{\partial x} &= \frac{1}{\epsilon} (\mathbf{F}(\mathbf{u}) - \mathbf{w}), \end{aligned} \quad (2.19)$$

called the relaxation system. Here, the relaxation rate ϵ is a small positive parameter and D^2 is a positive definite matrix. For small relaxation rates, system (2.19) rapidly relaxes to the local equilibrium defined by $\mathbf{w} = \mathbf{F}(\mathbf{u})$. A necessary condition for solutions of the relaxation system (2.19) to converge in the small ϵ limit to solutions of the original system (2.15) is that the characteristic speeds of the hyperbolic part of (2.19) are at least as large or larger than the characteristic speeds in system (2.15). This is the so-called subcharacteristic condition.

As [74] we choose $D = d \cdot I$ to be a diagonal matrix. In order to fulfill the subcharacteristic condition the diagonal element d or the so-called freezing speed is chosen to be

$$d = |v_x| + c_F, \quad (2.20)$$

where c_F is the speed of the fast magnetosonic waves, i.e. the fastest wave propagation speed supported by the equations of ideal MHD.

The key point in the relaxation system is that in the local equilibrium limit it has a very simple characteristic structure

$$\begin{aligned} \frac{\partial}{\partial t} (\mathbf{w} + D\mathbf{u}) + D \frac{\partial}{\partial x} (\mathbf{w} + D\mathbf{u}) &= 0 \\ \frac{\partial}{\partial t} (\mathbf{w} - D\mathbf{u}) - D \frac{\partial}{\partial x} (\mathbf{w} - D\mathbf{u}) &= 0, \end{aligned} \quad (2.21)$$

where $\mathbf{w} \pm D\mathbf{u}$ are then the characteristic variables. They travel with the ‘‘frozen’’ characteristic speeds $\pm D$ respectively.

System (2.21) can be easily recast into an equation for \mathbf{u} and \mathbf{w} . However, we are practically only interested in that for \mathbf{u}

$$\frac{\partial \mathbf{u}}{\partial t} + \frac{\partial \mathbf{F}^+}{\partial x} + \frac{\partial \mathbf{F}^-}{\partial x} = 0, \quad (2.22)$$

where $\mathbf{F}^+ = (\mathbf{w} + D\mathbf{u})/2$ denotes the right travelling waves and $\mathbf{F}^- = (\mathbf{w} - D\mathbf{u})/2$ the left travelling waves in the x -direction. In the following we shall drop the indices of the other directions. Since this defines an upwind direction for each wave component, a first

order upwind scheme results from choosing $\mathbf{F}_{i+1/2}^+ = \mathbf{F}_i^+$ and $\mathbf{F}_{i+1/2}^- = \mathbf{F}_{i+1}^-$. In this case, the total flux at the cell interfaces is readily evaluated to become

$$\mathbf{F}_{i+1/2} = \mathbf{F}_{i+1/2}^+ + \mathbf{F}_{i+1/2}^- = \frac{1}{2}(\mathbf{F}_i + \mathbf{F}_{i+1}) - \frac{1}{2}D(\mathbf{u}_{i+1} - \mathbf{u}_i), \quad (2.23)$$

where $\mathbf{F}_i = \mathbf{w}_i = \mathbf{F}(\mathbf{u}_i)$. For D we use the freezing speed

$$d = \max(d_i, d_{i+1}) \quad (2.24)$$

in order to satisfy the subcharacteristic condition. We note that the local choice eq. (2.24) for the freezing speed differs from the global choice in [126]. Further, eq. (2.24) for the freezing speed makes the numerical flux equivalent to the Rusanov flux and the local Lax-Friedrichs flux. As pointed out by [95], a wide variety of numerical flux assignments can be derived from the relaxation system by simply letting the matrix D having a more complicated form than diagonal.

So far, the numerical flux (2.23) is only first order accurate. First order methods permit the automatic capturing of flow discontinuities but are inaccurate in smooth flow regions due to the large amount of numerical dissipation inherent to them. As a matter of fact, the large numerical dissipation present in first order methods is not a deficit of these methods but it is the reason why they are stable at flow discontinuities in the first place. However, in many applications both smooth and discontinuous flow features are present and therefore the use of higher order methods is desirable. We opt for a second order accurate total variation diminishing (TVD) scheme due to the low computational cost and the robustness of these type of schemes.

Let us first consider the right traveling waves \mathbf{F}^+ . Given the i th cell, a first order accurate flux at the cell boundary $x_{i+1/2}$ is then given by $\mathbf{F}_{i+1/2}^+ = \mathbf{F}_i^+ = \mathbf{F}^+(\mathbf{u}_i)$. This corresponds to a piece-wise constant approximation of the flux function $\mathbf{F}^+(x, t)$ over the staggered cell $[x_i, x_{i+1}]$. For second order accuracy we seek a piece-wise linear approximation

$$\mathbf{F}^+(x, t) \approx \mathbf{F}_i^+ + \left. \frac{\partial \mathbf{F}^+}{\partial x} \right|_i (x - x_i), \quad (2.25)$$

where the derivative may be approximated from first order flux differences. Two choices exist: either left or right differences

$$\left. \frac{\partial \mathbf{F}^+}{\partial x} \right|_i = \begin{cases} \Delta \mathbf{F}_i^{+,L} = (\mathbf{F}_i^+ - \mathbf{F}_{i-1}^+) / \Delta x \\ \Delta \mathbf{F}_i^{+,R} = (\mathbf{F}_{i+1}^+ - \mathbf{F}_i^+) / \Delta x \end{cases}. \quad (2.26)$$

A flux limiter ϕ is used to choose between the left $\Delta \mathbf{F}_i^{+,L}$ and right $\Delta \mathbf{F}_i^{+,R}$ differences

$$\Delta \mathbf{F}_i^+ = \phi \left(\Delta \mathbf{F}_i^{+,L}, \Delta \mathbf{F}_i^{+,R} \right). \quad (2.27)$$

This limiter enforces a nonlinear stability constraint commonly known as Total Variation Diminishing (TVD) to ensure the stability of the scheme in the vicinity of discontinuities. The limiter reduces spurious oscillations associated with higher accuracy than first order to get a high resolution method. See for example [85, 90, 94, 159] and references therein. We have implemented the minmod limiter

$$\phi(a, b) = \text{minmod}(a, b) = \frac{1}{2} (\text{sign}(a) + \text{sign}(b)) \min(|a|, |b|), \quad (2.28)$$

which chooses the smallest absolute difference if both arguments have the same sign, and the van Leer limiter

$$\phi(a, b) = \frac{1}{2} (\text{sign}(a) + \text{sign}(b)) \frac{2ab}{a+b}. \quad (2.29)$$

Other choices are possible for the scheme to be TVD [74]. Note that when the left and right flux differences have different signs, i.e. at extrema and hence also at shocks, no correction is added in (2.25) and the scheme switches to first order accuracy. For core-collapse simulations we use the van Leer limiter in the subsonic flow regions and the minmod limiter in supersonic regions.

In a similar way we may construct a piece-wise linear approximation for the left going fluxes \mathbf{F}^- in the staggered cell $[x_i, x_{i+1}]$ starting at x_{i+1}

$$\mathbf{F}^-(x, t) \approx \mathbf{F}_{i+1}^- + \left. \frac{\partial \mathbf{F}^-}{\partial x} \right|_{i+1} (x - x_{i+1}) \quad (2.30)$$

with either the left or right differences

$$\left. \frac{\partial \mathbf{F}^-}{\partial x} \right|_{i+1} = \begin{cases} \Delta \mathbf{F}_{i+1}^{-,L} = (\mathbf{F}_{i+1}^- - \mathbf{F}_i^-) / \Delta x \\ \Delta \mathbf{F}_{i+1}^{-,R} = (\mathbf{F}_{i+2}^- - \mathbf{F}_{i+1}^-) / \Delta x \end{cases}. \quad (2.31)$$

Again the flux limiter ϕ is used to discriminate between the left or right differences

$$\Delta \mathbf{F}_{i+1}^- = \phi \left(\Delta \mathbf{F}_{i+1}^{-,L}, \Delta \mathbf{F}_{i+1}^{-,R} \right). \quad (2.32)$$

The total second order accurate numerical flux is then simply

$$\mathbf{F}_{i+1/2} = \mathbf{F}_i^+ + \mathbf{F}_{i+1}^- + \frac{\Delta x}{2} (\Delta \mathbf{F}_i^+ - \Delta \mathbf{F}_{i+1}^-). \quad (2.33)$$

For the time integration of eq. (2.17) we use a two step predictor-corrector method. As predictor we compute a half time step with the first order fluxes (2.23). We regard the freezing speed in the predictor step as a parameter varying between $d = 0$ and $d = \max(d_i, d_{i+1})$ to regulate the numerical dissipation. Hence we vary the predictor between a first order scheme and a second order centered difference scheme depending on the application.

In the corrector step we then use the calculated values from the predictor step $\mathbf{u}^{n+1/2}$ to compute the second order TVD fluxes eq. (2.33):

$$\mathbf{u}_i^{n+1} = \mathbf{u}_i^n - \frac{\Delta t}{\Delta x} \left(\mathbf{F}_{i+1/2}^{n+1/2} - \mathbf{F}_{i-1/2}^{n+1/2} \right). \quad (2.34)$$

Hence we obtain a second order update in time and space of the fluid variables. This ends the description of the L_x solution operator. The other spatial directions are treated in the same way.

2.1.4 Divergence preserving advection of the magnetic field

In this subsection we describe the divergence preserving advection of the magnetic field in x -direction B_x^{yz} . The operators for the update in y - and z -directions B_y^{xz} and B_z^{xy}

are handled analogously. During this operator split update, all quantities other than the magnetic field are held constant. The update is then prescribed by the induction equation

$$\frac{\partial \mathbf{b}}{\partial t} - \nabla \times (\mathbf{v} \times \mathbf{b}) = 0. \quad (2.35)$$

Straightforward discretisation of (2.35) can only guarantee that $\nabla \cdot \mathbf{b} = 0$ is of the order of the truncation error. However, at flow discontinuities, the discrete divergence may become large. As a consequence, large errors in the simulation can accumulate [22]. A variety of methods have been proposed to surmount this difficulty, see e.g. [46, 103, 136, 160, 161]. The algorithm of Pen et al. [126], and hence our code, uses the constrained transport method [46].

The key idea of the constrained transport method is to write the induction equation in integral form. Integrating eq. (2.35), for example, over the surface $S_{i+1/2,j,k}$ of cell $V_{i,j,k}$, substituting definition (2.8) and using Stoke's theorem yields

$$\frac{\partial}{\partial t} (b_x)_{i+1/2,j,k} = \int_{\partial S_{i+1/2,j,k}} \mathbf{v} \times \mathbf{b} \cdot d\mathbf{x}, \quad (2.36)$$

where $\partial S_{i+1/2,j,k}$ denotes the contour of $S_{i+1/2,j,k}$, i.e. the edges of the cell-face at $i+1/2$. The integral form then naturally suggests one to choose the normal projections of the magnetic field at faces of the cell $V_{i,j,k}$ and the normal projections of the electric field $\mathbf{E} = \mathbf{v} \times \mathbf{b}$ at the cell edges as primary variables. This positioning leads directly to the jump conditions of electric and magnetic fields [71] and therefore mimics Maxwell's equations at the discrete level (see figure 2.1). The discrete form of the $\nabla \cdot \mathbf{b} = 0$ constraint is then defined as

$$(\nabla \cdot \mathbf{b})_{i,j,k}^n = \frac{(b_x)_{i+1/2,j,k}^n - (b_x)_{i-1/2,j,k}^n}{\Delta x} + \frac{(b_y)_{i,j+1/2,k}^n - (b_y)_{i,j-1/2,k}^n}{\Delta y} + \frac{(b_z)_{i,j,k+1/2}^n - (b_z)_{i,j,k-1/2}^n}{\Delta z}. \quad (2.37)$$

A detailed inspection of the characteristic structure of the induction equation reveals the presence of two transport modes and one constraint mode. As pointed out by [126], this allows one to separate the evolution of the induction equation into advection and constraint steps. In x -direction, for example, this means that the y and z components of the magnetic field need to be updated as

$$\begin{aligned} \frac{\partial}{\partial t} (b_y)_{i,j+1/2,k} &= -\frac{1}{\Delta x} \left[(v_x b_y)_{i+1/2,j+1/2,k} - (v_x b_y)_{i-1/2,j+1/2,k} \right] \\ \frac{\partial}{\partial t} (b_z)_{i,j,k+1/2} &= +\frac{1}{\Delta x} \left[(v_x b_z)_{i+1/2,j,k+1/2} - (v_x b_z)_{i-1/2,j,k+1/2} \right]. \end{aligned} \quad (2.38)$$

However, the x component of the magnetic field has to be updated as

$$\begin{aligned} \frac{\partial}{\partial t} (b_x)_{i+1/2,j,k} &= +\frac{1}{\Delta y} \left[(v_x b_y)_{i+1/2,j+1/2,k} - (v_x b_y)_{i+1/2,j-1/2,k} \right] \\ &\quad -\frac{1}{\Delta z} \left[(v_x b_z)_{i+1/2,j,k+1/2} - (v_x b_z)_{i+1/2,j,k-1/2} \right]. \end{aligned} \quad (2.39)$$

The fluxes in eq. (2.38) need to be upwinded for stability, since they represent the two advection modes. To maintain $\nabla \cdot \mathbf{b} = 0$ within machine precision, the same fluxes used to update b_y and b_z in eq. (2.38) need to be used in eq. (2.39) for the b_x update. A simple calculation then clearly shows that $\partial/\partial t(\nabla \cdot \mathbf{b}) = 0$.

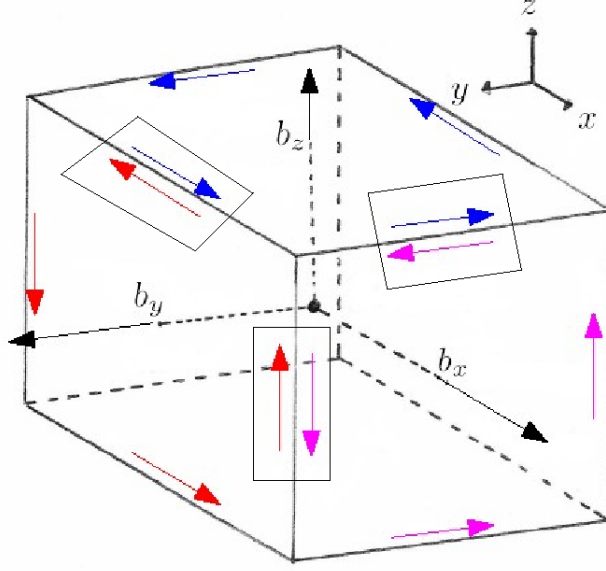


Figure 2.1: Schematic view of the positioning of the electromagnetic quantities in a computational cell. In the constrained transport scheme the total flux piercing the surface of a cell is always zero, achieved by balancing the electromotive force contributions taken around the cell edges. Arrows indicate the direction of the closed contour integral.

To update $(b_y)_{i,j+1/2,k}$ we then proceed as follows. A first order accurate upwinded flux is then given by

$$(v_x b_y)_{i+1/2,j+1/2,k} = \begin{cases} (v_x)_{i+1/2,j+1/2,k} (b_y)_{i,j+1/2,k} & , \quad (v_x)_{i+1/2,j+1/2,k} > 0 \\ (v_x)_{i+1/2,j+1/2,k} (b_y)_{i+1,j+1/2,k} & , \quad (v_x)_{i+1/2,j+1/2,k} \leq 0, \end{cases} \quad (2.40)$$

where the velocity has to be interpolated to the cell edge $(i + 1/2, j + 1/2, k)$. We use a simple bi-linear interpolation as

$$(v_x)_{i+1/2,j+1/2,k} = \frac{1}{4} \left[(v_x)_{i,j,k} + (v_x)_{i,j+1,k} + (v_x)_{i+1,j,k} + (v_x)_{i+1,j+1,k} \right], \quad (2.41)$$

which is second order accurate.

To obtain fully spatial second order accurate fluxes, we perform a piece-wise linear magnetic flux conserving reconstruction at each cell face $S_{i,j+1/2,k}$

$$b_y(x, t) \approx (b_y)_{i,j+1/2,k} + \left. \frac{\partial b_y}{\partial x} \right|_{i,j+1/2,k} (x - x_i), \quad (2.42)$$

where the derivative may be approximated by limited first order differences to obtain a non-oscillatory interpolation

$$\left. \frac{\partial b_y}{\partial x} \right|_{i,j+1/2,k} = \phi \left(\frac{(b_y)_{i+1,j+1/2,k} - (b_y)_{i,j+1/2,k}}{\Delta x}, \frac{(b_y)_{i,j+1/2,k} - (b_y)_{i-1,j+1/2,k}}{\Delta x} \right). \quad (2.43)$$

Here ϕ is a flux limiter and we have implemented the same limiters as for the fluid update, i.e. minmod and Van Leer. At each face interface, i.e. cell edge, we then get two boundary extrapolated values

$$\begin{aligned} (b_y)_{i+1/2,j+1/2,k}^L &= (b_y)_{i,j+1/2,k} + \frac{\partial b_y}{\partial x} \Big|_{i,j+1/2,k} \frac{\Delta x}{2} \\ (b_y)_{i+1/2,j+1/2,k}^R &= (b_y)_{i+1,j+1/2,k} - \frac{\partial b_y}{\partial x} \Big|_{i+1,j+1/2,k} \frac{\Delta x}{2}, \end{aligned} \quad (2.44)$$

where the slopes are limited. The spatial second order accurate flux is then simply

$$(v_x b_y)_{i+1/2,j+1/2,k} = \begin{cases} (v_x)_{i+1/2,j+1/2,k} (b_y)_{i+1/2,j+1/2,k}^L & , \quad (v_x)_{i+1/2,j+1/2,k} > 0 \\ (v_x)_{i+1/2,j+1/2,k} (b_y)_{i+1/2,j+1/2,k}^R & , \quad (v_x)_{i+1/2,j+1/2,k} \leq 0 \end{cases}. \quad (2.45)$$

Temporal second order accuracy is achieved as for the fluid update in a predictor-corrector manner. This ends the description of the $(b_y)_{i,j+1/2,k}$ component of the magnetic field. The update of the $(b_z)_{i,j,k+1/2}$ follows the same strategy.

We note that this magnetic field update is different from [126]. Empirically, we have found this update to be more robust especially at high resolutions. Similar schemes for the induction equation have been devised in e.g. [156], also in a constrained transport framework, and e.g. [160] and [52] where the magnetic field is defined at cell centers.

2.1.5 Gravitational source terms integration

Since the fluid evolution in FISH uses dimensional splitting, we also split the gravitational source term dimensionally as

$$\frac{\partial \mathbf{u}}{\partial t} + \frac{\partial \mathbf{F}}{\partial x} = \mathbf{S}_x, \quad (2.46)$$

where \mathbf{u} and \mathbf{F} are as defined above. The source term in x -direction is given by

$$\mathbf{S}_x = \begin{bmatrix} 0 \\ \rho \frac{\partial \phi}{\partial x} \\ 0 \\ 0 \\ \rho v_x \frac{\partial \phi}{\partial x} \end{bmatrix} \quad (2.47)$$

and in analogous manner for the y - and z -direction. In the following we shall regard the gravitational source term as given and constant in time. For the time integration of eq. (2.46) one then has two possibilities, either an operator split or unsplit method.

In the fully operator split version, the evolution of the conserved variables is divided into a homogeneous system ($\mathbf{S}_x = 0$) and the ordinary differential equation

$$\frac{d\mathbf{u}}{dt} = \mathbf{S}_x. \quad (2.48)$$

Solving the homogeneous part has been discussed in the previous section. In operator notation, we then solve equation (2.46) as

$$\mathbf{u}^{n+1} = G_x \left(\frac{\Delta t}{2} \right) L_x(\Delta t) G_x \left(\frac{\Delta t}{2} \right), \quad (2.49)$$

which is second order accurate in time.

Therefore the update of the momentum field is then explicitly

$$G_x(\Delta t) : (\rho \mathbf{v})_i^{n+1} = (\rho \mathbf{v})_i^n - \Delta t \cdot \rho_i^n \left(\frac{\partial \phi}{\partial x} \right)_i^n, \quad (2.50)$$

where we use centered differences for the gravitational potential

$$\left(\frac{\partial \phi}{\partial x} \right)_i^n = \frac{\phi_{i+1}^n - \phi_{i-1}^n}{2\Delta x}. \quad (2.51)$$

Note that the density field is left constant according to (2.46). The total energy is updated similarly.

As a second possibility, we implemented an unsplit version. There we directly account for gravity in the fluid predictor/corrector steps. The predictor step then is given by

$$\mathbf{u}_i^{n+1/2} = \mathbf{u}_i^n - \frac{\Delta t}{2\Delta x} \left(\mathbf{F}_{i+1/2}^n - \mathbf{F}_{i-1/2}^n \right) + \frac{\Delta t}{2} \mathbf{S}_i^n \quad (2.52)$$

where the $\mathbf{F}_{i+1/2}^n$ is the predictor numerical flux as described in previous section and

$$\mathbf{S}_i^n = \begin{bmatrix} 0 \\ \rho_i^n \\ 0 \\ 0 \\ (\rho v_x)_i^n \end{bmatrix} \frac{\phi_{i+1}^n - \phi_{i-1}^n}{2\Delta x}. \quad (2.53)$$

The corrector step is then

$$\mathbf{u}_i^{n+1} = \mathbf{u}_i^n - \frac{\Delta t}{\Delta x} \left(\mathbf{F}_{i+1/2}^{n+1/2} - \mathbf{F}_{i-1/2}^{n+1/2} \right) + \Delta t \mathbf{S}_i^{n+1/2}, \quad (2.54)$$

where the fluid fluxes are given in previous section and $\mathbf{S}_i^{n+1/2}$ is analogous to (2.53). However, the density and the momentum are then given by the predictor step $n + 1/2$. Both implementations of the source terms are second order accurate in space and time.

2.1.6 Generalisation to non-uniform meshes

Finite volume methods can be constructed for non-uniform meshes in a straightforward manner. The only quantities affected by the non-uniform mesh are the volumes of the computational cells, their bounding surfaces as well as the cell edge lengths.

In the current version of the code, we have implemented irregular Cartesian meshes. Then the mesh increments $\Delta x_i = x_{i+1/2} - x_{i-1/2}$, $\Delta y_j = y_{j+1/2} - y_{j-1/2}$, $\Delta z_k = z_{k+1/2} - z_{k-1/2}$ are no longer constant for the respective direction and equation (2.17) then changes to

$$\frac{\partial \mathbf{u}_{i,j,k}}{\partial t} + \frac{1}{\Delta x_i} \left(\mathbf{F}_{i+1/2,j,k} - \mathbf{F}_{i-1/2,j,k} \right) = 0. \quad (2.55)$$

For more general coordinates see for example [166].

The update formulas for irregular Cartesian meshes are then simply obtained by substituting Δx by Δx_i adequately in all the previous sections. Analogously Δy by Δy_j and Δz by Δz_k . Furthermore, the velocity interpolation (2.41) in the magnetic field advection needs also to conform with the non-equidistant spacing of the cell centers. Finally, the CFL condition eq. (2.13) needs to be adapted,

$$\Delta t^n = k \min \left(\frac{\Delta x_i}{C_{i,j,k}^{n,x}}, \frac{\Delta y_j}{C_{i,j,k}^{n,y}}, \frac{\Delta z_k}{C_{i,j,k}^{n,z}} \right) \text{ for all } i, j, k. \quad (2.56)$$

2.1.7 Efficient parallel implementation

The implementation of the above-described simple algorithms uses the directional operator splitting in a peculiar way: Instead of the traditional approach to hold the data locations fixed in memory while sweeping updates in x -, y -, and z -directions, we rearrange the data in the memory between the sweeps so that different directional sweeps always occur along the contiguous direction of the data in memory [126]. This has the advantage that the data load and store operations are very efficient for the large arrays that contain the three-dimensional data and that only a single one-dimensional subroutine is required per operator split physics ingredient to perform the corresponding data update in the sweep. The disadvantage is the additional compute load to rearrange the data (of order 10% of the total CPU-time) and the complications the rearranged data can cause if the code needs to import or export oriented data between the sweeps (e.g. for debugging).

The most convenient operation to rearrange the data in the desired way is a rotation with angle $2\pi/3$ about the axis threading the origin and point $(1, 1, 1)$. Each rotation aligns another original coordinate axis with the current x -direction, without changing any relative quantities between data points or the parity of the system. Three consequential rotations lead back to the original state.

The repeated evaluation of the physics equations in the 1D routines implementing their evolution prescription amounts to the dominant contribution to the total CPU-time. Because the sweeps are now always performed along contiguous memory, it is possible to pipeline the physics quantities in the cache so that the access of the large data arrays is reduced to a minimum. The first order predictor and second order corrector are evaluated according to the following scheme:

```
loop over cells i in x-direction
  u3 = u4
  u4 = u5
  u5 = u6
  u6 = u(i)
  if i<3 cycle
  uu1 = uu2
  uu2 = uu3
  uu3 = uu4
  uu4 = uu5
  uu5 = u5 + rate(u4,u5,u6)*0.5*dt !first order
  if i<7 cycle
  u(i-3) = u3 + rate(uu1,uu2,uu3,uu4,uu5)*dt !second order
end loop over cells
```

Here, $u(i)$ is the state vector with the conserved variables, which is only involved twice per time step dt , once for data retrieval and once for data storage. The evolution prescription of the physics equation is here abbreviated as `rate`. The whole operation has a stencil of 7 cells and will lead to 3 unassigned cells at each end of the array u . Hence, the buffer in Fig. 2.2 has to be large enough to host the unassigned cells.

The computational domain is then partitioned via a cubical domain decomposition. For the implementation of the parallel algorithm on distributed memory architectures we have used the Message Passing Interface (MPI) [59]. For the MHD application here, communication between individual parallel processing units or CPUs (henceforth just processes)

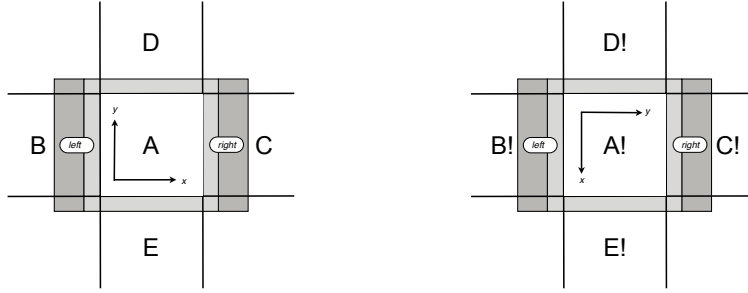


Figure 2.2: The interaction between sweeps and rotations is illustrated for a process A with its four neighbouring processes B-E. The distributed data stored and treated in process A carries a small permanent buffer area (light shading) around all of its interfaces. An additional volatile buffer (dark shading) is added in the current x -direction. The x -sweep is performed horizontally. For the y -sweep, the data and the permanent buffer are rotated clockwise by 90 degrees such that the y -sweep can also be performed in the horizontal direction.

is needed in two instances. The first is a collective communication, where all the processes participate, for the time step computation (CFL condition). The second are point-to-point communications between adjacent (in physical space) processes needed for the exchange of buffer or ghost cells for the stencil operations. The latter represents the dominant part of data communication (the time step computation needs only one float per process to be sent/received).

The domain decomposition is chosen to minimise the amount of data that has to be communicated. Suppose we want to distribute $N_x \times N_y \times N_z$ cells evenly across $N_p = p_x \times p_y \times p_z$ CPUs. Here $N_{x,y,z}$ and $p_{x,y,z}$ is the number of cells and the number of processors in the respective direction. We determine the decomposition triplet (p_x, p_y, p_z) by minimising the surface to volume ratio

$$\frac{\text{Surface}}{\text{Volume}} = \frac{2 \frac{N_x}{p_x} \frac{N_y}{p_y} + 2 \frac{N_x}{p_x} \frac{N_z}{p_z} + 2 \frac{N_y}{p_y} \frac{N_z}{p_z}}{\frac{N_x}{p_x} \frac{N_y}{p_y} \frac{N_z}{p_z}}. \quad (2.57)$$

Figure 2.2 shows the computational domain of a process A after the cuboidal domain decomposition. The data stored and updated in process A is surrounded by a small permanent buffer zone (light shading). In the current x -direction, there is an additional volatile buffer zone (dark shading). At the beginning of a time step, the overlapping data from process B is communicated to process A in order to update the buffer designated by 'left'. The overlapping data communicated from process C fills the buffer designated by 'right'. During the communication, the horizontal sweep in x -direction can already start to work on the interior zones that don't require the communicated buffer zones. Once all data has arrived, the x -sweep can be completed so that all zones in domain A and the permanent buffer are up to date. Hence communication is overlapped with computation. The details of the implementation are presented below.

In distributed memory parallelism, the bottleneck is generally the communication [59], i.e. the exchange of buffer zones between neighbouring processes. Therefore one goal is to overlap communication with computation. In the following we describe our implementation at the example of a sweep in x -direction. The other directions are handled analogously. We shall forget for the moment the rotation of the data.

The sweep in x -direction is performed by calling a routine `sweep($h_x, n_x, n_y, n_z, \mathbf{u}, \text{update}$)`, where $n_x = N_x/p_x$, $n_y = N_y/p_y$ and $n_z = N_z/p_z$ specify the dimension of the data array \mathbf{u} , belonging to a particular process, and where `update` points to a 1D routine that implements the physical equations treated by the sweep. The h_x is a handle, which holds the addresses of adjacent processes (left and right) for the communication of buffer data. In figure 2.2, these are communications $B \rightarrow A$ (left) and $C \rightarrow A$ (right). This handle is defined during the initialisation of the MPI parallel environment. Furthermore, since during the course of a parallel computation the location of parallel processes, i.e. the topology, remains fixed, the exchange of buffer cells can easily be implemented using a persistent communication request in the MPI at the beginning of a parallel computation. The communication is then started by simply calling `MPI_STARTALL(requests)` and checked for completion by `MPI_WAITALL`. Note that persistent communications are non-blocking, i.e. the call to initiate communication returns immediately and the program can continue. The communication should proceed in the background and one has then to check for its completion.

In figure 2.3 a particular process with data array u , containing the solution at time t^n (light blue), together with a pseudo-code sweep routine is shown. There are also two temporary data arrays `u_left` and `u_right` which are initially empty (white). The size of the `u_left` and `u_right` arrays in x -direction is $3\mathbf{x}\mathbf{b}$, where $\mathbf{x}\mathbf{b}$ is the number of unassigned cells at the boundary by the `update` routine (i.e. the stencil is $2\mathbf{x}\mathbf{b} + 1$). The `u_left` and `u_right` have the same size as \mathbf{u} in y - and z -direction. The first step in the `sweep` routine is then to copy data from the data array \mathbf{u} of size $2\mathbf{x}\mathbf{b}$ from the left and right end to the `u_left` and `u_right` arrays (see figure 2.3). This data is available locally and therefore no communication is needed.

The second step then consists of copying the data in \mathbf{u} that has to be exchanged with the left/right neighbouring processes into a sending buffer and of the initiation of the non-blocking point-to-point communication via the handle h_x (see figure 2.4). This is implemented using permanent communications in the MPI.

Once the communication is initiated, the non-blocking MPI routine immediately returns and we can proceed with the third step to update the data in array \mathbf{u} with the routine `update`. This step is illustrated in figure 2.5. When the update is finished, the data array \mathbf{u} contains the updated data at time t^{n+1} (green). At the left and right boundaries in x -direction of \mathbf{u} there are also $\mathbf{x}\mathbf{b}$ zones of unassigned or corrupted data because of the stencil of the update (red area in figure 2.5). Note that the left and right processes have also initiated their sends of halo data for our particular process. This data is continuously received during the update of \mathbf{u} and stored into the left/right receive buffer.

The fourth step then consists of testing if the non-blocking communication has completed during the update of the data array \mathbf{u} (see figure 2.6). Ideally, the communication completes during the third step. This efficiently overlaps communication with computation.

In the fifth step, the received data from the neighbouring processes, available in a receive buffer is copied into the `u_left` and `u_right` data arrays (see figure 2.7). Then the `update` routine is applied to `u_left` and `u_right` with exactly the same calling arguments except the size of the data arrays in x -direction. This results then in an updated central part of `u_left` and `u_right` of size $\mathbf{x}\mathbf{b}$ at time t^{n+1} (green) (see figure 2.8). At each side of `u_left` and `u_right`, $\mathbf{x}\mathbf{b}$ unassigned zones result (red) in the x -direction.

The sixth and last step then is to copy the updated data in `u_left` and `u_right` at time t^{n+1} onto its respective location in the data array \mathbf{u} . This is illustrated in figure 2.9. At the end of the `sweep` routine, all the data in \mathbf{u} is evolved to time t^{n+1} . With the just

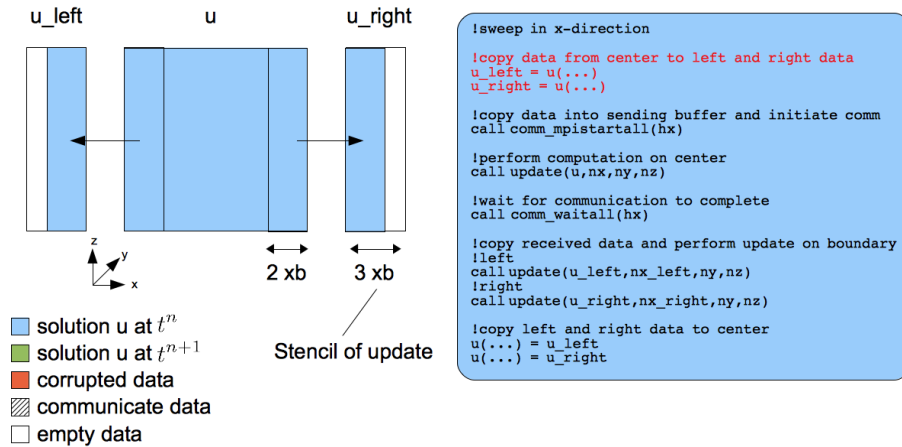


Figure 2.3: Illustration of the **sweep** routine: Copy data from center to left and right data.

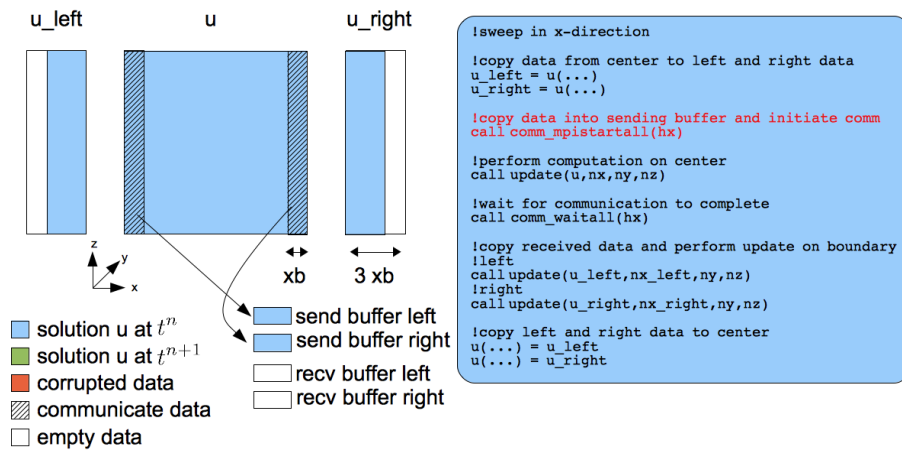


Figure 2.4: Illustration of the **sweep** routine: Copy of data into sending buffer and initiation of communication with neighbouring processes.

outlined procedure, the cumbersome dimensional index gymnastics in the **sweep** and the implementation of the physics in the routine **update** are very well disentangled. This ends the description of the **sweep** routine.

Now we come back to the question of how the rotation of the data interferes with the parallelisation. After having applied a cuboidal domain decomposition for distributed memory architectures, one realises that it is not meaningful to rotate the whole domain about the same rotation axis, because this would invoke excessive data communication among the processes. It is sufficient to rotate all cuboids individually about the axis defined in their local reference frame. These local rotations do not require any data communication. For the sweep in y -direction, all local data in Figure 2.2 are rotated clockwise by 90 degrees so that the y -direction becomes horizontal. This time it is the data of process E that need to be communicated to the buffer zones designated by 'left' and the data of process D that need to be communicated to the buffer zones designated by 'right'. Again, the sweep can start with the inner zones and update the border zones once the communications have completed. The important point is to realise that the y -sweep is now also applied in the horizontal direction so that the one-dimensional subroutines used

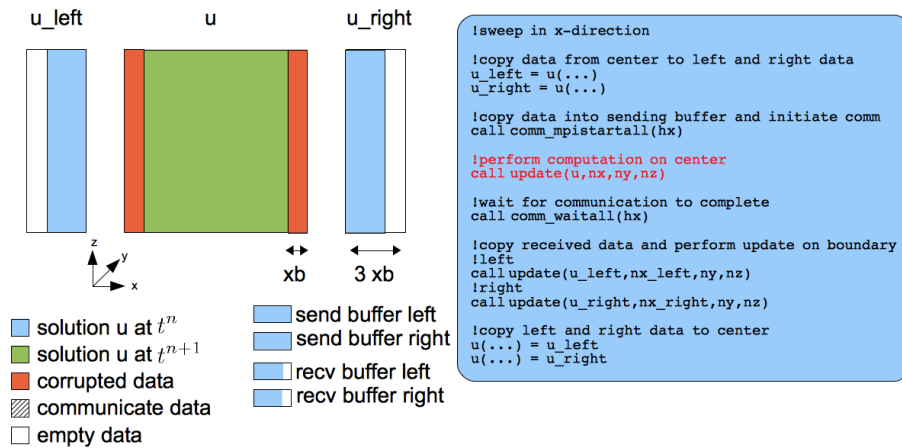


Figure 2.5: Illustration of the sweep routine: Perform update of center.

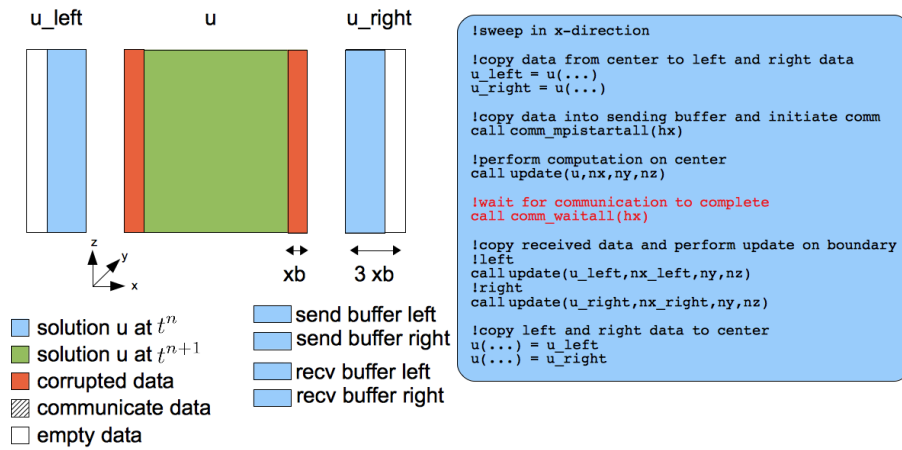


Figure 2.6: Illustration of the sweep routine: Wait for communication to complete.

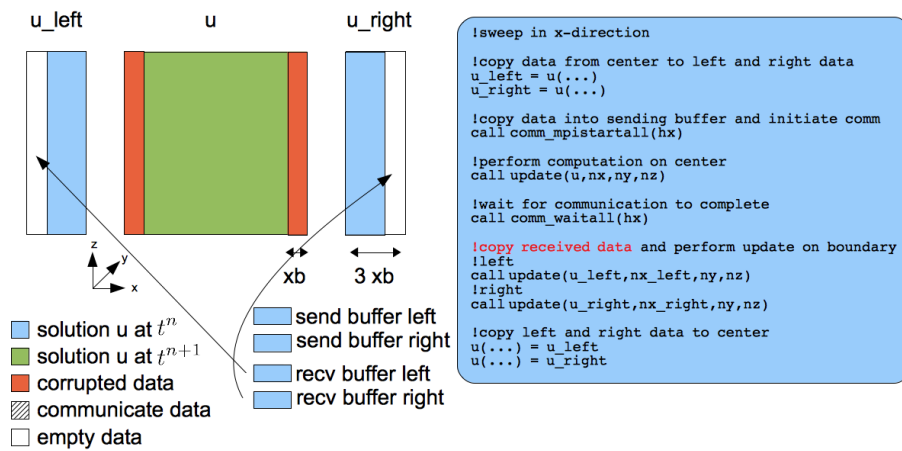


Figure 2.7: Illustration of the sweep routine: Copy received data.

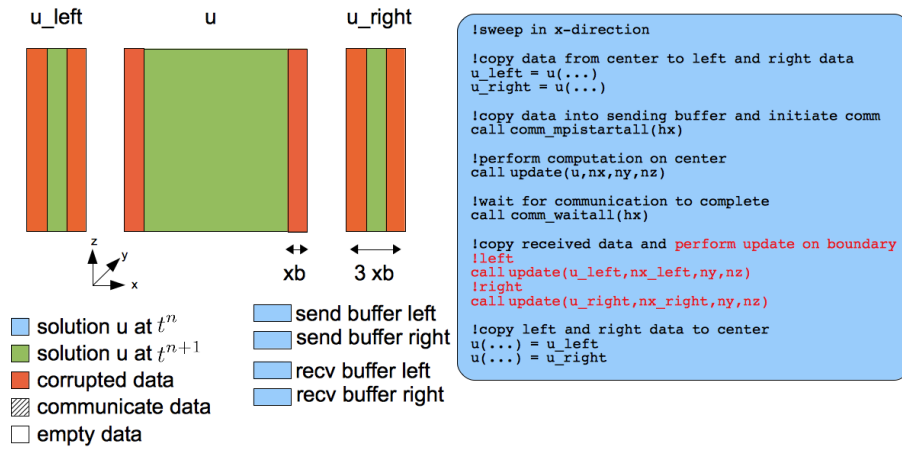


Figure 2.8: Illustration of the sweep routine: Apply update on left and right data.

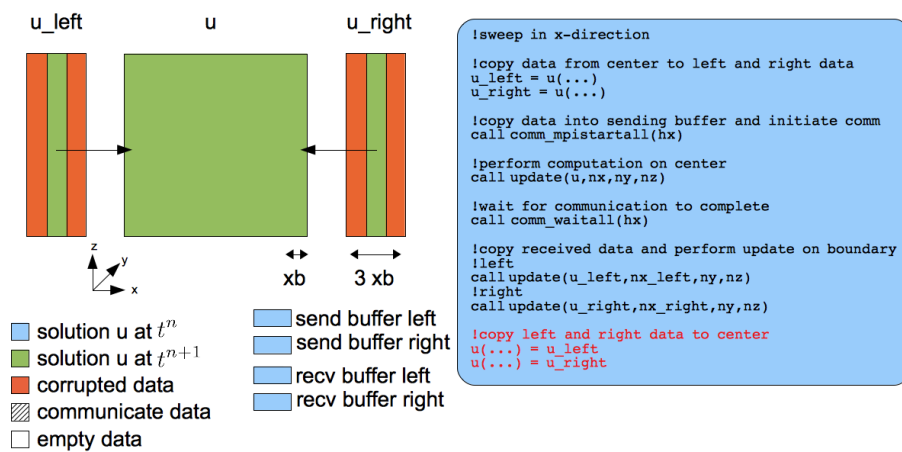


Figure 2.9: Illustration of the sweep routine: Copy updated left and right data onto center.

for the x -sweep can be used without any modifications. The y sweep is then initiated with a call `sweep($h_y, n_y, n_z, n_x, \mathbf{u}', \text{update}$)`, where \mathbf{u}' is the rotated state of \mathbf{u} . Here h_y is a handle, which holds the addresses of adjacent processes for the y sweep. Also `update` points to the same 1D routine that implements the physical equations as in the x sweep. In figure 2.2, this are communications $E \rightarrow A$ (left) and $D \rightarrow A$ (right). In the three-dimensional code, the procedure is repeated a third time for the sweeps in z -direction. Finally, all three sweeps are once more applied in reverse order to obtain second order accuracy. This ordering of the sweeps requires four rotations between the six directional sweeps.

Note that the horizontal sweep in x -direction is performed independently for all n_y rows of the data in process A . Hence it is straightforward to further parallelise the loop over the rows $i_y = 1 \dots n_l$ with OpenMP, where $n_l = n_y + 2n_{bp}$ is the dimension of A including the permanent buffer of width n_{bp} on either side. This one OpenMP parallel section suffices to parallelise over 90% of the workload of the code for shared memory nodes. Hence, the above-described approach naturally leads to a hybrid parallelisation, where MPI is used to distribute the memory by the cuboidal domain decomposition across different nodes or processors, while OpenMP is used to parallelise the loop over the rows along the current sweep direction on the cores that are available to each node or processor.

To give a measure of the code's performance in single-processor mode, we evaluated the number of cells updated per wall clock second. The code was compiled with the INTEL IFORT 10.1 compiler with -O2 optimisation level. The magnetic explosion test from subsection 2.1.8 was evolved with $N_x = N_y = N_z = 128$ on a single core of a dual-core AMD Opteron 8220 2.8 GHz. The code made 39 double time steps in 726.6 s wall clock time resulting in 225127 cell updates per second. We note that this measure is only qualitative and is highly dependent on e.g. the processor speed, compiler, compiler options and number of cells.

We evaluated the strong scaling of FISH on the new ROSA system (Cray XT-5, nodes with 2 quad-core AMD Opteron 2.4 GHz Shanghai processors, SeaStar 2.2 communications processor with 2 GBytes/s of injection bandwidth per node) at the Swiss National Supercomputer Center (CSCS). The dominant limitation to the scaling of FISH is the rather large stencil that emerges from the combination of the MHD and hydrodynamics solver with a first and second order step in a single sweep. FISH scales without problem if the problem size is increased with the increased number of processors. More interesting is the case of a fixed size problem. Figure 2.10 shows the strong scaling for a problem with 600^3 cells. As the number of processors is increased, the ratio of buffer zones to volume zones increases as well. In this case it is the evaluation of the physics equations on the buffer zones that limit the efficiency. However, Fig. 2.10 also shows that FISH scales very nicely to of order 10000 processes in the hybrid MPI/OpenMP mode where MPI is used between nodes and OpenMP within the node. This scaling can be achieved because the parallelisation with OpenMP does not increase the number of buffer zones.

There is still room for further optimisations, which we have begun to explore. A version of FISH with smaller stencils is under development. Furthermore, we have started to explore more OpenMP shared memory parallelisation, including the threading of the MPI library. In this approach, one OpenMP thread is dedicated to communicate the data with MPI while the other threads are used to perform the updates [132]. However, this optimisations are still in a preliminary phase.

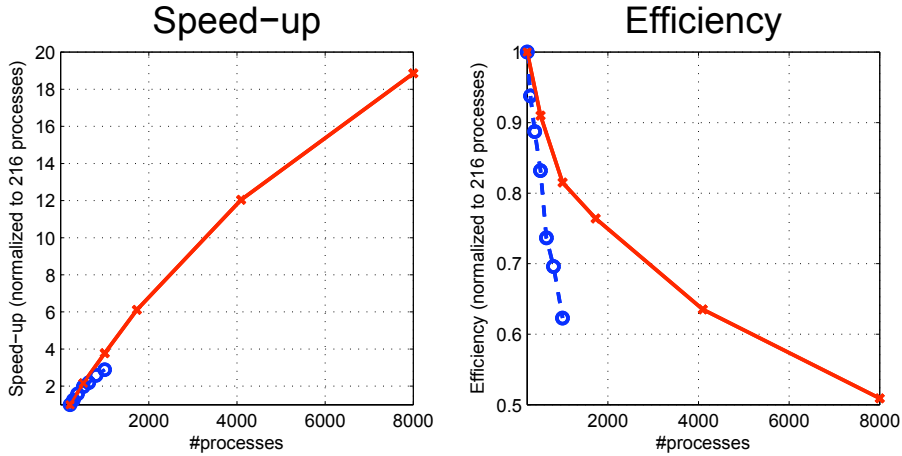


Figure 2.10: Strong scaling of the FISH code. The speedup, normalised to 216 processes, is shown on the left hand side. The efficiency is displayed on the right hand side. The dashed lines with data points taken at the circles refer to a parallelisation that uses only MPI. The solid lines with data points taken at the crosses refer to a hybrid parallelisation with MPI between nodes and OpenMP within nodes. The problem size was kept constant at 600^3 cells. The deviation from perfect scaling is rather due to the increase of work on buffer zones with respect to the work on volume zones than a bottleneck in the communication.

2.1.8 Numerical results

In this subsection we test our code by performing several multidimensional test simulations of astrophysical interest. Unless otherwise stated, we use periodic boundary conditions and the van Leer limiter for all test problems. The simulations are stopped before any interaction due to the periodic boundary can occur.

Linear wave convergence

Our first test problem involves the propagation of linear waves, namely the fast, Alfvén and slow modes, in 1D and 2D. We use a similar setup as [53] and [148].

The initial conditions are set as

$$\begin{aligned}\mathbf{u} &= \mathbf{u}_0 + A \mathbf{R}_p^{\text{FLUID}} \sin(2\pi\xi) \\ \mathbf{b} &= \mathbf{b}_0 + A \mathbf{R}_p^{\text{MAG}} \sin(2\pi\xi),\end{aligned}$$

where $\mathbf{u} = [\rho, \rho v_{\parallel}, \rho v_{\perp}, \rho v_z, E]^T$ and $\mathbf{b} = [b_{\parallel}, b_{\perp}, b_z]^T$. The subscript \parallel and \perp indicate the vector components parallel and perpendicular to the direction ξ , e.g. $\xi = x$, $\xi = y$ or $\xi = z$. The \mathbf{u}_0 and \mathbf{b}_0 are the constant background state of the conserved variables and the magnetic field on which a perturbation with amplitude A in direction ξ is set. The $\mathbf{R}_p^{\text{FLUID}}$ and $\mathbf{R}_p^{\text{MAG}}$ are the fluid and magnetic components of the right eigenvectors of the ideal MHD system. Expressions for these may be found in many references, see e.g. [134]. The constant background state \mathbf{u}_0 , \mathbf{b}_0 is set as in [53]. Then we have $\rho_0 = 1$, $p_0 = 1/\gamma = 3/5$, $v_{0,\parallel} = v_{0,\perp} = v_{0,z} = 0$ and $b_{0,\parallel} = 1$, $b_{0,\perp} = \sqrt{2}$, $b_{0,z} = 1/2$. This results in well separated propagation speeds for each mode: fast $c_f = 2$, Alfvén $c_A = 1$ and slow $c_s = 1/2$ modes. The perturbation is set to $A = 10^{-6}$. The numerical expressions for $\mathbf{R}_p^{\text{FLUID}}$ and $\mathbf{R}_p^{\text{MAG}}$ can be extracted from [53], appendix A.

After letting the waves evolve for one wavelength, we calculate the $L1$ norm of the difference between the initial conditions and the numerical solution over all cells

$$\begin{aligned}\delta\mathbf{u} &= \frac{1}{N} \sum_i |\mathbf{u}_i^n - \mathbf{u}_i^0| \\ \delta\mathbf{b} &= \frac{1}{N} \sum_i |\mathbf{b}_i^n - \mathbf{b}_i^0|,\end{aligned}$$

where the correct staggering of the magnetic variables is left out for readability. To get the total error, we take the $L2$ norm of $[\delta\mathbf{u}, \delta\mathbf{b}]^T$.

We then tested convergence for one dimensional linear waves in the domain $[0, 1]$, therefore ξ is simply $\xi = x$, by varying the resolution as $N_x = 32, 64, 128, 256, 512, 1024$ and $N_y = N_z = 1$. The computed total errors are shown in figure 2.11.

Next the linear waves are propagated in the $x - y$ plane at an angle $\alpha = 30^\circ$ with respect to the x -axis. The domain is set to $[0, 1/\cos\alpha] \times [0, 1/\sin\alpha]$ and is discretised with $N_x \times N_y$ cells where $N_x = N_y = 32, 64, 128, 256, 512, 1024$. The direction ξ is then given by $\xi = x \cos\alpha + y \sin\alpha$. The computed total errors are shown in figure 2.11.

We conclude that the scheme shows second order accuracy for linear wave propagation. Figure 2.11 may be compared with similar tests found in [148]. We note that when the magnetic field components are initialised at their respective staggered positions, the initial conditions are divergence free to machine precision for the chosen discretisations.

Circularly polarised Alfvén waves

Our second test problem involves the propagation of circularly polarised Alfvén waves in 1D and 2D. These waves are a smooth exact non-linear solution to the equations of ideal MHD [83] and represent therefore an ideal problem to test the convergence of numerical methods.

We have used the same initial conditions as [161]. The adiabatic index is set to $\gamma = 5/3$. Then we have $\rho = 1$, $v_{\parallel} = 0$, $p = 0.1$, $b_{\parallel} = 1$, $v_{\perp} = b_{\perp} = A \sin(2\pi\xi)$ and $v_z = b_z = A \cos(2\pi\xi)$. The subscript \parallel and \perp denote the components parallel and perpendicular to the wave propagation, respectively. We have set the wave amplitude to $A = 0.1$. With these parameters the Alfvén velocity is $b_{\parallel}/\rho = 1$ and the wave is evolved until it crossed once the domain and arrives back to its initial position.

First, we then tested convergence for one dimensional circularly polarised Alfvén waves in the domain $[0, 1]$, therefore ξ is simply $\xi = x$, by varying the resolution as $N_x = 32, 64, 128, 256, 512, 1024$ and $N_y = N_z = 1$. In figure 2.11 are shown the total errors computed as in the previous test problem after the wave profile crossed the domain once at $t = 1$.

Second, the circularly polarised Alfvén waves are propagated in the $x - y$ plane at an angle of $\alpha = 30^\circ$ with respect to the x -axis. The domain is set to $[0, 1/\cos\alpha] \times [0, 1/\sin\alpha]$ and is discretised with $N_x \times N_y$ cells where $N_x = N_y = 32, 64, 128, 256, 512, 1024$. The direction ξ is then given by $\xi = x \cos\alpha + y \sin\alpha$. The final time is $t = 1$. The computed total errors are shown in figure 2.11.

We conclude that the scheme shows second order accuracy as can be inferred from figure 2.11. The same remarks concerning the divergence free initialisation of the magnetic field apply as for the previous linear wave tests.

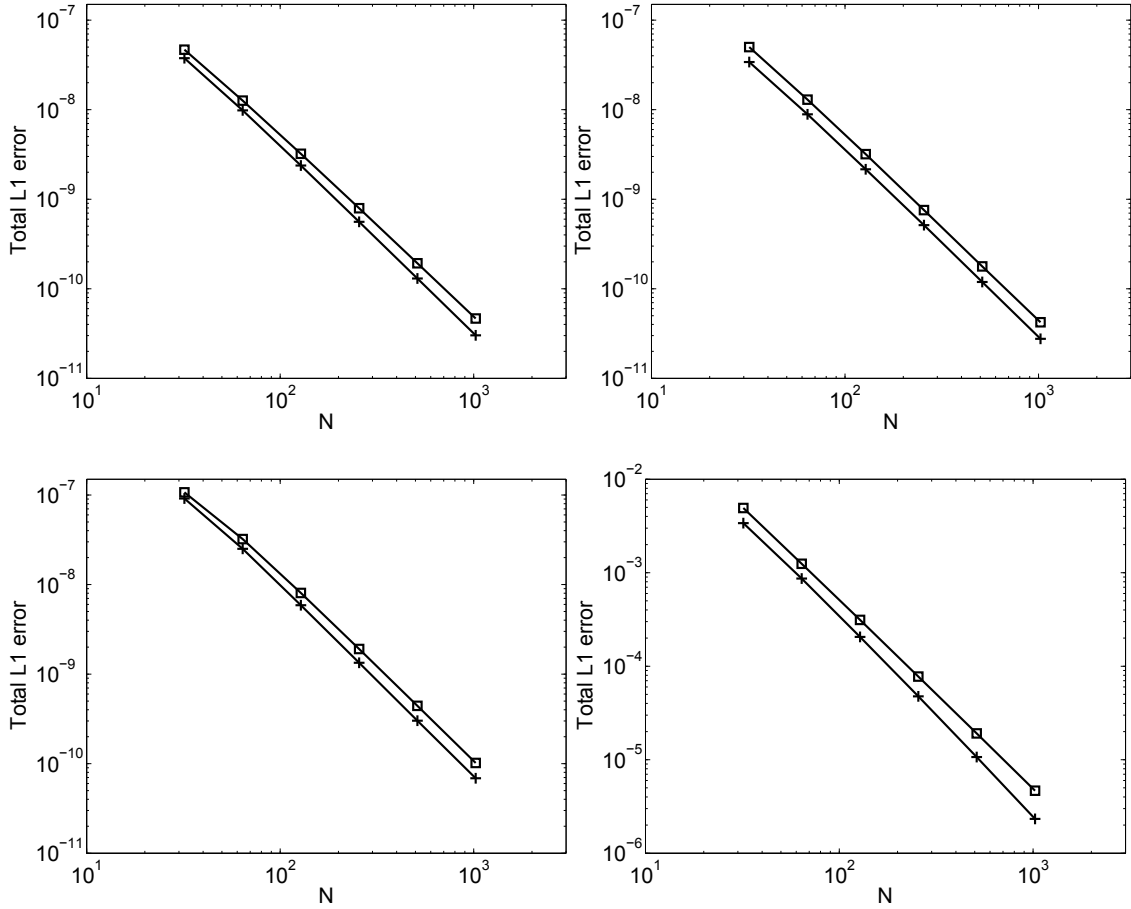


Figure 2.11: Convergence in the total error for fast (top left), Alfvén (top right), slow (bottom left) and circularly polarised Alfvén (bottom right) waves after evolving the waves once through the periodic domain in 1D (crosses) and 2D (squares).

Sedov-Taylor blast wave

The Sedov-Taylor blastwave test is a purely hydrodynamical test involving a strong spherically symmetric outward propagating shock wave. An analytical self-similar solution can be found for example in [84] and [173]. We use an adiabatic index of $\gamma = 5/3$. The problem is solved on a cubic domain $(x, y, z) \in [0, 1]^3$ with 256^3 computational cells and equidistant mesh spacing.

The density is set to unity and the velocity to zero throughout the whole domain. A huge amount of internal energy $e = 3 \times 10^3$ is placed uniformly in a small spherical region of radius 0.01 at the center of the domain. Outside the spherical region the energy is set to $e = 1 \times 10^{-3}$. The energy amount concentrated at the center then starts a strong shock wave which propagates spherically outward from the center of the domain. The simulation was stopped at time $t = 1.7419 \times 10^{-4}$ when the shock has propagated to a distance $r \approx 0.45$ from the center. In figure 2.12 a random subset of cells (points) are compared against the exact solution (solid line). All the values have been normalized to the exact postshock value. The postshock values of the numerical solution are lower but come close to the exact solution. Despite we have a dimensionally split code, the scattering of the points at the shock is not dramatic when compared to the Cartesian grid size of

$\Delta x = \Delta y = \Delta z \approx 0.004$. In figure 2.13 a shaded surface plot is shown for the density in the x, y plane with $z = 1/2$. As seen in the figure, the shock looks spherical and no serious symmetry breaking due to the dimensionally split character of the code can be seen.

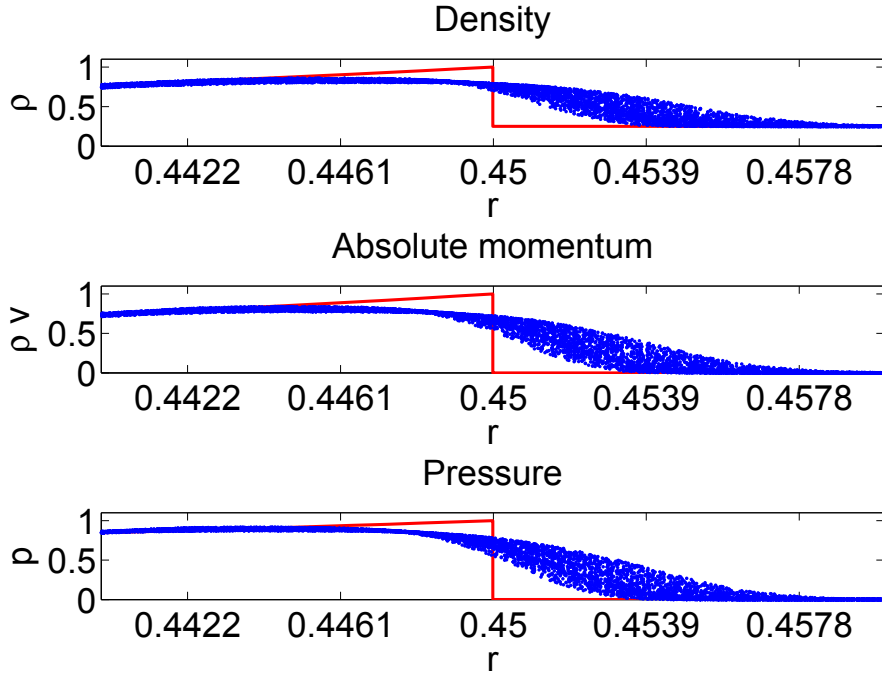


Figure 2.12: Radial distribution of the Sedov-Taylor blast wave test computed with 256^3 cells. The points represent a random subset of all the cells and the line is the exact solution. All values have been normalized to the exact postshock values. The ticks on the r axis have the size of the mesh spacing Δx and the shock is resolved within roughly $2\Delta x$. See the electronic edition of the Journal for a color version of this figure.

Spherical Riemann problem

This problem is a spherical setup of Sod's shocktube and was suggested in [159] as a test for multidimensional hydrodynamics codes. The solution is computed on a cubic domain $(x, y, z) \in [0, 1]^3$ with 256^3 computational cells and equidistant mesh spacing. Once again, an adiabatic index $\gamma = 5/3$ is used.

The domain is decomposed into a spherical region of radius $R = 0.25$ at the center of the domain and the remaining exterior region. The fluid variables are set to constant values in each region. At the boundary between both regions a spherical discontinuity results. In both regions, the velocity is set to zero. In the inner region we set the density $\rho = 0.125$ and the pressure $p = 0.1$. In the outer region, we set the density $\rho = 1$ and the pressure $p = 1$. The simulation is stopped at time $t = 0.09$.

In figure 2.14 the density distribution at the end of the simulation is displayed. The points are a random subset of cells and the solid line is a highly resolved numerical solution from a 1D spherically symmetric code based on the same algorithm as the 3D one. The shock, the contact discontinuity and the rarefaction wave are well captured by the 3D code. The scattering of the points is strongest at the inward propagating shock. In figure 2.15 a shaded surface plot of the density in the x, y plane with $z = 1/2$ is pictured. The spherical

character of the solution is well retained and the dimensional splitting does not degrade this symmetry.

Magnetic explosion

This test is based on the same idea as the Sedov-Taylor blastwave problem with the addition of a magnetic field. We used the same domain, number of cells and adiabatic index. The same initial conditions as in [54] are set. The density is set to $\rho = 1$ and the velocity to vanish everywhere in the domain. At the center of the domain we set the pressure $P = 100$ in a spherical region with radius $R = 0.125$. Outside of the sphere we set the pressure to $P = 1$. The magnetic field components are set as $b_x = b_y = 10/\sqrt{2}$ and $b_z = 0$. Inside the high pressure sphere the ratio between gas pressure and magnetic pressure is $\beta = 2P/b^2 \approx 2$ and outside it is $\beta = 2P/b^2 \approx 0.02$. This is a difficult test problem for codes evolving the total energy: The internal energy is obtained by the subtraction of kinetic and magnetic energy from the total energy. When the energy density is locally dominated by the magnetic field, negative internal energies can occur, which then break down the simulation.

The simulation was stopped at $t = 0.02$ and we used a CFL number of 0.75. The results

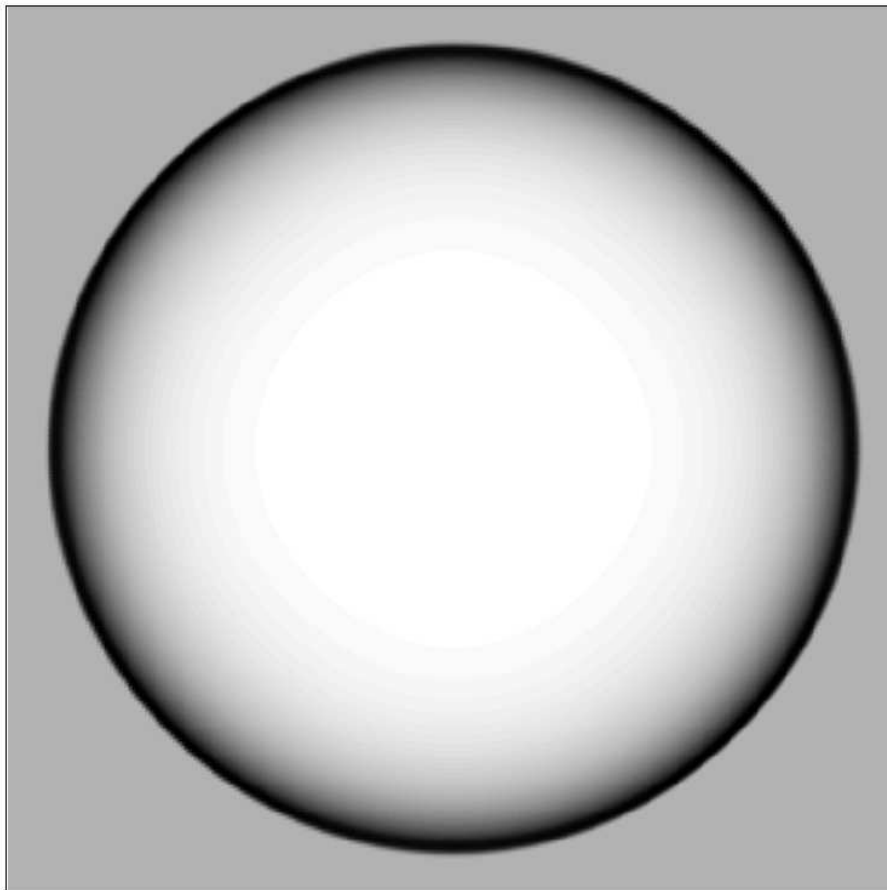


Figure 2.13: Shaded surface plot of the density for the Sedov-Taylor blast wave in the x, y plane with $z = 1/2$ illustrating the spherically symmetric character of the numerical solution. The solution was obtained with 256^3 cells.

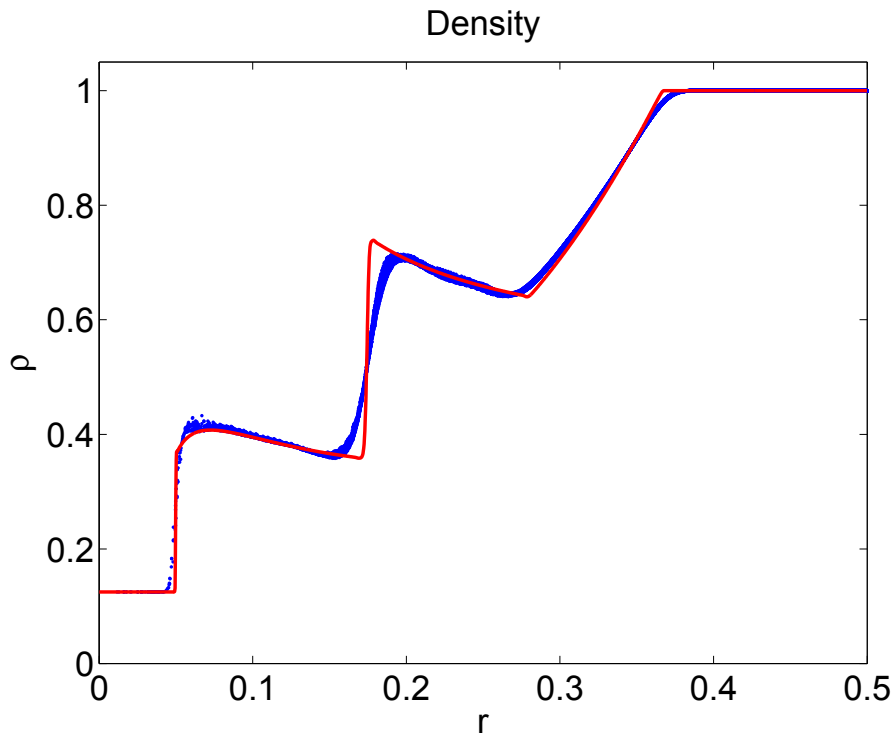


Figure 2.14: Radial density distribution of the spherical Riemann problem computed with 256^3 cells. The points represent a random subset of all the cells, and the line is the result of a highly resolved 1D simulation. See the electronic edition of the Journal for a color version of this figure.

are displayed in figure 2.16 for the density, pressure, kinetic energy and magnetic energy. As apparent from the figure, spherical symmetry is broken and one clearly distinguishes between the flow propagation parallel and orthogonal to the magnetic field. The outermost shell indicates a fast magnetosonic shock, which is only weakly compressive. The energy density is dominated by the magnetic field. On the inside there are two dense shells propagating parallel to the magnetic field. From the outside these dense shells are bound by a slow magnetosonic shock and a contact on the inside. Our results compare qualitatively well to the ones of [54].

The rotor problem

Our next test is the so-called rotor problem, presented in [13]. We use the first rotor problem in [161] as initial conditions. We solve this 2D problem in the Cartesian domain $[0, 1]^2$ with 256^2 computational cells. The problem consists of a dense rapidly rotating cylinder (the rotor) with $\rho = 10$, $v_x = -2(y - 1/2)/r_0$, $v_y = 2(x - 1/2)/r_0$ extending up to a radius $r_0 = 0.1$, where $r = [(x - 1/2)^2 + (y - 1/2)^2]^{1/2}$, installed in a lighter resting fluid. The lighter fluid is characterized by $\rho = 1$, $v_x = v_y = 0$ for $r > r_1 = 0.115$. In between the rotating and the light fluid $r_0 < r < r_1$ we set

$$\begin{aligned}\rho &= 1 + 9f(r) \\ v_x &= -2f(r)(y - 1/2)/r \\ v_y &= 2f(r)(x - 1/2)/r\end{aligned}$$

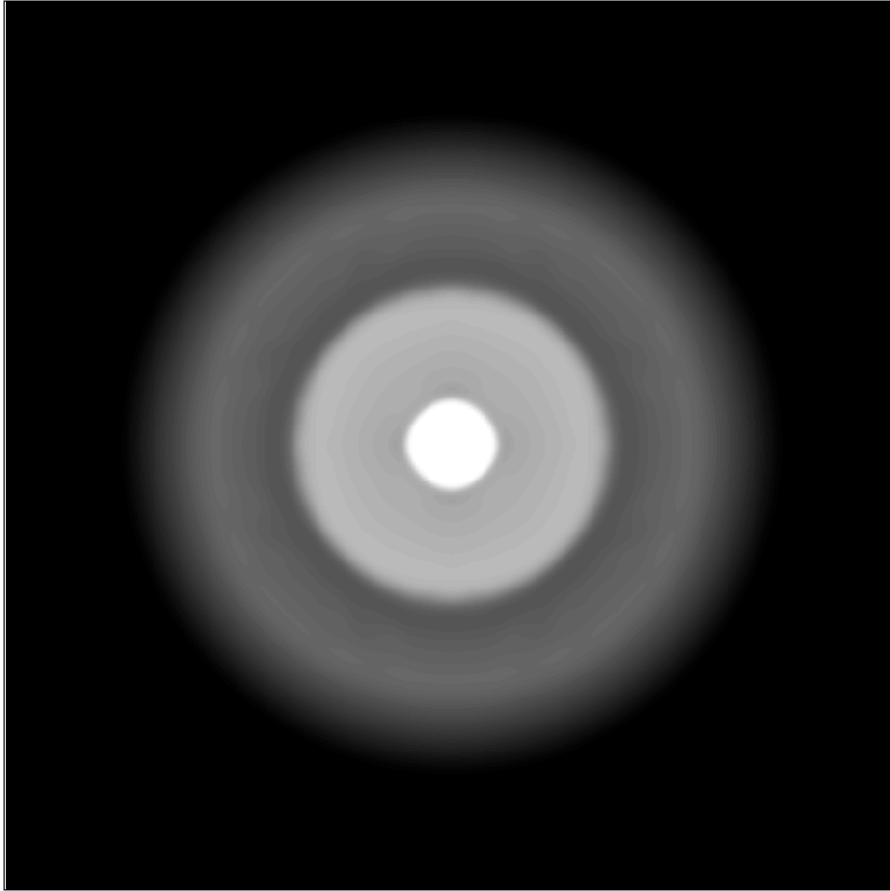


Figure 2.15: Shaded surface plot of the density for the spherical Riemann problem in the x, y plane with $z = 1/2$ illustrating the spherically symmetric character of the numerical solution. The density ranges from 1 (black) to 0.125 (white). The solution was computed with 256^3 cells.

where

$$f(r) = \frac{r_1 - r}{r_1 - r_0}.$$

This smooths out the discontinuities and reduces initial transients. The magnetic field is initially set to $b_x = 5/\sqrt{4\pi}$, $b_y = b_z = 0$ and the pressure is uniformly set to $p = 1$. The adiabatic index used for this test is $\gamma = 1.4$.

The simulation was run to time $t = 0.15$ and the results are displayed in figure 2.17. The dense rotating cylinder initially not in equilibrium has started to expand until the magnetic pressure due to field wrapping has stopped the expansion resulting in its oblate shape. The outer layers of the dense cylinder has lost part of its initial angular momentum in form of Alfvén waves radiating away. This braking of the magnetic rotor is a possible model for the angular momentum loss of collapsing gas clouds in star formation [116, 117].

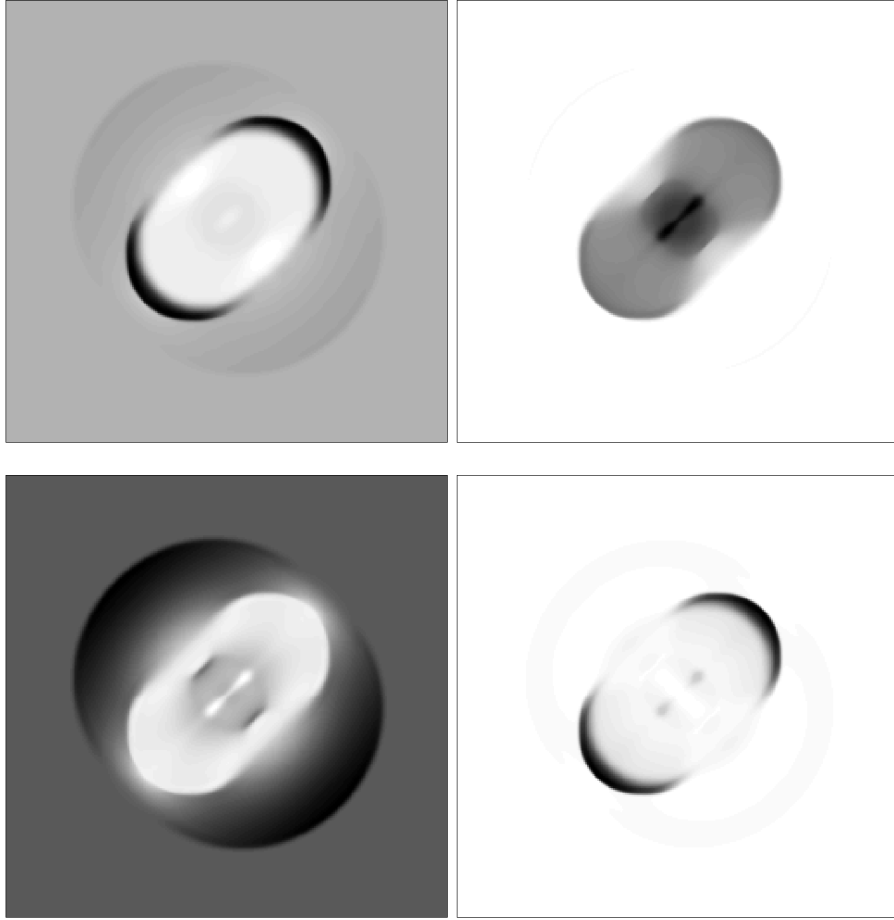


Figure 2.16: Shaded surface plot of the magnetic explosion at time $t = 0.03$ computed with 256^3 cells. Density (top left) ranges from 0.21 (white) to 2.75 (black). Gas pressure (top right) ranges from 1 (white) to 45.13 (black). Magnetic energy (bottom left) ranges from 23.90 (white) to 64.39 (black). Kinetic energy (bottom right) ranges from 0 (white) to 32.88 (black).

Two dimensional MHD Riemann problem

The next test we performed is a two dimensional Riemann problem. The initial conditions are similar to [42]:

$$(\rho, v_x, v_y, v_z, P) = \begin{cases} (1, -0.75, 0.5, 0., 1.), & x \leq L_x/2, y \leq L_y/2 \\ (3, -0.75, -0.5, 0., 1.), & x > L_x/2, y \leq L_y/2 \\ (2, 0.75, 0.5, 0., 1.), & x \leq L_x/2, y > L_y/2 \\ (1, 0.75, -0.5, 0., 1.), & x > L_x/2, y > L_y/2 \end{cases}$$

and the magnetic field is uniformly $\mathbf{b} = (2, 0, 1)/\sqrt{4\pi}$. We setup the problem on the domain $[0, 0.8]^2$ with 512^2 cells. The adiabatic index is set to $\gamma = 5/3$. For this test we used zeroth order extrapolation boundary conditions and evolved the problem to time $t = 0.8$. The density, pressure, kinetic energy and magnetic energy are displayed in figure 2.18. A similar test problem can also be found in [143]. Our results compare qualitatively well with the cited references.

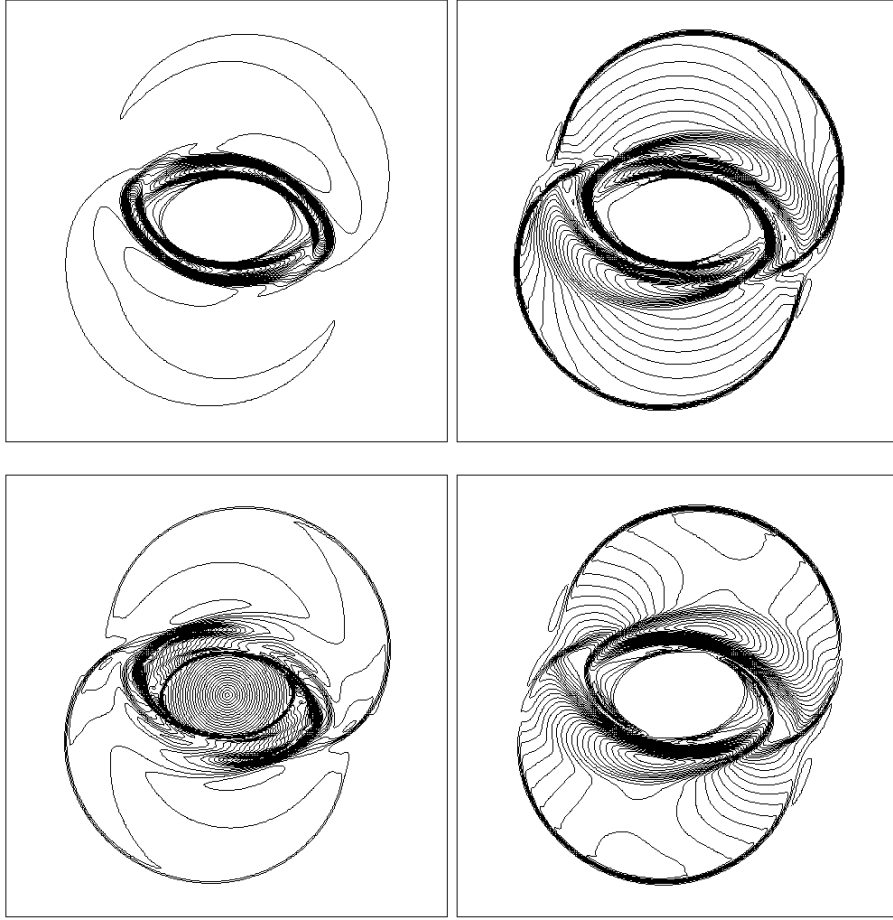


Figure 2.17: Contour plot of the rotor problem at time $t = 0.15$ computed with 256^2 cells. The density (top left), the gas pressure (top right), the Mach number (bottom left) and the magnetic pressure (bottom right).

Field loop advection

The next problem we consider, is the advection of a weak magnetic field loop. Similar initial conditions can be found in [53]. This problem tests the ability of the algorithm to maintain the solenoidal character of the magnetic field. The computational domain is set to $[0, 2] \times [0, 1]$ and is discretised by $N_x = 64, 128, 256, 512, 1024$ and $N_y = 32, 64, 128, 256, 512$ grid cells, respectively. Periodic boundary conditions are used.

The velocity field is set to

$$\begin{aligned} v_x &= v_0 \cos(\alpha) \\ v_y &= v_0 \sin(\alpha) \\ v_z &= 1, \end{aligned}$$

where $\cos(\alpha) = 1/\sqrt{5}$ and $\sin(\alpha) = 1/\sqrt{5}$ respectively. We set $v_0 = \sqrt{5}$ so that after a simulation time of $t = 2$ the field loop has been advected twice through the domain. The magnetic field is initialised with the magnetic vector potential where the only non-vanishing component is given by

$$A_z = \begin{cases} A_0(R - r) & , \text{ if } r \leq R \\ 0 & , \text{ if } r > R, \end{cases}$$

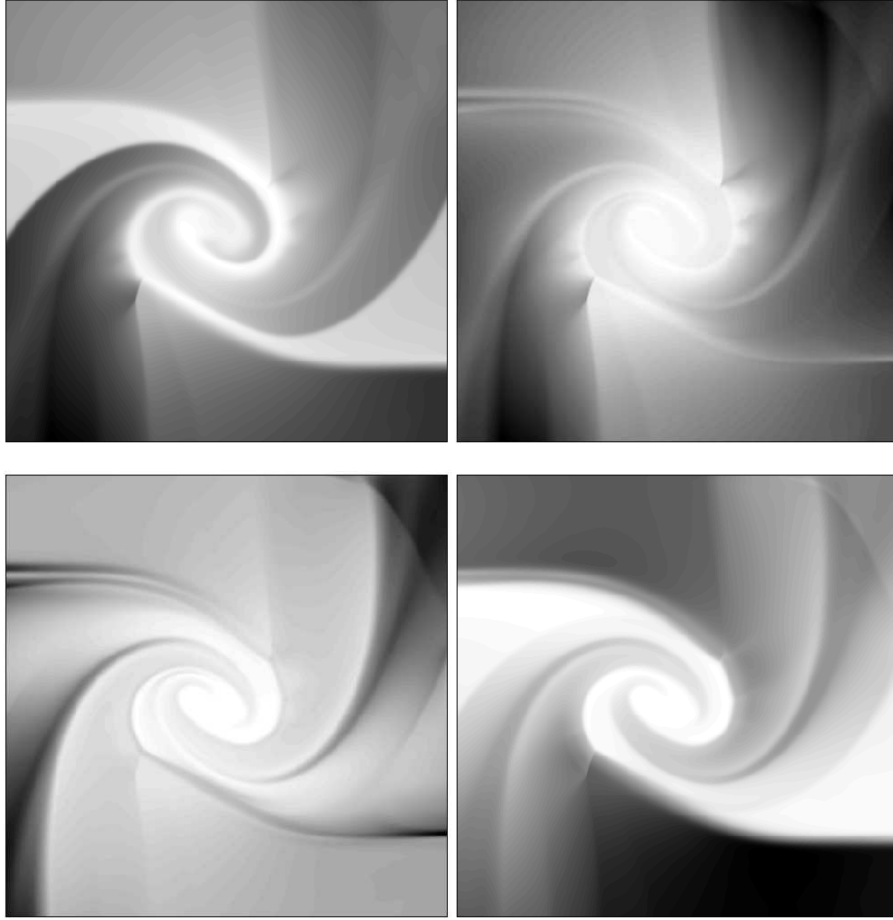


Figure 2.18: Shaded surface plot of the 2D MHD Riemann problem at time $t = 0.8$ computed with 512^2 cells. Density (top left) ranges from 0.2571 (white) to 2.4398 (black). Gas pressure (top right) ranges from 0.0787 (white) to 0.7091 (black). Magnetic energy (bottom left) ranges from 0.0029 (white) to 0.2501 (black). Kinetic energy (bottom right) ranges from 0 (white) to 0.6388 (black).

where $A_0 = 10^{-3}$, $R = 0.3$ and $r = \sqrt{x^2 + y^2}$.

The magnetic energy b^2 is displayed in figure 2.19 at the initial and final time for the 128×64 resolution. This figure may be directly compared to figure 6 in [53]. We observe that the circular shape is well preserved. However, we observe numerical magnetic field dissipation. Especially at the center and at the boundary of the field loop. The decay of the magnetic field energy is displayed in figure 2.20, where we plot the mean magnetic energy b^2 as a function of time normalised to its initial value for the tested resolutions. We note that while figure 2.19 gives a qualitative impression of where the magnetic energy is dissipated, figure 2.20 gives a quantitative measure of the dissipation as a function of resolution.

Similar to [88] we set $v_z \neq 0$. This choice then implies that b_z , initially zero, will grow in time if the magnetic field is not divergence free. During our simulations, b_z remained zero to machine precision and therefore the algorithm preserves numerically $\nabla \cdot \mathbf{b} = 0$ identically.

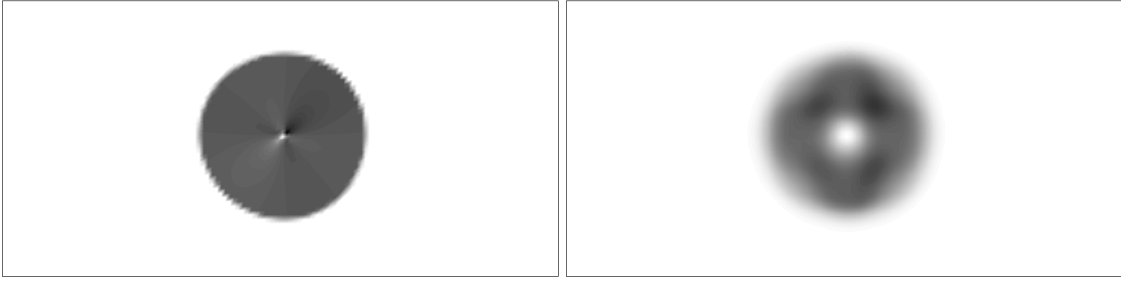


Figure 2.19: Shaded surface plot of the magnetic energy b^2 at times $t = 0$ (left) and $t = 2$ (right) with 128×64 resolution.

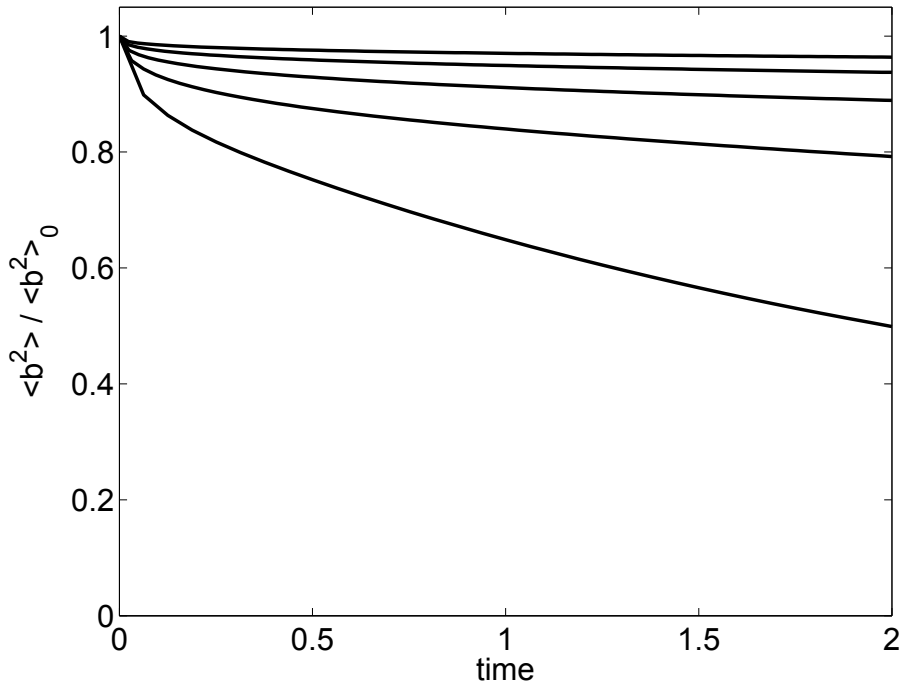


Figure 2.20: Plot of the mean magnetic energy as a function of time for the five tested resolutions: $N_x = 64, 128, 256, 512, 1024$ and $N_y = 32, 64, 128, 256, 512$ grid cells, respectively. The magnetic energy dissipation is monotonically decreasing with increasing resolution.

Isentropic vortex evolution

This test simulates the evolution of a stationary isentropic vortex in 2D (see e.g. [182]). This problem involves no flow discontinuities and an exact solution is available. The problem is solved on a square domain $[-5, 5]^2$ with $N = N_x = N_y = 64, 128, 256, 512, 1024$ computational cells and equidistant mesh spacing. We have used an adiabatic index of $\gamma = 1.4$.

The stationary background flow is initialised with $T_0 = 1$, $v_{x,0} = v_{y,0} = 0$, where $T = p/\rho$ is the temperature. The entropy is set to unity $S = p/\rho^\gamma = 1$. The following perturbations

are then added to get the T , v_x and v_y fields:

$$\begin{aligned}\delta T &= -\frac{\beta^2}{8\pi^2} \exp(1 - r^2) \\ \delta v_x &= -\frac{\beta}{2\pi} \exp\left(\frac{1 - r^2}{2}\right) y \\ \delta v_y &= \frac{\beta}{2\pi} \exp\left(\frac{1 - r^2}{2}\right) x,\end{aligned}$$

where $r^2 = x^2 + y^2$ and $\beta = 5$ is a measure of the vortex strength. The density is then computed by $\rho = (T_0 + \delta T)^{1/(\gamma-1)}$ and the pressure by $p = \rho^\gamma$.

The isentropic vortex is then evolved numerically up to $t = 10$ with a CFL number $k = 0.9$ and the Van Leer flux limiter. The flow is stationary and therefore the exact solution is simply the initial condition for all times. The total $L1$ errors are shown in figure 2.21. From the figure second order convergence is apparent.

This problem is also the basis for an accuracy test of the tracer particles evolution discussed in section 2.4.

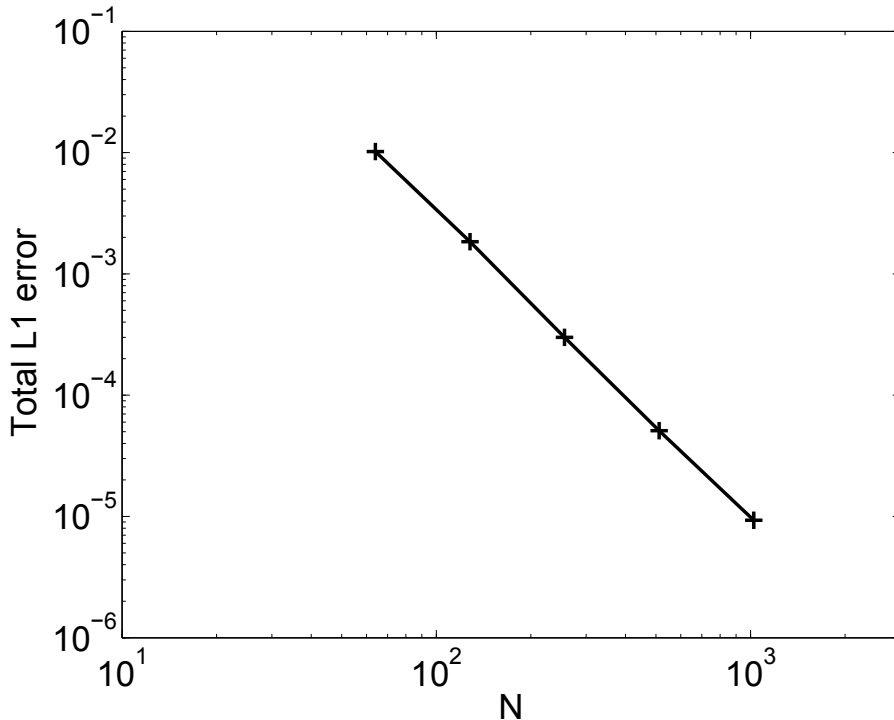


Figure 2.21: Convergence of the total error for the isentropic vortex test problem.

2.2 Well-balanced methods for hydrostatic equilibrium

In this section we present a novel well-balanced scheme for the Euler equations with gravitational source terms based on a discrete hydrostatic reconstruction. The extension of the method to general equations of state and to MHD will also be discussed. The section will end by several numerical examples demonstrating the accuracy of the scheme.

The Euler equations for a fluid in a gravitational field are given by

$$\frac{\partial \rho}{\partial t} + \nabla \cdot (\rho \mathbf{v}) = 0 \quad (2.58)$$

$$\frac{\partial \rho \mathbf{v}}{\partial t} + \nabla \cdot (\mathbf{v} \rho \mathbf{v}) + \nabla p = -\rho \nabla \phi \quad (2.59)$$

$$\frac{\partial E}{\partial t} + \nabla \cdot [(E + p) \mathbf{v}] = -\rho \mathbf{v} \cdot \nabla \phi, \quad (2.60)$$

expressing the conservation of mass, momentum and energy, respectively. We will also assume an ideal gas law for the equation of state (EoS)

$$p = \rho e(\gamma - 1). \quad (2.61)$$

The inclusion of more general EoSs will be discussed below.

The above equations allow a rich family of non-trivial steady states. Of particular interest in a multitude of applications is the hydrostatic state

$$\nabla p = -\rho \nabla \phi, \quad (2.62)$$

where the pressure gradient exactly balances the gravitational force. The interest in developing numerical schemes to accurately model this stationary or quasi-stationary solutions is twofold. On the one hand, one might be concerned with the simulation of small perturbations on a gravitationally stratified atmosphere. These perturbations may be small when compared to the density and pressure variations stemming from gravity and may therefore be difficult to resolve numerically. On the other hand, one might be interested in accurate long term simulations of stationary states. Long in the sense of many times a characteristic dynamic timescale on which the stationary state reacts to equilibrium perturbations.

In a CCSN context, this situation happens after bounce when the newly forming neutron star is approximately in hydrostatic equilibrium. In figure 2.22 we show a radial density and velocity profile at a typical time shortly after bounce. The stalled accretion shock is located at ~ 100 km. The density profile shows a steep gradient and the innermost parts are in near equilibrium ($v \approx 0$). The dynamical timescale of the innermost parts ($\gtrsim 10^{12}$ g/cm³) may be approximated by $(\bar{\rho}G)^{-1/2} \approx 1$ ms. This timescale is short when compared to the typical simulation time $\gtrsim 100$ ms. Therefore the numerical scheme should be able to hold the near hydrostatic equilibrium of the neutron and at the same time accurately model the perturbations on top of it. Since the neutron star is constantly accreting further matter (until an explosion sets in), the numerical scheme should be self-adapting to the slowly evolving equilibrium configuration. This poses some serious challenges for the numerical methods.

Conservation laws with source terms or, equivalently, balance laws arise abundantly in many research fields. These balance laws often admit steady state solutions in which the flux gradient is exactly balanced by the source term. Classical numerical solution methods generally fail to capture this subtle balance. Numerical schemes that maintain certain steady states either exactly or discretely are called well-balanced. Diverse well-balanced methods have been designed for specific problems, in particular for the shallow water equations, e.g. [8, 91, 121, 135, 179] and references therein.

Well-balanced methods for hydrostatic equilibrium have been developed in [21, 51, 93, 89]. Botta et al. [21] limpidly analyse the reason for the inaccuracies of standard high-resolution

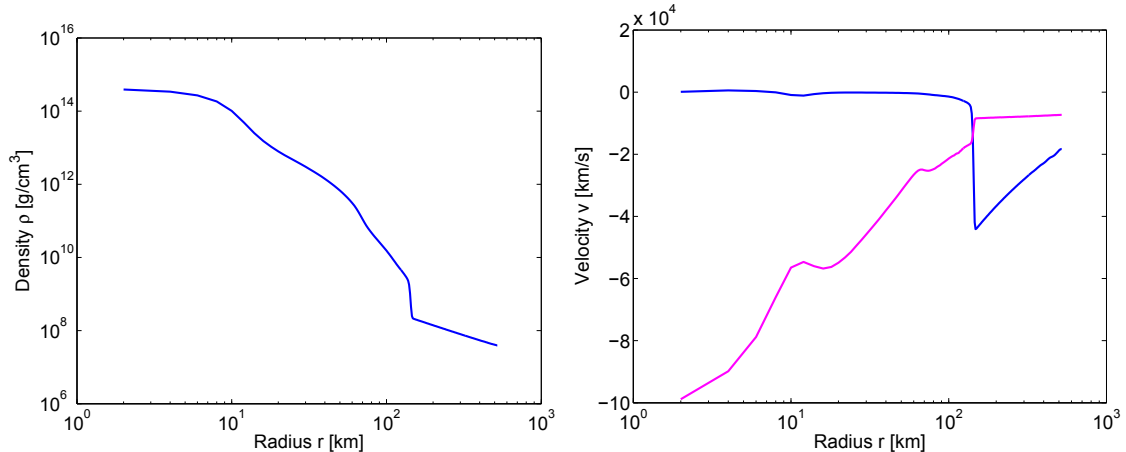


Figure 2.22: Density (left) and velocity (right) profiles in a CCSN simulation at a typical time postbounce. In the right panel, also the sound velocity is shown (solid magenta line). We observe that the innermost regions of the PNS are in near hydrostatic equilibrium $v \approx 0$. The numerical resolution of this near equilibrium state is difficult due to the large gradients in density (and also pressure, ...).

shock-capturing methods in preserving the hydrostatic state. The reason for these inaccuracies is that the equilibrium state is not a constant or a simple polynomial function. Hence, standard reconstruction techniques lead to non-zero truncation errors. This leads to spurious inaccuracies in computations of stationary states. Further, they propose an elegant numerical scheme combining local analytical hydrostatic reconstructions with a source term discretisation through a discrete Archimedes' buoyancy principle. The resulting scheme is second order accurate and well-balanced for homentropic hydrostatic states. In the following, we describe our well-balanced scheme for arbitrary entropy stratified hydrostatic equilibrium.

The organisation of this section is then as follows. In subsection 2.2.1 and 2.2.2, we will introduce a standard one-dimensional first order finite volume scheme for the Euler equations together with explicit expression for several numerical fluxes. In subsection 2.2.3, we present a discrete hydrostatic reconstruction scheme for the first order finite volume resulting in a well-balanced scheme. In subsection 2.2.4, we present an equilibrium preserving second order extension of the one-dimensional finite volume schemes. The multi-dimensional extension of the well-balanced schemes is then presented in subsection 2.2.5. In subsection 2.2.6, we present extensions of the hydrostatic reconstruction to general equations of states and also to MHD in the form of an approximately-balanced scheme. We end this section in 2.2.7 with several numerical experiments demonstrating the efficiency of the schemes.

2.2.1 First order one-dimensional schemes

For simplicity and without loss of generality we focus on the one-dimensional Euler equations in Cartesian coordinates:

$$\frac{\partial \mathbf{u}}{\partial t} + \frac{\partial \mathbf{F}}{\partial x} = \mathbf{S} \quad (2.63)$$

with

$$\mathbf{u} = \begin{bmatrix} \rho \\ \rho v_x \\ E \end{bmatrix}, \quad \mathbf{F} = \begin{bmatrix} \rho v_x \\ \rho v_x^2 + p \\ (E + p)v_x \end{bmatrix} \quad \text{and} \quad \mathbf{S} = \begin{bmatrix} 0 \\ \rho \\ \rho v_x \end{bmatrix} \frac{\partial \phi}{\partial x}, \quad (2.64)$$

where \mathbf{u} , \mathbf{F} and \mathbf{S} are the vectors of conserved variables, fluxes and source terms. Further, we will denote the primitive variables by $\mathbf{w} = [\rho, v_x, p]^T$.

Space is discretised into cells or finite volumes $I_i = [x_{i-1/2}, x_{i+1/2}]$ of regular size $\Delta x = x_{i+1/2} - x_{i-1/2}$ and time is discretised into time steps $\Delta t^n = t^{n+1} - t^n$, where n labels the different time levels. A standard first order finite volume scheme is obtained by integrating eq. (2.63) over a cell I_i and a time interval Δt^n (see e.g. [85, 92, 159])

$$\mathbf{u}_i^{n+1} = \mathbf{u}_i^n - \frac{\Delta t}{\Delta x} \left(\mathbf{F}_{i+1/2}^n - \mathbf{F}_{i-1/2}^n \right) + \Delta t \mathbf{S}_i^n, \quad (2.65)$$

where the time step has to fulfil a certain CFL condition. Here \mathbf{u}_i^n and \mathbf{u}_i^{n+1} are the cell average of the conserved variables at their respective time level. The $\mathbf{F}_{i\pm 1/2}^n$ are the numerical fluxes and \mathbf{S}_i^n the discretised source term to be given below.

2.2.2 Numerical fluxes: approximate solution of the Riemann problem

As is standard, the numerical flux is obtained by (approximate) solution of Riemann problems at the cell interfaces

$$\mathbf{F}_{i+1/2}^n = \mathcal{F}(\mathbf{u}_{i+1/2}^{n,L}, \mathbf{u}_{i+1/2}^{n,R}), \quad (2.66)$$

where the $\mathbf{u}_{i+1/2}^{n,L}$ and $\mathbf{u}_{i+1/2}^{n,R}$ are the cell interface extrapolated conserved variables. For a first order scheme these reduce to $\mathbf{u}_{i+1/2}^{n,L} = \mathbf{u}_i^n$ and $\mathbf{u}_{i+1/2}^{n,R} = \mathbf{u}_{i+1}^n$.

We have used several popular approximate Riemann solvers: local Lax-Friedrichs, HLL, HLLC and Roe. In the following we will give explicit expressions for the computation of the numerical fluxes according to these approximate Riemann solvers. We refer to the original research papers and textbooks (e.g. [85, 92, 159]) for their theoretical derivation.

The local Lax-Friedrichs approximate Riemann solver

The local Lax-Friedrichs solver assumes that the initial discontinuity at the cell interface decays into a right and a left discontinuity propagating with identical speeds. Therefore the solver does not resolve the contact discontinuity. This solver is also used in the MHD algorithm of FISH for the solution of the extended Euler equations 2.1.3. The numerical flux, consistent with the integral form of the homogeneous conservation law, is then

$$\mathbf{F}^{\text{LxF}} = \mathcal{F}(\mathbf{u}^L, \mathbf{u}^R) = \frac{1}{2} (\mathbf{F}^L + \mathbf{F}^R) - \frac{S^{\text{max}}}{2} (\mathbf{u}^R - \mathbf{u}^L), \quad (2.67)$$

where S^{max} is a numerical approximation for the largest physical signal-velocities in the exact solution to the Riemann problem, given by

$$S^{\text{max}} = \max(|v_x^L| + c^L, |v_x^R| + c^R). \quad (2.68)$$

The sound speed is given by $c = (\gamma p / \rho)^{1/2}$. The fluxes are simply $\mathbf{F}^L = \mathbf{F}(\mathbf{u}^L)$ and $\mathbf{F}^R = \mathbf{F}(\mathbf{u}^R)$.

The HLL approximate Riemann solver

Likewise, the HLL solver [62] assumes that the initial discontinuity at the cell interface decays into a right and a left discontinuity, however, propagating with different speeds. Like the Lax-Friedrichs solver, the HLL solver does not resolve the contact discontinuity. This solver can also be easily incorporated into FISH since the same amount of characteristic information (fastest physical signal-velocities) is needed than for the relaxation solver (which is equivalent to the local Lax-Friedrichs solver) 2.1.3. The HLL numerical flux is then

$$\mathbf{F}^{\text{HLL}} = \mathcal{F}(\mathbf{u}^L, \mathbf{u}^R) = \begin{cases} \mathbf{F}^L & \text{if } 0 \leq S^L \\ \frac{S^R \mathbf{F}^L - S^L \mathbf{F}^R + S^L S^R (\mathbf{u}^R - \mathbf{u}^L)}{S^R - S^L} & \text{if } S^L \leq 0 \leq S^R \\ \mathbf{F}^R & \text{if } S^R \leq 0, \end{cases} \quad (2.69)$$

where S_L, S_R are numerical approximations for the fastest physical signal-velocities in the exact solution to the Riemann problem, given by

$$\begin{aligned} S^L &= \min(v_x^L - c^L, v_x^R - c^R) \\ S^R &= \max(v_x^L + c^L, v_x^R + c^R). \end{aligned} \quad (2.70)$$

The HLLC approximate Riemann solver

The HLLC approximate Riemann solver [158] opens the Riemann fan with three waves, where the middle wave represents the contact discontinuity. This solver can also be generalised for the extended Euler system of the MHD algorithm in FISH (see [51] for details). The HLLC numerical flux is given by

$$\mathbf{F}^{\text{HLLC}} = \mathcal{F}(\mathbf{u}^L, \mathbf{u}^R) = \begin{cases} \mathbf{F}^L & \text{if } 0 \leq S^L \\ \mathbf{F}^{*,L} = \mathbf{F}^L + S^L (\mathbf{u}^{*,L} - \mathbf{u}^L) & \text{if } S^L \leq 0 \leq S^m \\ \mathbf{F}^{*,R} = \mathbf{F}^R + S^R (\mathbf{u}^{*,R} - \mathbf{u}^R) & \text{if } S^m \leq 0 \leq S^R \\ \mathbf{F}^R & \text{if } S^R \leq 0 \end{cases} \quad (2.71)$$

with

$$\mathbf{u}^{*,K} = \rho^K \frac{S^K - v_x^K}{S^K - S^m} \begin{bmatrix} 1 \\ S^m \\ \frac{E^K}{\rho^K} + (S^m - v_x^K) \left(S^m + \frac{p^K}{\rho^K (S^K - v_x^K)} \right) \end{bmatrix} \quad (2.72)$$

for $K = L, R$. Here S^L, S^R are numerical approximations for the fastest physical signal-velocities given in eq. (2.70). For the intermediate wave speed, we use an expression which depends merely on the assumed speeds S^L and S^R [16]

$$S^m = \frac{p^R - p^L + \rho^L v_x^L (S^L - v_x^L) - \rho^R v_x^R (S^R - v_x^R)}{\rho^L (S^L - v_x^L) - \rho^R (S^R - v_x^R)}. \quad (2.73)$$

The Roe approximate Riemann solver

Roe's approximate Riemann solver [133] is one of the most commonly used solvers. In this solver, the Riemann problem is approximately solved by writing the conservation law in quasi-linear form and evaluating the Jacobian matrix at a conveniently chosen state rendering the Riemann problem linear which can then be solved exactly. Like the HLLC, this solver resolves the full spectrum of modes present in the Euler equations and therefore resolves also the contact discontinuity.

The flux difference is then decomposed as

$$\mathbf{F}^R - \mathbf{F}^L = \sum_{i=1}^3 \tilde{\alpha}_i \tilde{\lambda}_i \tilde{\mathbf{R}}^{(i)}, \quad (2.74)$$

where the $\tilde{\mathbf{R}}^{(i)}$ are the right eigenvectors of the approximate Jacobian

$$\tilde{\mathbf{R}}^{(1)} = \frac{1}{2\tilde{c}} \begin{bmatrix} 1 \\ \tilde{v}_x - \tilde{c} \\ \tilde{H} - \tilde{c}\tilde{v}_x \end{bmatrix}, \quad \tilde{\mathbf{R}}^{(2)} = \frac{1}{\tilde{c}^2} \begin{bmatrix} 1 \\ \tilde{v}_x \\ \frac{1}{2}\tilde{v}_x^2 \end{bmatrix}, \quad \tilde{\mathbf{R}}^{(3)} = \frac{1}{2\tilde{c}} \begin{bmatrix} 1 \\ \tilde{v}_x + \tilde{c} \\ \tilde{H} + \tilde{c}\tilde{v}_x \end{bmatrix}, \quad (2.75)$$

where $\tilde{\lambda}_i$ are the propagation speeds

$$\tilde{\lambda}_1 = \tilde{v}_x - \tilde{c}, \quad \tilde{\lambda}_2 = \tilde{v}_x, \quad \tilde{\lambda}_3 = \tilde{v}_x + \tilde{c} \quad (2.76)$$

and where $\tilde{\alpha}_i$ are the wave strengths

$$\begin{aligned} \tilde{\alpha}_1 &= \frac{p^R - p^L}{\tilde{c}} - \tilde{\rho} (v_x^R - v_x^L) \\ \tilde{\alpha}_2 &= (p^R - p^L) - \tilde{c}^2 (\rho^R - \rho^L) \\ \tilde{\alpha}_3 &= \frac{p^R - p^L}{\tilde{c}} + \tilde{\rho} (v_x^R - v_x^L). \end{aligned} \quad (2.77)$$

The Roe averages are given by

$$\begin{aligned} \tilde{\rho} &= \sqrt{\rho^L \rho^R} \\ \tilde{v}_x &= \frac{\sqrt{\rho^L} v_x^L + \sqrt{\rho^R} v_x^R}{\sqrt{\rho^L} + \sqrt{\rho^R}} \\ \tilde{H} &= \frac{\sqrt{\rho^L} H^L + \sqrt{\rho^R} H^R}{\sqrt{\rho^L} + \sqrt{\rho^R}} \\ \tilde{c}^2 &= (\gamma - 1) \left(\tilde{H} - \frac{1}{2} \tilde{v}_x^2 \right), \end{aligned} \quad (2.78)$$

where H is the total enthalpy

$$H = \frac{E + p}{\rho}. \quad (2.79)$$

We use a standard Harten-Hyman entropy fix with speed estimates from the Roe averaged states to avoid expansion shocks [159]. The numerical flux is given by

$$\mathbf{F}^{\text{Roe}} = \mathcal{F}(\mathbf{u}^L, \mathbf{u}^R) = \frac{1}{2} (\mathbf{F}^L + \mathbf{F}^R) - \frac{1}{2} \sum_{i=1}^3 \tilde{\alpha}_i |\tilde{\lambda}_i| \tilde{\mathbf{R}}^{(i)}. \quad (2.80)$$

2.2.3 Well-balanced local hydrostatic reconstruction and source term discretisation

In one dimension, hydrostatic equilibrium is given when the pressure gradient exactly balances the gravitational force

$$\frac{\partial p}{\partial x} = -\rho \frac{\partial \phi}{\partial x}. \quad (2.81)$$

For any non-constant gravitational potential, hydrostatic equilibrium clearly dictates a non-trivial distribution of pressure and with it in density and internal energy. Therefore some type of hydrostatic reconstruction is needed when computing the point values at cell interface from the cell averaged conserved quantities. In case of equilibrium, this reconstruction should guarantee pressure continuity at the cell interface. When the equilibrium is perturbed, only the deviation from equilibrium should determine the pressure jump at the cell interface.

If the stationary state is known globally $\mathbf{u}_0(x)$, one can use $\mathbf{u}_0(x)$ to perform the reconstruction. This amounts to evolve numerically only the equilibrium perturbation $\mathbf{u} - \mathbf{u}_0$. However, if $\mathbf{u}_0(x)$ is not known in advance, a different approach has to be taken. As proposed in [21], another approach is to construct a local hydrostatic state $\mathbf{u}_{0,i}(x)$ inside each cell independently based on the local gravitational potential and thermodynamic conditions. This local hydrostatic state is then used for the reconstruction. A similar approach is taken in [51] in the context of wave propagation in stellar atmospheres.

We propose to perform the hydrostatic reconstruction based on a discrete form of (2.81) for the cell averaged pressure and density

$$\frac{p_{i+1}^n - p_i^n}{\Delta x} = -\frac{\rho_i^n + \rho_{i+1}^n}{2} \frac{\phi_{i+1} - \phi_i}{\Delta x}, \quad (2.82)$$

which is second order accurate at the cell interface. We then define the hydrostatic pressure differences

$$\begin{aligned} \Delta p_i^{n,+} &= -\frac{1}{2} \frac{\rho_i^n + \rho_{i+1}^n}{2} (\phi_{i+1} - \phi_i) \\ \Delta p_i^{n,-} &= -\frac{1}{2} \frac{\rho_{i-1}^n + \rho_i^n}{2} (\phi_i - \phi_{i-1}), \end{aligned} \quad (2.83)$$

which are then used to reconstruct the pressure at the cell interface

$$\begin{aligned} p_{i+1/2}^{n,L} &= p_i^n + \Delta p_i^{n,+} \\ p_{i+1/2}^{n,R} &= p_{i+1}^n - \Delta p_{i+1}^{n,-}. \end{aligned} \quad (2.84)$$

Note that pressure equilibrium at the cell interface, i.e. $p_{i+1/2}^{n,L} = p_{i+1/2}^{n,R}$, holds exactly if and only if eq. (2.82) is verified, by construction.

Now we have to compute from the interface pressures the corresponding density and internal energy density at the interface: $p_{i+1/2}^{n,L} = p(\rho_{i+1/2}^{n,L}, \rho e_{i+1/2}^{n,L})$ and $p_{i+1/2}^{n,R} = p(\rho_{i+1/2}^{n,R}, \rho e_{i+1/2}^{n,R})$. This inversion, however, is not yet uniquely determined and a further assumption on some thermodynamic variable is needed. We propose to use the polytropic relation

$$p = K(S)\rho^\gamma, \quad (2.85)$$

where γ is the ratio of specific heats and the coefficient $K(S)$ depends on the entropy S . We define the cell average of K_i^n simply by

$$K_i^n = p_i^n / (\rho_i^n)^\gamma. \quad (2.86)$$

The same choice was made in [21].

The interface density and internal energy density are then easily obtained:

$$\begin{aligned}\rho_{i+1/2}^{n,L} &= \left(\frac{p_{i+1/2}^{n,L}}{K_i^n} \right)^{1/\gamma} & \text{and} & \quad \rho e_{i+1/2}^{n,L} = \frac{p_{i+1/2}^{n,L}}{\gamma - 1} \\ \rho_{i+1/2}^{n,R} &= \left(\frac{p_{i+1/2}^{n,R}}{K_{i+1}^n} \right)^{1/\gamma} & \text{and} & \quad \rho e_{i+1/2}^{n,R} = \frac{p_{i+1/2}^{n,R}}{\gamma - 1}.\end{aligned}\tag{2.87}$$

The velocity, if the system is not in exact equilibrium $v_x = 0$, is left unchanged by the hydrostatic reconstruction $v_{x,i+1/2}^{n,L} = v_{x,i}^n$ and $v_{x,i+1/2}^{n,R} = v_{x,i+1}^n$. We then get the interface momentum density as

$$\begin{aligned}\rho v_{x,i+1/2}^{n,L} &= \rho_{i+1/2}^{n,L} v_{x,i} \\ \rho v_{x,i+1/2}^{n,R} &= \rho_{i+1/2}^{n,R} v_{x,i+1}.\end{aligned}\tag{2.88}$$

Similarly to the pressure differences, we may define hydrostatic density differences

$$\begin{aligned}\Delta \rho_i^{n,+} &= \rho_{i+1/2}^{n,L} - \rho_i^n \\ \Delta \rho_i^{n,-} &= \rho_i^n - \rho_{i-1/2}^{n,R},\end{aligned}\tag{2.89}$$

hydrostatic momentum differences

$$\begin{aligned}\Delta \rho v_{x,i}^{n,+} &= \rho v_{x,i+1/2}^{n,L} - \rho v_{x,i}^n \\ \Delta \rho v_{x,i}^{n,-} &= \rho v_{x,i}^n - \rho v_{x,i-1/2}^{n,R}\end{aligned}\tag{2.90}$$

and hydrostatic total energy density differences

$$\begin{aligned}\Delta E_i^{n,+} &= E_{i+1/2}^{n,L} - E_i^n \\ \Delta E_i^{n,-} &= E_i^n - E_{i-1/2}^{n,R}.\end{aligned}\tag{2.91}$$

We can then write the hydrostatic reconstruction in the following compact form for the conserved variables

$$\begin{aligned}\mathbf{u}_{i+1/2}^{n,L} &= \mathbf{u}_i^n + \Delta \mathbf{u}_i^{n,+} \\ \mathbf{u}_{i+1/2}^{n,R} &= \mathbf{u}_{i+1}^n - \Delta \mathbf{u}_{i+1}^{n,-}\end{aligned}\tag{2.92}$$

and for the primitive variables

$$\begin{aligned}\mathbf{w}_{i+1/2}^{n,L} &= \mathbf{w}_i^n + \Delta \mathbf{w}_i^{n,+} \\ \mathbf{w}_{i+1/2}^{n,R} &= \mathbf{w}_{i+1}^n - \Delta \mathbf{w}_{i+1}^{n,-}.\end{aligned}\tag{2.93}$$

The hydrostatic differences in conserved and primitive variables are given by

$$\Delta \mathbf{u}_i^{n,\pm} = \begin{bmatrix} \Delta \rho_i^{n,\pm} \\ \Delta \rho v_{x,i}^{n,\pm} \\ \Delta E_i^{n,\pm} \end{bmatrix} \quad \text{and} \quad \Delta \mathbf{w}_i^{n,\pm} = \begin{bmatrix} \Delta \rho_i^{n,\pm} \\ 0 \\ \Delta p_i^{n,\pm} \end{bmatrix}.\tag{2.94}$$

It remains to specify the discrete source term. Assume we are given discrete hydrostatic data verifying eq. (2.82). Plugging the reconstructed interface variables (2.92) into the

momentum component of the numerical flux divergence gives

$$\begin{aligned}
\frac{1}{\Delta x} \left[\mathcal{F}_{\rho v_x} \left(\mathbf{u}_{i+1/2}^{n,L}, \mathbf{u}_{i+1/2}^{n,R} \right) - \mathcal{F}_{\rho v_x} \left(\mathbf{u}_{i-1/2}^{n,L}, \mathbf{u}_{i-1/2}^{n,R} \right) \right] &= \frac{1}{\Delta x} \left[p_{i+1/2}^n - p_{i-1/2}^n \right] \\
&= \frac{1}{\Delta x} \left[(p_i^n + \Delta p_i^{n,+}) - (p_i^n - \Delta p_i^{n,-}) \right] \\
&= \frac{1}{\Delta x} \left[\Delta p_i^{n,+} + \Delta p_i^{n,-} \right]
\end{aligned} \tag{2.95}$$

for all the numerical fluxes in subsection 2.2.2. In the first equality, pressure equilibrium at the interface $p_{i\pm 1/2}^n = p_{i\pm 1/2}^{n,L} = p_{i\pm 1/2}^{n,R}$ was used. If the density and energy flux divergence components vanish depends on the entropy stratification $K(x)$ and the numerical flux used. For solvers resolving the contact discontinuity, namely the HLLC and the Roe solver, the density and energy flux divergence vanishes for any entropy stratification. For the local Lax-Friedrichs and HLL solver, this holds only for a constant entropy $K(x) = \text{const.}$, i.e. continuous density and internal energy density over the interface.

Eq. (2.95) therefore suggests the following form for the source term

$$\mathbf{S}_i^n = - \begin{bmatrix} 0 \\ \frac{1}{2} \left(\frac{\rho_{i-1}^n + \rho_i^n}{2} \frac{\phi_i - \phi_{i-1}}{\Delta x} + \frac{\rho_i^n + \rho_{i+1}^n}{2} \frac{\phi_{i+1} - \phi_i}{\Delta x} \right) \\ \rho v_{x,i}^n \frac{\phi_{i+1} - \phi_{i-1}}{2\Delta x} \end{bmatrix}, \tag{2.96}$$

where the energy source term uses a simple central discretisation.

We conclude that the first order scheme (2.65) and the hydrostatic reconstruction (2.94) together with the source term discretisation (2.96) maintains exactly, i.e. is well-balanced, any discrete stationary state in the form (2.82).

The definition $K(x) = K_i$ inside a cell is not the only possible choice. One could perform any high order reconstruction, e.g. piece-wise linear, to get a better representation of K inside the cell. However, this choice is not relevant for the scheme to maintain any discrete hydrostatic equilibrium (2.82). By construction, the pressure is continuous across the cell interface and any numerical flux resolving the contact discontinuity will yield a zero mass and energy flux across the interface. More precisely, the numerical flux has to fulfil

$$\mathcal{F}(\mathbf{w}^L, \mathbf{w}^R) = \mathcal{F}([\rho_L, 0, p]^T, [\rho_R, 0, p]^T) = [0, 0, p]^T \tag{2.97}$$

given that $p = p_L = p_R$. Therefore, we note that that the scheme maintains the discrete hydrostatic equilibrium (2.82) for arbitrary $K(x)$, i.e. arbitrary entropy stratification, in particular for the HLLC and Roe approximate Riemann solver.

2.2.4 Second order one-dimensional schemes: higher order hydrostatic reconstruction

Due to the limited practical use of first order schemes, a higher order extension is needed. We will design a second order accurate in both space and time finite volume scheme which maintains the discrete hydrostatic equilibrium (2.82) exactly.

A semi-discrete scheme may be written as

$$\frac{d\mathbf{u}_i}{dt} = -\frac{1}{\Delta x} (\mathbf{F}_{i+1/2} - \mathbf{F}_{i-1/2}) + \mathbf{S}_i, \tag{2.98}$$

where $\mathbf{F}_{i+1/2} = \mathcal{F}(\mathbf{u}_{i+1/2}^L, \mathbf{u}_{i+1/2}^R)$ is the numerical flux and \mathbf{S}_i the gravity source term.

In subsection 2.1.3, we have discussed a higher order extension by flux reconstruction. The flux reconstruction can directly be performed on the basis of the numerical fluxes obtained after hydrostatic reconstruction. This ensures that any discrete equilibrium of the form (2.82) is exactly (or within round-off errors) preserved and that only deviations from equilibrium are used in the flux reconstruction.

Another way to increase the spatial resolution is obtained by replacing the piece-wise constant approximation of the conserved variables by a higher-order non-oscillatory reconstructions, see e.g. [85, 92, 159]. Since we are seeking a spatially second order accurate scheme, we will use a common piece-wise linear reconstruction with TVD limiters [165]. As a matter of fact, other reconstructions like ENO [61] or WENO [146] are possible and these permit even higher orders of accuracy.

TVD equilibrium reconstruction

A standard piece-wise linear reconstruction of the conserved variables may not preserve the discrete hydrostatic equilibrium.

Since the hydrostatic reconstruction already maintains to second order accuracy stationary states, only the deviations from this discrete equilibrium should be used in the computation of the slopes for the piece-wise linear reconstruction. Therefore, we propose to not simply reconstruct $\mathbf{u}_i(x)$ from cell averages \mathbf{u}_i , but rather the difference $\tilde{\mathbf{u}}_i(x) = \mathbf{u}_i(x) - \mathbf{u}_i$

$$\tilde{\mathbf{u}}_i(x) = \tilde{\sigma}_i(x - x_i) \quad \text{for } x \in [x_{i-1/2}, x_{i+1/2}], \quad (2.99)$$

where $\tilde{\sigma}_i$ is a slope. When computing the slope $\tilde{\sigma}_i$, we also subtract the hydrostatic differences (2.94) in the conserved variables

$$\tilde{\sigma}_i = \varphi \left(\frac{\mathbf{u}_i - \mathbf{u}_{i-1} - (\Delta \mathbf{u}_{i-1}^+ + \Delta \mathbf{u}_i^-)}{\Delta x}, \frac{\mathbf{u}_{i+1} - \mathbf{u}_i - (\Delta \mathbf{u}_i^+ + \Delta \mathbf{u}_{i+1}^-)}{\Delta x} \right), \quad (2.100)$$

where φ is a flux limiter. We have used the minmod limiter

$$\varphi(a, b) = \text{minmod}(a, b) = \frac{1}{2} (\text{sign}(a) + \text{sign}(b)) \min(|a|, |b|), \quad (2.101)$$

where the limiter is applied component-wise. Other choices for the limiter are possible and we refer to e.g. [85, 92, 150, 159].

The cell interface extrapolated conserved variables are then evaluated by

$$\begin{aligned} \mathbf{u}_{i+1/2}^L &= \mathbf{u}_i + \Delta \mathbf{u}_i^+ + \tilde{\sigma}_i \frac{\Delta x}{2} \\ \mathbf{u}_{i+1/2}^R &= \mathbf{u}_{i+1} - \Delta \mathbf{u}_{i+1}^- - \tilde{\sigma}_{i+1} \frac{\Delta x}{2}. \end{aligned} \quad (2.102)$$

The reconstruction amounts to approximate the slope of only the deviations from hydrostatic equilibrium. It is straightforward to show that the outlined second order TVD reconstruction is well-balanced with respect to the discrete hydrostatic equilibrium eq. (2.82). Similar approaches have been devised in [21].

Time stepping

For temporal second order accuracy, we use a simple predictor-corrector method. As a predictor, we compute a half time step with the well-balanced first order scheme (2.65).

In the corrector step, we then use the calculated values from the predictor step $\mathbf{u}^{n+1/2}$ as input for the above second order TVD equilibrium reconstruction:

$$\mathbf{u}_i^{n+1} = \mathbf{u}_i^n - \frac{\Delta t}{\Delta x} \left(\mathbf{F}_{i+1/2}^{n+1/2} - \mathbf{F}_{i-1/2}^{n+1/2} \right) + \Delta t \mathbf{S}_i^{n+1/2}. \quad (2.103)$$

The source term is given by eq. (2.96).

2.2.5 Extension beyond one dimension

The extension of the well-balanced hydrostatic reconstruction to two dimensions is shown for convenience and the extension to three dimensions is straightforward. The equations of hydrodynamics are then given by

$$\frac{\partial \mathbf{u}}{\partial t} + \frac{\partial \mathbf{F}}{\partial x} + \frac{\partial \mathbf{G}}{\partial y} = \mathbf{S}, \quad (2.104)$$

where

$$\mathbf{u} = \begin{bmatrix} \rho \\ \rho v_x \\ \rho v_y \\ E \end{bmatrix}, \quad \mathbf{F} = \begin{bmatrix} \rho v_x \\ \rho v_x^2 + p \\ \rho v_y v_x \\ (E + p)v_x \end{bmatrix}, \quad \mathbf{G} = \begin{bmatrix} \rho v_y \\ \rho v_x v_y \\ \rho v_y^2 + p \\ (E + p)v_y \end{bmatrix} \quad (2.105)$$

and

$$\mathbf{S} = \mathbf{S}_x + \mathbf{S}_y = \begin{bmatrix} 0 \\ \rho \\ 0 \\ \rho v_x \end{bmatrix} \frac{\partial \phi}{\partial x} + \begin{bmatrix} 0 \\ 0 \\ \rho \\ \rho v_y \end{bmatrix} \frac{\partial \phi}{\partial y}. \quad (2.106)$$

The primitive variables vector is then $\mathbf{w} = [\rho, v_x, v_y, p]^T$. While the hydrostatic reconstruction is independent of the way one solves the 2D equations (dimensionally split or unsplit), we shall use a dimensionally split approach in order to comply with the FISH code.

The hydrostatic reconstruction is then applied in each direction separately and we will describe the scheme in x -direction. Similar to the description in subsection 2.1.3, we drop the indices of the ignored y -direction. The only change is that in x - (y -) direction we have ρv_y (ρv_x) that represents a passive scalar, i.e. the tangential velocity components are passive scalars in the solution process of the directionally split Riemann problem. In x -direction, if the system is moving in tangential direction $v_y \neq 0$, the velocity v_y should be left unchanged by the hydrostatic reconstruction: $v_{y,i+1/2}^{n,L} = v_{y,i}^n$ and $v_{y,i+1/2}^{n,R} = v_{y,i+1}^n$. This motivates the following hydrostatic reconstructed interface tangential momentum densities:

$$\begin{aligned} \rho v_{y,i+1/2}^{n,L} &= \rho_{i+1/2}^{n,L} v_{y,i} \\ \rho v_{y,i+1/2}^{n,R} &= \rho_{i+1/2}^{n,R} v_{y,i+1}. \end{aligned} \quad (2.107)$$

We then define the hydrostatic ρv_y momentum differences as

$$\begin{aligned} \Delta \rho v_{y,i}^{n,+} &= \rho v_{y,i+1/2}^{n,L} - \rho v_{y,i}^n \\ \Delta \rho v_{y,i}^{n,-} &= \rho v_{y,i}^n - \rho v_{y,i-1/2}^{n,R}. \end{aligned} \quad (2.108)$$

In x -direction, the hydrostatic reconstruction can then be compactly written as (2.92) for the conserved variables and as (2.93) for the primitive variables. The 2D x -split hydrostatic

differences in conserved and primitive variables are given by

$$\Delta \mathbf{u}_i^{n,\pm} = \begin{bmatrix} \Delta \rho_i^{n,\pm} \\ \Delta \rho v_{x,i}^{n,\pm} \\ \Delta \rho v_{y,i}^{n,\pm} \\ \Delta E_i^{n,\pm} \end{bmatrix} \quad \text{and} \quad \Delta \mathbf{w}_i^{n,\pm} = \begin{bmatrix} \Delta \rho_i^{n,\pm} \\ 0 \\ 0 \\ \Delta p_i^{n,\pm} \end{bmatrix}. \quad (2.109)$$

The corresponding expressions for the hydrostatic reconstruction in y -direction follow by analogy.

As for the one-dimensional case, one can compute the momentum component of the numerical flux divergence (for the 2D equations) and this suggests the following discretisation of the gravitational source term:

$$\mathbf{S}_{x,i}^n = - \begin{bmatrix} 0 \\ \frac{1}{2} \left(\frac{\rho_{i-1}^n + \rho_i^n}{2} \frac{\phi_i - \phi_{i-1}}{\Delta x} + \frac{\rho_i^n + \rho_{i+1}^n}{2} \frac{\phi_{i+1} - \phi_i}{\Delta x} \right) \\ 0 \\ \rho v_{x,i}^n \frac{\phi_{i+1} - \phi_{i-1}}{2\Delta x} \end{bmatrix}. \quad (2.110)$$

The energy source term uses a simple central discretisation.

It follows from a simple calculation, that the hydrostatic reconstruction applied on a per dimension basis together with the x -direction source term eq. (2.110) and the appropriate source term in y -direction preserves exactly any discrete equilibrium of the form

$$\begin{aligned} \frac{p_{i+1,j}^n - p_{i,j}^n}{\Delta x} &= - \frac{\rho_{i,j}^n + \rho_{i+1,j}^n}{2} \frac{\phi_{i+1,j} - \phi_{i,j}}{\Delta x} \\ \frac{p_{i,j+1}^n - p_{i,j}^n}{\Delta y} &= - \frac{\rho_{i,j}^n + \rho_{i,j+1}^n}{2} \frac{\phi_{i,j+1} - \phi_{i,j}}{\Delta y}. \end{aligned} \quad (2.111)$$

This will also be demonstrated in three-dimension in subsection 2.2.7. Furthermore, spatial second order accuracy is also achieved on a per dimension basis as described in subsection 2.2.4.

2.2.6 Extension to general equation of states and MHD: approximately-balanced schemes

In many applications, the equation of state is more complicated than the ideal gas law. For example in CCSN simulation, we use tabulated EoS due to the complexity of the state description at the encountered extreme conditions. Furthermore, EoS evaluations are often computationally intensive (e.g. table look-up) and one wants to avoid any superfluous EoS calls. Therefore, it may be difficult to obtain from the hydrostatically reconstructed pressure $p(\rho, \rho e)$ the associated density and internal energy density.

If we again assume the entropy to be constant inside each cell, then we can express the hydrostatic pressure gradient by

$$\frac{\partial p}{\partial x} = \left(\frac{\partial p}{\partial \rho} \right)_s \frac{\partial \rho}{\partial x} = c^2 \frac{\partial \rho}{\partial x}, \quad (2.112)$$

where c is the speed of sound. With eq. (2.112), we can then express approximately the hydrostatic density differences with

$$\Delta p_i^{n,\pm} = c_i^2 \Delta \rho_i^{n,\pm}, \quad (2.113)$$

where c_i is the speed of sound in the cell and $\Delta p_i^{n,\pm}$ is the hydrostatic pressure difference as computed in eq. (2.83).

Using the fundamental thermodynamic relation $de = -pdV$ and relation (2.112), we can express the hydrostatic internal energy density gradient by

$$\frac{\partial \rho e}{\partial x} = \left(e + \frac{p}{\rho} \right) \frac{\partial \rho}{\partial x}. \quad (2.114)$$

With eq. (2.114), we can then express approximately the hydrostatic internal energy density differences with

$$\Delta \rho e_i^{n,\pm} = \left(e_i + \frac{p_i}{\rho_i} \right) \Delta \rho_i^{n,\pm}. \quad (2.115)$$

The hydrostatic total energy density differences follow immediately from the above.

The just outlined hydrostatic and internal energy density reconstruction is not exact. Hence, we call the scheme using these differences an approximately-balanced scheme. This scheme will not guarantee that a discrete hydrostatic state is maintained exactly. However, we will confirm in a numerical experiment in the next subsection 2.2.7, that the scheme performs very well and is therefore well suited for the simulation of (near) hydrostatic objects with complex EoS.

Furthermore, the just outlined hydrostatic reconstruction for general EoS is only directly applicable to hydrodynamics. However, since the magnetic field is usually playing a minor role in regions where (near) hydrostatic equilibrium prevails, we have found that replacing the acoustic sound speed by the fast magnetosonic speed works well and in a stable manner for MHD simulations as well. This extension is implemented into `FISH` and is used in our CCSN simulations.

2.2.7 Numerical results

In this section, we numerically test the first order (2.65) and second order (2.103) well-balanced schemes on a series of numerical problems. For comparison, we also consider unbalanced versions of the schemes by switching off the hydrostatic reconstruction, but still using the discretisation (2.96) of the source term.

In all tests we use equidistant Cartesian grids. The time step is chosen according a suitable CFL condition and a CFL number of 0.9.

To construct the equilibrium models, we use the polytropic relation between pressure and density $p = K(S)\rho^\gamma$, where the coefficient $K = K(S)$ is a function of entropy S . The internal energy density is then simply computed via eq. (2.61).

To characterise a timescale on which a model reacts to perturbations of its equilibrium, we define the sound crossing time τ_{sound}

$$\tau_{\text{sound}} = 2 \int_{x_0}^{x_1} \frac{dx}{c}, \quad (2.116)$$

where $c = (\gamma p/\rho)^{1/2}$ is the speed of sound and the integral has to be taken over the extent of the steady configuration of interest.

We quantify the accuracy of the schemes by computing the errors

$$Err = \frac{1}{N} \sum_i |q_i - q_i^{\text{ref}}|, \quad (2.117)$$

where the sum runs over all N cells in the domain of interest. Here q is a selected relevant quantity (e.g. density, pressure) and q^{ref} is the reference solution, i.e. the steady state to be maintained discretely or an interpolated numerically obtained reference solution on a very fine grid. While the comparison with a numerically obtained reference solution does not provide a rigorous evidence of convergence, it nevertheless indicates a meaningful measure of the errors.

One-dimensional hydrostatic atmosphere in a constant gravitational field: well-balanced property and wave propagation

Our first numerical test problem considers the very simple setting of a one-dimensional atmosphere in a constant gravitational field in hydrostatic equilibrium. The potential is then a simple linear function

$$\phi(x) = gx, \quad (2.118)$$

where g is a constant set to $g = 1$. We have set $\gamma = 5/3$.

We set the computational domain to $x \in [0, L]$ with $L = 2$ discretised by N cells. The density cell averages are initialised by solving numerically

$$\frac{p_{i+1} - p_i}{\Delta x} = -\frac{\rho_i + \rho_{i+1}}{2} \frac{\phi_{i+1} - \phi_i}{\Delta x} \quad (2.119)$$

for $i = 2, \dots, N$ with $\phi_i = \phi(x_i)$ and $\Delta x = L/N$. The pressure $p_i = K(x_i)\rho_i^\gamma$ is a function of density alone once $K(x)$ is given (see below). The first cell is initialised by solving

$$\frac{p_1 - p(0)}{\Delta x/2} = -\frac{\rho(0) + \rho_1}{2} \frac{\phi_1 - \phi(0)}{\Delta x/2}, \quad (2.120)$$

where the density at the base is $\rho(0) = 1$ and the pressure $p(0) = K(0)$. The velocity is set to zero and the total energy is computed by $E_i = p_i/(\gamma - 1)$.

For the boundary conditions, we perform a hydrostatic extrapolation of the density and the pressure and a zero order extrapolation of the velocity. Explicitly, we have used the following prescription at the lower boundary

$$\begin{aligned} \frac{p_{1-m} - p_{1-(m-1)}}{\Delta x} &= -\frac{\rho_{1-(m-1)} + \rho_{1-m}}{2} \frac{\phi_{1-m} - \phi_{1-(m-1)}}{\Delta x} \\ v_{x,1-m} &= v_{x,1-(m-1)} \end{aligned} \quad (2.121)$$

and similarly at the upper boundary

$$\begin{aligned} \frac{p_{N+m} - p_{N+(m-1)}}{\Delta x} &= -\frac{\rho_{N+(m-1)} + \rho_{N+m}}{2} \frac{\phi_{N+m} - \phi_{N+(m-1)}}{\Delta x} \\ v_{x,N+m} &= v_{x,N+(m-1)}, \end{aligned} \quad (2.122)$$

where $m = 1, \dots, M$. M is the number of ghost cells. Note that again the equations for the density have to be solved numerically. The coefficient K is also constantly extrapolated $K_{1-m} = K_{1-(m-1)}$ and $K_{N+m} = K_{N+(m-1)}$.

Well-balanced property

We first numerically verify the well-balanced property of the first and second order schemes for different choices of the coefficient $K(x)$. We use the following expressions

$$K_1(x) = 1 \tag{2.123}$$

$$K_2(x) = 1 + 0.1 \sin\left(\frac{2\pi x}{L}\right) \tag{2.124}$$

$$K_3(x) = \begin{cases} 2 & \text{if } x < 1 \\ 1 & \text{if } x \geq 1 \end{cases} . \tag{2.125}$$

Since K is a function of entropy, we therefore test the performance of the schemes on different entropy stratifications.

We then evolved the initial condition for the three different entropy stratifications with the resolutions $N = 64, 128, 256, 512$ for one sound crossing time: $t = 4.28, 4.28, 2.86$ for K_1, K_2 and K_3 , respectively.

The numerical errors in density for the first order schemes and entropy stratification K_1 are shown in table 2.1. We see that the well-balanced schemes maintain the stationary state up to machine precision for all numerical fluxes and independently of the spatial resolution. On the other hand, the unbalanced schemes show large errors.

Tables 2.2 and 2.3 show the numerical errors in density for the K_2 and K_2 entropy stratifications. We confirm by experiment the fact that only the well-balanced schemes with a numerical flux resolving the contact discontinuity (HLLC and Roe) are able to maintain the discrete hydrostatic equilibrium within round-off errors and this independently of the spatial resolution. However, the unbalanced schemes show large deviations from equilibrium with all numerical fluxes and these errors tend to zero with the expected first order convergence.

N	LxF	HLL	HLLC	Roe
64	2.57E-02/4.50E-16	2.57E-02/5.19E-16	2.58E-02/5.82E-15	2.56E-02/2.48E-15
128	1.30E-02/2.17E-15	1.30E-02/2.40E-16	2.30E-02/6.51E-15	1.30E-03/6.49E-16
256	6.53E-03/9.63E-15	6.53E-03/4.81E-16	6.53E-03/4.39E-15	6.52E-03/8.99E-16
512	3.27E-03/1.98E-15	3.27E-03/1.78E-15	3.27E-03/4.15E-14	3.26E-03/1.04E-14

Table 2.1: Error in density for the one-dimensional hydrostatic atmosphere and entropy stratifications K_1 for the unbalanced/balanced first order schemes and the different numerical fluxes.

N	LxF	HLL	HLLC	Roe
64	2.42E-02/8.21E-03	2.42E-02/8.21E-03	2.81E-02/5.11E-15	2.69E-02/2.84E-15
128	1.31E-02/5.79E-03	1.31E-02/5.79E-03	1.42E-02/8.54E-16	1.37E-02/1.65E-15
256	7.16E-03/3.65E-03	7.15E-03/3.65E-03	7.17E-03/2.03E-14	6.88E-03/1.59E-14
512	3.89E-03/2.14E-03	3.89E-03/2.14E-03	3.60E-03/6.40E-14	3.45E-03/5.33E-14

Table 2.2: Error in density for the one-dimensional hydrostatic atmosphere and entropy stratifications K_2 for the unbalanced/balanced first order schemes and the different numerical fluxes.

In tables 2.4, 2.5 and 2.6 the errors in density for the second order schemes and entropy stratifications K_1, K_2 and K_3 , respectively, are displayed. Here we also observe that

N	LxF	HLL	HLLC	Roe
64	5.32E-02/5.15E-02	5.32E-02/5.14E-02	1.20E-02/1.03E-14	1.26E-02/3.86E-15
128	3.87E-02/3.72E-02	3.87E-02/3.72E-02	6.22E-03/8.72E-15	6.55E-03/4.85E-15
256	2.76E-02/2.66E-02	2.76E-02/2.66E-02	3.17E-03/7.07E-15	3.35E-03/9.28E-15
512	1.95E-02/1.89E-02	1.95E-02/1.89E-02	1.60E-03/5.54E-15	1.69E-03/7.79E-15

Table 2.3: Error in density for the one-dimensional hydrostatic atmosphere and entropy stratifications K_3 for the unbalanced/balanced first order schemes and the different numerical fluxes.

the discrete equilibrium for arbitrary entropy stratifications is only guaranteed for the well-balanced scheme with a numerical flux that resolves the contact discontinuity. As expected, this result is independent of the spatial resolution. The errors for the second order unbalanced schemes show the expected decrease.

N	LxF	HLL	HLLC	Roe
64	7.21E-05/1.48E-15	7.26E-05/4.07E-15	5.81E-05/1.11E-15	5.64E-05/1.60E-15
128	1.74E-05/5.90E-16	1.75E-05/4.87E-16	1.58E-05/8.01E-16	1.55E-05/5.50E-16
256	4.29E-06/5.58E-16	4.29E-06/9.93E-16	4.11E-06/2.77E-15	4.07E-06/8.58E-16
512	1.07E-06/3.38E-15	1.07E-06/1.23E-15	1.05E-06/1.50E-14	1.04E-06/1.25E-15

Table 2.4: Error in density for the one-dimensional hydrostatic atmosphere and entropy stratifications K_1 for the unbalanced/balanced second order schemes and the different numerical fluxes.

N	LxF	HLL	HLLC	Roe
64	1.41E-03/1.96E-03	1.41E-03/1.96E-03	5.64E-03/3.41E-15	1.34E-03/4.63E-16
128	5.78E-04/7.67E-04	5.78E-04/7.67E-04	2.96E-03/2.02E-15	6.92E-04/1.74E-15
256	2.40E-04/3.02E-04	2.40E-04/3.02E-04	1.52E-03/5.11E-14	3.55E-04/2.27E-14
512	1.02E-04/1.17E-04	1.02E-04/1.17E-04	7.71E-04/1.64E-15	1.81E-04/1.14E-15

Table 2.5: Error in density for the one-dimensional hydrostatic atmosphere and entropy stratifications K_2 for the unbalanced/balanced second order schemes and the different numerical fluxes.

N	LxF	HLL	HLLC	Roe
64	2.40E-02/1.98E-02	2.40E-02/1.98E-02	1.39E-04/1.36E-15	4.55E-04/6.87E-16
128	1.47E-02/1.27E-02	1.47E-02/1.27E-02	3.91E-05/8.11E-15	2.38E-04/8.54E-16
256	8.93E-03/8.05E-03	8.93E-03/8.05E-03	1.02E-05/6.02E-15	1.21E-04/1.61E-15
512	5.47E-03/5.10E-03	5.47E-03/5.10E-03	2.61E-05/2.52E-14	6.08E-05/1.35E-14

Table 2.6: Error in density for the one-dimensional hydrostatic atmosphere and entropy stratifications K_3 for the unbalanced/balanced second order schemes and the different numerical fluxes.

From the performed tests, we conclude that the well-balanced schemes for both first and second order accuracy show the theoretically expected ability to maintain discrete equilibria. This experiment illustrates the contrast between the unbalanced schemes and their well-balanced counterparts.

Wave propagation

As a second test, we check the capability of the second order schemes to propagate waves on the static background of our first test with K_1 entropy stratification by imposing a periodic velocity perturbation at the lower boundary

$$v_0^n = A \sin(6\pi t^n). \quad (2.126)$$

The excited waves move through the domain and are modified by the density and pressure gradient induced by gravity. We perform two different tests: a small and a large amplitude perturbation. For the small amplitude perturbation we set $A = 10^{-6}$. Figure 2.23 shows the velocity and the density deviation (from equilibrium) at time $t = 1.8$, just before the waves reach the upper boundary, for the unbalanced (solid red line) and the well-balanced (dash dotted red line) schemes with the HLLC numerical flux for $N = 256$.

As a reference solution, a high resolution $N = 4096$ simulation with the well-balanced scheme and the HLLC is also shown in the figure (solid blue line). We observe that the well-balanced scheme nicely resolves the wave pattern. On the other hand, the unbalanced scheme suffers from large spurious deviations. As a matter of fact, the induced density perturbation ($\sim 10^{-6}$ from the figure) is either of the same order or orders of magnitude smaller (see table 2.4) than the errors of the unbalanced schemes. This illustrates the superiority of the well-balanced schemes for this type of problems.

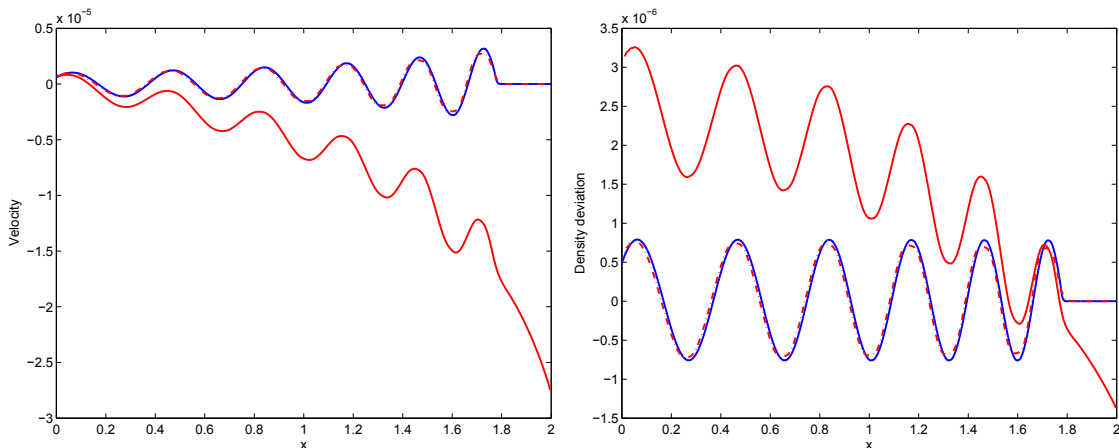


Figure 2.23: Plot of the velocity (left) and the density equilibrium deviation (right) for the small amplitude $A = 10^{-6}$ perturbation on a hydrostatic background. The blue line is the reference solution, the red solid/dash-dotted line was computed with the unbalanced/well-balanced second order scheme, both with HLLC and $N = 256$. The well-balanced scheme is clearly able to resolve the small perturbations, while the unbalanced scheme suffers from spurious deviations.

In order to check that the hydrostatic reconstruction does not interfere negatively with the robustness of the base high-resolution shock-capturing finite volume scheme, we also tested the propagation of large amplitude $A = 0.1$ waves until $t = 1.8$ (shortly before the waves reach the upper boundary). The errors are displayed in table 2.7. The errors were computed on the basis of a reference solution computed with the well-balanced scheme and the HLLC at high resolution $N = 4096$. Both, the unbalanced and the well-balance second order schemes show a rate of convergence close to one and the errors are of comparable size. This is to be expected, because the sine waves steepen into saw-tooth waves while

propagating down the density gradient. This is displayed in figure 2.24. The large amplitude test illustrates that the hydrostatic reconstruction does not diminish the accuracy and the robustness of the base high-resolution shock-capturing scheme.

N	LxF	HLL	HLLC	Roe
64	2.01E-02/2.47E-02	1.97E-02/2.44E-02	2.02E-02/2.44E-02	2.01E-02/2.44E-02
128	1.27E-02/1.47E-02	1.18E-02/1.44E-02	1.21E-02/1.43E-02	1.20E-02/1.43E-02
256	5.21E-03/6.56E-03	4.62E-03/5.99E-03	4.71E-03/5.93E-03	4.67E-03/5.92E-03
512	3.30E-03/3.16E-03	3.01E-03/2.85E-03	3.01E-03/2.76E-03	3.00E-03/2.75E-03

Table 2.7: Error in density for the large amplitude perturbation and entropy stratifications K_1 for the unbalanced/balanced second order schemes and the different numerical fluxes.

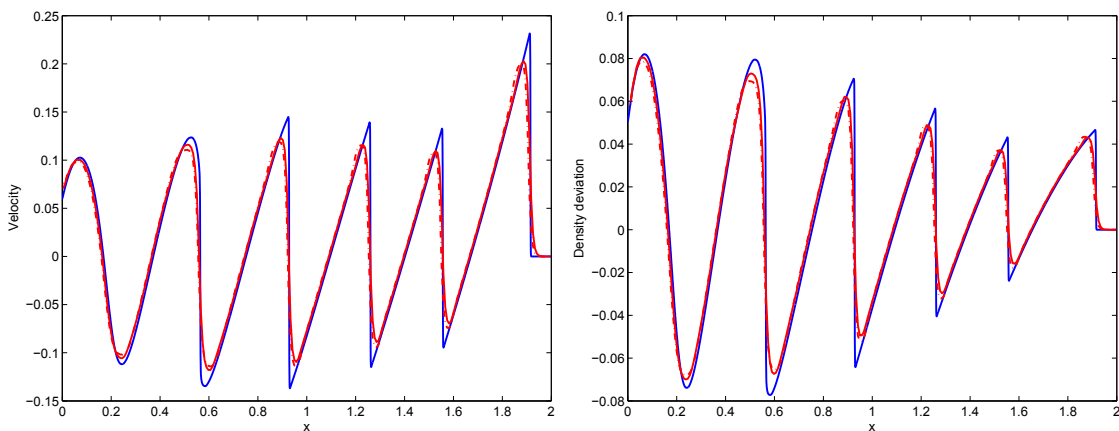


Figure 2.24: Plot of the velocity (left) and the density equilibrium deviation (right) for the large amplitude $A = 0.1$ perturbation on a hydrostatic background. The blue line is the reference solution, the red solid/dash-dotted line was computed with the unbalanced/well-balanced second order scheme, both with HLLC and $N = 256$. Both schemes are able to capture the large amplitude perturbations and their steepening down the density profile.

Three-dimensional steady polytrope

As a three-dimensional test, we show the performance of our hydrostatic reconstruction scheme on an astrophysical problem. We simulate a static configuration of an adiabatic gaseous sphere held together by self-gravitation, a so-called polytrope [37]. Here we test our implementation of the second order well-balanced and the approximately-balanced scheme into FISH. Note that FISH uses a flux reconstruction to achieve spatial second order accuracy and a numerical flux equivalent to the Lax-Friedrichs.

These model stars are constructed from hydrostatic equilibrium

$$\frac{dp}{dr} = -\rho \frac{d\phi}{dr} \quad (2.127)$$

and Poisson's equation in spherical symmetry

$$\frac{1}{r^2} \frac{d}{dr} \left(r^2 \frac{d\phi}{dr} \right) = 4\pi G\rho, \quad (2.128)$$

where r is the radial variable and G is the gravitational constant.

With help of the polytropic relation $p = K\rho^\gamma$, eq. (2.127) and (2.128) can be combined into a single equation

$$\frac{1}{r^2} \frac{d}{dr} \left(r^2 \gamma K \frac{d\rho}{dr} \right) = -4\pi G \rho, \quad (2.129)$$

which is known as the Lane-Emden equation. To this equation, there exist three analytical solutions for $\gamma = 6/5, 2, \infty$ [37].

We will use $\gamma = 2$ since neutron stars can be modelled by $\gamma = 2 - 3$ and since there exists an analytical solution to eq. (2.129). The density is then given by

$$\rho(r) = \rho_c \frac{\sin(\alpha r)}{\alpha r}, \quad (2.130)$$

where

$$\alpha = \sqrt{\frac{4\pi G}{2K}} \quad (2.131)$$

and ρ_c is the central density of the polytrope. The gravitational potential is given by

$$\phi(r) = -2K\rho(r). \quad (2.132)$$

We use for the model constants $K = G = \rho_c = 1$.

We then initialised the density profile (2.130), internal energy profile ($\rho e = p/(\gamma - 1)$) and gravitational potential (2.132) onto a regular Cartesian domain of size $(x, y, z) \in [-0.65, 0.65]^3$ discretised by N^3 grid cells. The radius is $r^2 = x^2 + y^2 + z^2$. The velocity is set to zero in the full domain. For the boundary condition, we have used the same hydrostatic extrapolation of the density and the pressure and a zero order extrapolation of the velocity as in the above one-dimensional tests. The boundary condition is applied in each direction and the gravitational potential in the boundary is given by the analytical solution. We note that the initialised hydrostatic configuration fulfils the discrete equilibrium exactly eq. (2.111) (generalised to three-dimensions).

We then evolved the initial conditions for 20 sound crossing times $t = 20\tau_{\text{sound}}$, where $\tau_{\text{sound}} \approx 1$. We have used two resolutions: $N = 64^3$ and $N = 128^3$. For comparison, we also tested the standard unsplit integration of the gravitational source terms described in 2.1.5. Note that the gravitational potential is kept fixed during the simulation, i.e. we do not use self-gravity.

The numerical errors for this test are shown in table 2.8 for the unbalanced, approximately-balanced and well-balanced schemes. From the table, we observe that the well-balanced scheme resolves the stationary state within machine precision. Therefore, we conclude that our dimension-by-dimension hydrostatic reconstruction works as expected. On the other hand, the approximately-balanced and the unbalanced show some deviations. However, the errors in the approximately-balanced are two orders of magnitude lower than in the unbalanced case.

In figure 2.25, we display the central density as a function of time for the well-balanced (blue solid line), the approximately-balanced (dash-dotted red line) and the unbalanced (solid red line) schemes. We see that the well-balanced and the approximately-balanced show a near indistinguishable central density. On the other hand, the unbalanced scheme seems not to be able to hold the discrete hydrostatic equilibrium of the polytrope. In figure 2.26, we show the initial density profile (blue solid line) and the profile for the approximately-balanced (dash-dotted red line) and the unbalanced (solid red line) scheme at the final time. The profile of the gravitational potential is also shown. From the figure,

we observe that the approximately balanced scheme can hold the equilibrium profile very well, while the unbalanced scheme suffers from spurious deviations.

Here we have numerically demonstrated, that the hydrostatic reconstruction is well-balanced with respect to discrete equilibrium in the form (2.111) (generalised to three-dimensions). Furthermore, it is clear that the approximately-balanced scheme improves greatly the numerical resolution of equilibrium configurations with respect to the unbalanced scheme.

N	unbalanced	approx.-balanced	well-balanced
64	1.88E-02	3.41E-04	1.19E-15
128	2.73E-03	4.87E-05	3.41E-15

Table 2.8: Error in density for the 3D polytrope for the second order unbalanced, approximately-balanced and well-balanced schemes.

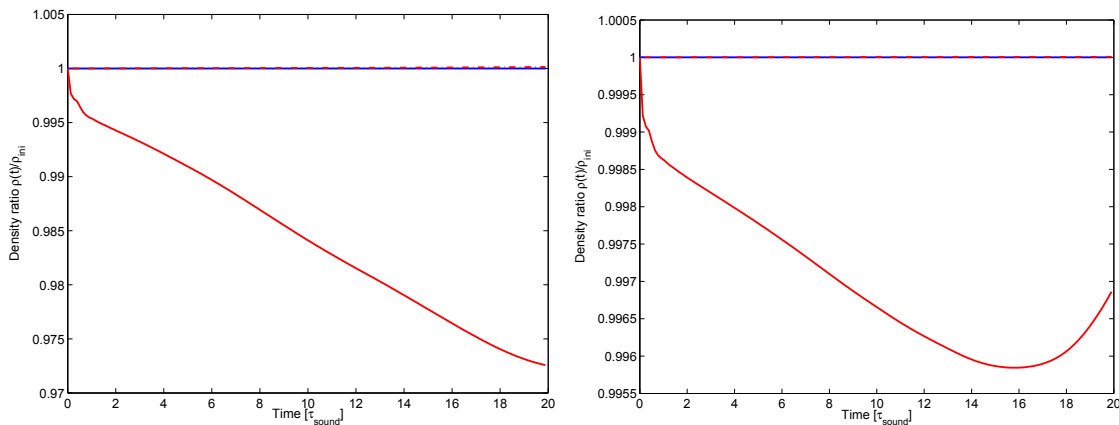


Figure 2.25: The central density normalised to the exact value as a function of time is shown for the second order unbalanced (solid red line), approximately-balanced (dash-dotted red line) and well-balanced schemes (solid blue line). The left panel was computed with 64^3 computational cells and the right panel with 128^3 . The approximately and well-balanced simulations are nearly indistinguishable, while the unbalanced ones suffer from deviations from the exact value.

2.3 Gravitation

In this section we detail the numerical methods used to solve the Poisson equation

$$\nabla^2 \phi = 4\pi G \rho, \quad (2.133)$$

where ϕ is the gravitational potential, ρ the mass density and G the gravitational constant. In contrast with the hyperbolic MHD equations, the Poisson equation is an elliptic partial differential equation (PDE). While the MHD equations propagate physical information at a finite speed, the Poisson equations propagates information instantly, i.e. at infinite speed. This has some important consequences concerning the efficient parallel implementation of a solver for elliptic PDEs. After a straightforward domain decomposition of a hyperbolic problem, one parallel working unit needs only to communicate with its imme-

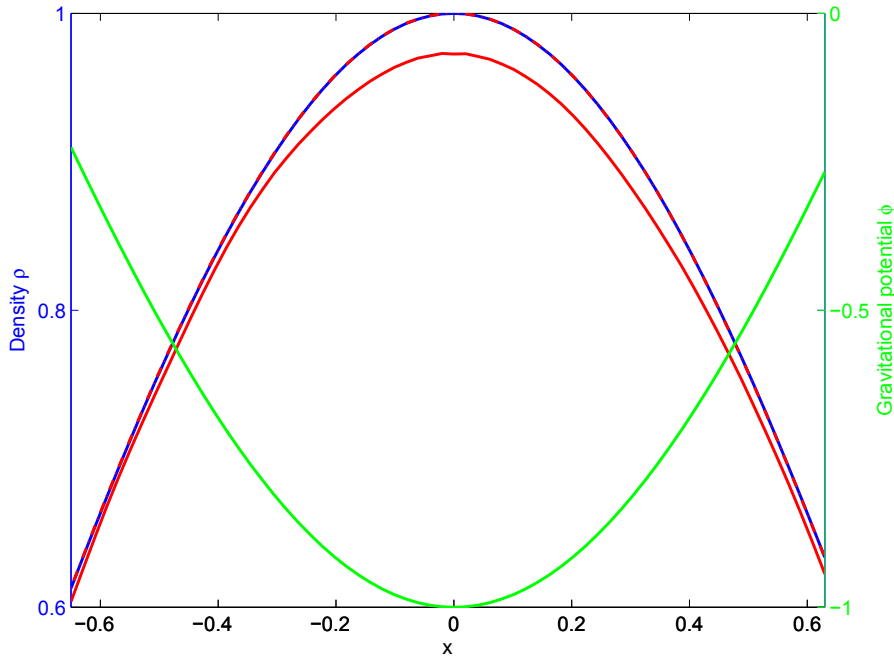


Figure 2.26: The figure shows the initial density profile (blue line), the gravitational potential (green line) and the density at the end of the simulation for the unbalanced and the approximately-balanced second order schemes and 64^3 cells. The profiles have been plotted along the x axis and $y = z = 0$.

diante neighbours for one time step¹. On the other hand, to compute the solution for an elliptic problem the entire domain has to be available for each parallel unit.

There exist several highly efficient algorithms, which alleviate this communication bottleneck by a divide-and-conquer approach (e.g. Barnes-Hut [14], fast multipole method [58], ...). Another related approach proceeds by dimensional reduction, where the original problem is approximated in lower dimensions. This has also the effect of reducing the communication demand during the solution process.

We have followed the latter approach, where our 3D Cartesian domain is reduced to a 2D axisymmetric or to a 1D spherically symmetric domain. The details of the method and its implementation are presented in the following subsections.

2.3.1 Gravity in spherical symmetry and general relativistic corrections

In the case of non- or slowly rotating stars, the mass distribution may be reasonably well approximated by a spherically symmetric distribution. This approximation remains reasonable as long as centrifugal forces don't produce significant deformations of the rotating star or convection leads to strong density anisotropies. The Poisson equation in spherical coordinates is then given by

$$\frac{1}{r^2} \frac{\partial}{\partial r} \left(r^2 \frac{\partial \phi}{\partial r} \right) = 4\pi G \rho, \quad (2.134)$$

¹This time step has to be of course small enough that information does not travel more than one extent of a parallel working unit.

which can be integrated once to get

$$\frac{\partial\phi}{\partial r} = \frac{GM}{r^2}, \quad (2.135)$$

where

$$M(r) = \int_0^r 4\pi\rho r^2 dr \quad (2.136)$$

is the spherical symmetric mass distribution. Here $\phi = \phi(r)$ is the gravitational potential, $\rho = \rho(r)$ the spherically symmetric density distribution and G the gravitational constant. Once $\rho(r)$ is specified, eq. (2.134) or (2.135) can be integrated in a straightforward manner. The spherically symmetric density distribution $\rho(r)$ is obtained by a conservative mapping from the 3D Cartesian domain to 1D spherical symmetry. The 1D spherical domain is chosen to be the biggest sphere fully contained in the 3D domain (see figure 2.27).

In a parallel distributed memory context, this mapping requires the call to a collective communication routine (`MPI_ALL_REDUCE`) to sum up the contributions from all processes to $\rho(r)$. Then each process has the spherically symmetric density and can integrate eq. (2.134) or (2.135) to obtain the spherical symmetric gravitational potential. The obtained potential $\phi(r)$ is then mapped onto the process's local 3D domain. Since each process holds the spherical symmetric potential for the full domain, no communication is required during this step.

The most expensive part in terms of wall-clock time and a potential parallel scaling bottleneck for the procedure outlined above is the collective communication required for the construction of the spherical symmetric density distribution $\rho(r)$. But due to the low amount of data ($\sim \sqrt{3} \min(N_x, N_y, N_z)/2$, where $N_{x,y,z}$ is the number of cells in the respective direction) that has to be communicated collectively, the overall solution process takes less than $\sim 1\%$ of the time required for a MHD step and is therefore quite efficient.

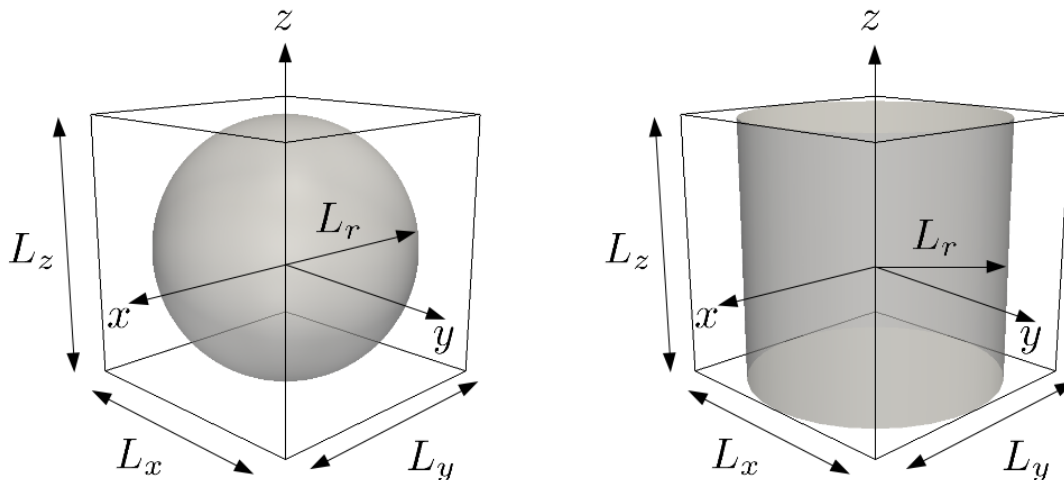


Figure 2.27: The 3D Cartesian domain of size L_x, L_y, L_z with the embedded 1D spherically symmetric domain (left) and the 2D axisymmetric cylindrical domain (right). The size of the sphere is given by $L_r = \min(L_x, L_y, L_z)/2$. The size of the cylinder is $L_r = \min(L_x, L_y)/2$ in radial direction and L_z in z -direction. Note that in the part of the 3D domain not covered by the sphere or the cylinder, the gravitational potential from the surrounding 1D spherically symmetric code is used.

Due to the compactness of the mass distribution involved in core-collapse, the pure Newtonian approach to gravity is too simplistic and general relativistic effects become important. Because general relativity yields stronger gravitational forces, a purely Newtonian treatment leads to slower infall velocities and reduced compactness of the nascent proto-neutron star (see [27, 98, 100]). Therefore, general relativistic effects have to be appropriately approximated for quantitative simulations of core-collapse supernova.

In our Newtonian MHD codes `FISH` and `ELEPHANT`, we approximately include general relativity by an effective gravitational potential [106] which mimics the deeper gravitational well of the relativistic case (see figure 2.28). In this approach, the Newtonian gravitational potential given by eq. (2.135) is replaced by an effective potential

$$\frac{\partial\phi}{\partial r} = \frac{G}{r^2} \left(M_{\text{eff}} + \frac{4\pi r^3}{c^2} (p + p_\nu) \right) \frac{1}{\Gamma^2} \left(\frac{\rho c^2 + \rho e + p}{\rho c^2} \right), \quad (2.137)$$

where p is the gas pressure, p_ν the neutrino pressure and e the specific internal energy. This form is theoretically motivated by the Tolman-Oppenheimer-Volkoff (TOV) solution of general relativistic hydrostatic equilibrium of spherical stars [144]. In [106] several expressions for the effective mass have been suggested and we adopted their recommended 'case A':

$$M_{\text{eff}}(r) = \int_0^r 4\pi \left(\rho + \frac{\rho e}{c^2} + \frac{E_\nu}{c^2} \right) \Gamma r^2 dr, \quad (2.138)$$

where E_ν is the neutrino energy density. The metric function Γ is given by

$$\Gamma(r) = \sqrt{1 + \frac{v_r^2}{c^2} + \frac{2GM_{\text{eff}}}{c^2 r}}, \quad (2.139)$$

where v_r is the radial velocity. Note the mutual dependence of Γ and M_{eff} , which is accounted for iteratively. The (parallel) implementation follows the above described Newtonian procedure. The effective potential additionally needs also the mapping of the radial velocity and the thermodynamic state onto the spherical symmetric domain. We note that in [118] an effective relativistic potential for (very) rapidly rotating configurations was proposed. However, in our models we have not implemented it yet and this may be postponed for future work. Furthermore, it might be interesting to integrate also the magnetic energy density in this formalism.

2.3.2 Gravity in cylindrical coordinates and axisymmetry

In the case of moderately to rapidly rotating stars, centrifugal forces may substantially deform the mass distribution so that a spherically symmetric treatment is no longer adequate. Moreover, the combined action of rotation and magnetic fields also results in substantial deviations from spherical symmetry. In this case, the mass distribution may be reasonably well approximated by an axisymmetric mass distribution. For obvious reasons, the symmetry axis is chosen to coincide with the rotational axis.

We have chosen to use (axisymmetric) cylindrical coordinates and then the Poisson equation reads

$$\frac{1}{r} \frac{\partial}{\partial r} \left(r \frac{\partial\phi}{\partial r} \right) + \frac{\partial^2\phi}{\partial z^2} = \frac{\partial^2\phi}{\partial r^2} + \frac{1}{r} \frac{\partial\phi}{\partial r} + \frac{\partial^2\phi}{\partial z^2} = 4\pi G\rho, \quad (2.140)$$

where r is the cylindrical radius and $\rho = \rho(r, z)$ the axisymmetric density distribution. The latter is obtained by a conservative mapping procedure (very similar to the spherically symmetric case) from the 3D Cartesian domain.

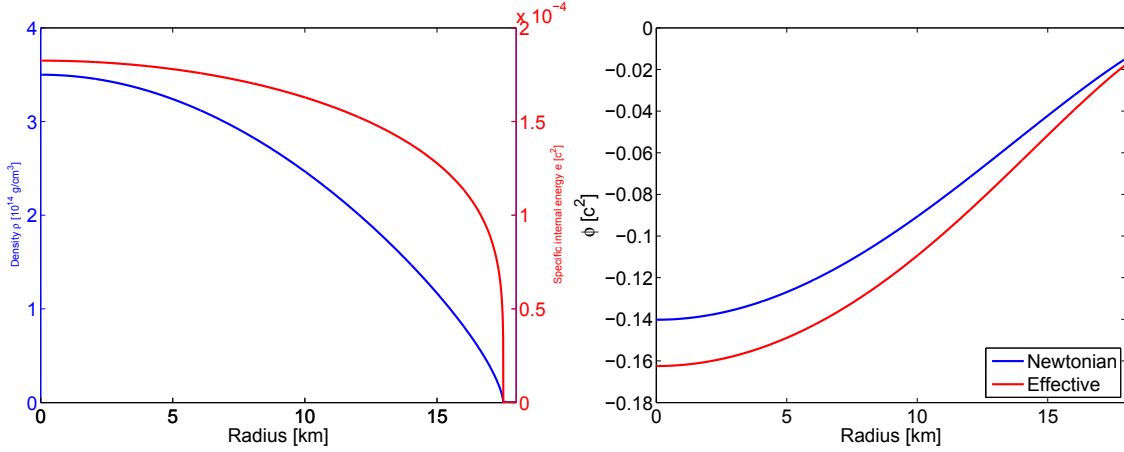


Figure 2.28: Comparison of the Newtonian and effective relativistic gravitational potential for a $\gamma = 2.5$ polytrope and polytropic constant $K = 0.01$. Left: density and specific internal energy profiles. Right: gravitational potential profiles. Note the deeper gravitational well of the effective relativistic potential mimicking the stronger attraction in the relativistic case.

The axisymmetric cylindrical domain is chosen to be the largest cylinder, fully contained in the 3D Cartesian domain, with the z axis for the symmetry axis: $r \in [0, \min(L_x, L_y)/2]$ and $z \in [-L_z/2, L_z/2]$ where L_x, L_y, L_z are the domain's lengths in the respective direction (see figure 2.27).

The axisymmetric domain, including boundary, is discretised regularly by $N_r + 2$ ($N_r = \min(N_x, N_y)/2$) and $N_z + 2$ points in the respective direction, i.e. with the same resolution as the 3D Cartesian domain:

$$r_l = \left(l - \frac{1}{2}\right) \Delta r, \quad l = 0, \dots, N_r + 1$$

$$\Delta r = \frac{\min(L_x, L_y)/2}{N_r},$$
(2.141)

and

$$z_k = \left(k - \frac{1}{2}\right) \Delta z - \frac{L_z}{2}, \quad k = 0, \dots, N_z + 1$$

$$\Delta z = \frac{L_z}{N_z}.$$
(2.142)

Note that this discretisation avoids the coordinate singularity at the symmetry axis. On the lower and upper boundary (r_l, z_k) for $l = 1, \dots, N_r$, $k = 0, N_z + 1$ the potential is obtained from the previously described spherically symmetric approach. The same condition is applied at the upper boundary in r direction (r_l, z_k) for $l = N_r + 1$, $k = 1, \dots, N_z$. Along the symmetry axis, a mirror boundary condition is applied:

$$\phi(r_0, z_k) = \phi(r_1, z_k), \quad k = 1, \dots, N_z.$$
(2.143)

The Poisson eq. (2.140) is then discretised to $O(\Delta r^2 + \Delta z^2)$ accuracy as follows

$$\frac{\phi_{l+1,k} - 2\phi_{l,k} + \phi_{l-1,k}}{\Delta r^2} + \frac{\phi_{l+1,k} - \phi_{l-1,k}}{2\Delta r r_l} + \frac{\phi_{l,k+1} - 2\phi_{l,k} + \phi_{l,k-1}}{\Delta z^2} = 4\pi G \rho_{l,k}$$
(2.144)

for $l = 2, \dots, N_r$, $k = 1, \dots, N_z$ and

$$\frac{\phi_{l+1,k} - \phi_{l,k}}{\Delta r^2} + \frac{\phi_{l+1,k} - \phi_{l,k}}{2\Delta r r_l} + \frac{\phi_{l,k+1} - 2\phi_{l,k} + \phi_{l,k+1}}{\Delta z^2} = 4\pi G \rho_{l,k} \quad (2.145)$$

for $l = 1$, $k = 1, \dots, N_z$. This linear system of $N_r \times N_z$ equations can be solved by a wide variety of methods (see [131, 137, 142] and references therein).

In the production codes, we have implemented a simple V cycle multigrid method with a variety of smoothers. This type of iterative methods can solve elliptic PDEs discretised on N grid points in $O(N)$ iterations [23, 137, 162]. Thorough theoretical and methodical descriptions of the multigrid method can be found in the cited textbooks and shall not be repeated here. The only difference of our implementation to the ones in the textbooks cited above relies in straightforward and standard adaption of the algorithm to non-square discretisations ($N_r \neq N_z$) and the usually assumed $2^n + 1$ grid points (here n is the number of grids). Non-square discretisations are handled by semi-coarsening, where only one direction is coarsened, i.e. the direction with more grid points. The $2^n + 1$ grid points requirement is 'relaxed' by coarsening from the full $N_r \times N_z$ grid to the one that is closest to $N_r/2 \times N_z/2$ and has $(2^{n_r-1} + 1) \times (2^{n_z-1} + 1)$ points, where n_r and n_z are the number of grids in the respective direction.

In a parallel distributed memory context, the mapping procedure from the 3D Cartesian domain to the 2D axisymmetric domain also requires the call to a collective communication routine (`MPI_ALL_REDUCE`) to sum up the contributions from all processes to $\rho(r, z)$. Then each process has available the axisymmetric density distribution and can solve eq. (2.140) by the multigrid method to obtain the axisymmetric gravitational potential. Again, since each process holds the axisymmetric potential for the full domain, no communication is required during this step.

Similar to the spherically symmetric case, the most expensive part in terms of wall-clock time and potential parallel scaling bottleneck for the algorithm outlined above, is the collective communication required for the construction of the axisymmetric density distribution $\rho(r, z)$. However, the overall solution procedure takes only $\sim 5\%$ of the time for a MHD step in typical production runs. The speed of this may seem surprising compared to the spherical symmetric timing, because significantly more data ($N_r \times N_z$) has to be communicated in the axisymmetric case. This may be explained by the fact that the time for the communication in the spherical case is latency dominated. Further investigations are needed to clarify this point. However, the implemented version seems to be quite efficient.

We note that the multigrid scheme has also been adapted for shared memory parallelism via OpenMP.

As outlined in the previous subsection 2.3.1, general relativity is important in the context of stellar collapse and some approximate treatment is therefore desirable. As proposed in [106], an effective relativistic potential for multi-dimensional flows $\phi(r, z)$ can be constructed by substitution of the 'spherical contribution' $\bar{\phi}(r)$ to the multi-dimensional Newtonian gravitational potential $\phi(r, z)$ by the effective potential $\bar{\phi}_{\text{eff}}(r)$:

$$\phi_{\text{eff}}(r, z) = \phi(r, z) - \bar{\phi}(r) + \bar{\phi}_{\text{eff}}(r). \quad (2.146)$$

2.4 Tracer particles

Constraints on the nature of the CCSN explosion mechanism can also come from the composition of the ejecta. Because nuclear networks with thousands of isotopes are prohibit-

ively expensive in terms of CPU time and memory for multi-dimensional computations, such networks can (currently) only be integrated in a post-processing step. This, however, neglects the feedback of the nuclear burning onto the hydrodynamics.

The post-processing calculations need as input the thermodynamic conditions (density, temperature, electron fraction, ...) of a particular fluid element advected with the flow. In order to record these quantities in our Eulerian code (where the grid is fixed in space), we introduce a Lagrangian component in the form of tracer particles that we passively advect with the flow.

In principle, the tracer particles trajectories could also be produced by post-processing the regular output of a hydrodynamical simulation. This was done e.g. in [120]. With this approach, one has to make sure that the outputs are sufficiently dense in time in order to follow "precisely" enough the particle trajectories. In our 3D simulations, we output only every 5-8th time step in order to limit the generated data amount. Further, only selected parts of the total computational domain are written with the full resolution. Because of these considerations, we opted for a direct implementation of the tracer particles (where the particles are concurrently evolved in time with hydrodynamics). The trajectories are thus computed with the full temporal and spatial resolution and accuracy.

The evolution equation for the p th passive tracer particle is then simply

$$\frac{d\mathbf{x}_p}{dt} = \mathbf{v}(\mathbf{x}_p, t), \quad (2.147)$$

where \mathbf{x}_p is the particle position and $\mathbf{v}(\mathbf{x}_p, t)$ is the velocity at the particle's position. The velocity is obtained by interpolation on the hydrodynamics grid.

The following subsections describe in detail the temporal evolution of the tracer particles, the mapping of grid quantities to the particles and the (parallel) implementation. Because there is not much original information in the following subsections, they are more meant as a documentation.

2.4.1 Time integration

Here we shall describe the used methods to integrate the ODE (2.147) in time. The particles velocities are obtained by interpolating the velocity field on the hydrodynamics grid.

The particles are advanced in time from t^n to $t^{n+1} = t^n + \Delta t^n$, where the time step is dictated by the hydrodynamics scheme. A simple first order accurate in time update of the p th particle's position is then given by Euler's method

$$\mathbf{x}_p^{n+1} = \mathbf{x}_p^n + \mathbf{v}_p^n \Delta t^n. \quad (2.148)$$

Here $\mathbf{v}_p^n = \mathbf{v}(\mathbf{x}_p, t^n)$ is the fluid velocity at the particle's position.

We have also implemented a second order accurate in time two-stage Runge-Kutta (RK2) method:

$$\begin{aligned} \mathbf{x}_p^* &= \mathbf{x}_p^n + \mathbf{v}_p^n \Delta t^n \\ \mathbf{x}_p^{**} &= \mathbf{x}_p^* + \mathbf{v}_p^* \Delta t^n \\ \mathbf{x}_p^{n+1} &= \frac{1}{2} (\mathbf{x}_p^n + \mathbf{x}_p^{**}), \end{aligned} \quad (2.149)$$

where $\mathbf{v}_p^* = \mathbf{v}(\mathbf{x}_p^*, t^{n+1})$.

For obvious accuracy reasons, the RK2 was used in all simulations. Further, note that it makes not much sense to use higher than second order methods because the current hydrodynamics scheme is second order.

2.4.2 Spatial interpolation

We demand that the interpolation of grid quantities to the particles positions is consistent with the numerical method used for the hydrodynamics. Since we are using a finite volume method, the quantities on the grid represent cell averages rather than point values

$$\bar{q}_{i,j,k}^n = \frac{1}{V_{i,j,k}} \int_{V_{i,j,k}} q(\mathbf{x}, t^n) dV, \quad (2.150)$$

where $\bar{q}_{i,j,k}^n$ is some scalar grid quantity (e.g. density) and $V_{i,j,k}$ is the volume of cell (i, j, k) . Vectors are interpolated component-wise.

A first order in space conservative interpolation is then simply obtained by

$$q_p^n = q(\mathbf{x}_p, t^n) = \bar{q}_{i,j,k}^n \quad \text{for } \mathbf{x}_p^n \in V_{i,j,k}, \quad (2.151)$$

i.e. constant interpolation.

For second order accuracy, we use a tri-linear conservative interpolation

$$\begin{aligned} q(\mathbf{x}, t^n) &= \bar{q}_{i,j,k}^n \\ &+ \left(\frac{\partial q}{\partial x} \right)_{i,j,k}^n (x - x_i) \\ &+ \left(\frac{\partial q}{\partial y} \right)_{i,j,k}^n (y - y_j) \\ &+ \left(\frac{\partial q}{\partial z} \right)_{i,j,k}^n (z - z_k) \quad \text{for } \mathbf{x}_p^n \in V_{i,j,k}, \end{aligned} \quad (2.152)$$

where we evaluated the derivatives by simple central differences of the cell averages

$$\begin{aligned} \left(\frac{\partial q}{\partial x} \right)_{i,j,k}^n &= \frac{\bar{q}_{i+1,j,k}^n - \bar{q}_{i-1,j,k}^n}{\frac{\Delta x_{i-1}}{2} + \Delta x_i + \frac{\Delta x_{i+1}}{2}} \\ \left(\frac{\partial q}{\partial y} \right)_{i,j,k}^n &= \frac{\bar{q}_{i,j+1,k}^n - \bar{q}_{i,j-1,k}^n}{\frac{\Delta y_{j-1}}{2} + \Delta y_j + \frac{\Delta y_{j+1}}{2}} \\ \left(\frac{\partial q}{\partial z} \right)_{i,j,k}^n &= \frac{\bar{q}_{i,j,k+1}^n - \bar{q}_{i,j,k-1}^n}{\frac{\Delta z_{k-1}}{2} + \Delta z_k + \frac{\Delta z_{k+1}}{2}}. \end{aligned}$$

Since our hydrodynamics scheme is currently second order, it makes no sense to implement a higher than second order spatial interpolation here. Furthermore, we also do not limit the slopes (as is done in the hydrodynamics scheme), because there are no stability issues for the tracer particles evolution.

2.4.3 Verification

We have tested the tracer particles on the isentropic vortex problem. It is a smooth 2D hydrodynamics problem with the motion of the fluid swirling around the domain's centre. Furthermore, it has an analytical solution and is therefore ideally suited for testing the tracer particles evolution in conjunction with the hydrodynamics.

We used the initial conditions in 2.1.8, domain $[-5, 5]^2$ and the same series of grids ($N^2 = 64^2, 128^2, 256^2, 512^2, 1024^2$). On this we added 2 tracer particles with the following initial positions

$$\mathbf{r}_1 = \begin{bmatrix} 0.5 \\ 0 \end{bmatrix} \quad \text{and} \quad \mathbf{r}_2 = \begin{bmatrix} 2.1 \\ 0 \end{bmatrix}. \quad (2.153)$$

The particles positions in time are then given by

$$\mathbf{r}_p(t) = r_p(t=0) \begin{bmatrix} \cos(A_p t) \\ \sin(A_p t) \end{bmatrix}, \quad (2.154)$$

where

$$A_p = \frac{\beta}{2\pi} e^{\frac{1}{2}(1-r_p(t=0)^2)} \quad (2.155)$$

with $p = 1, 2$ and $r_p = \|\mathbf{r}_p\|$.

The fluid and the particles are then evolved until $t = 10$ with a fixed time step corresponding initially to ≈ 0.75 CFL. During this time lapse, particle 1 does ~ 1.84 and particle 2 ~ 0.23 revolutions around the centre of the domain. We used the Euler and the RK2 scheme for the temporal integration, while keeping fixed the tri-linear spatial interpolation of the velocity.

The computed $L2$ error between the numerical and analytical particle positions are displayed in figure 2.29. From the figure we conclude that the tracer evolution works well and is consistent with the expected accuracy of the respective temporal integration scheme.

We note that a similar test was conducted in [24], thought for one grid resolution only.

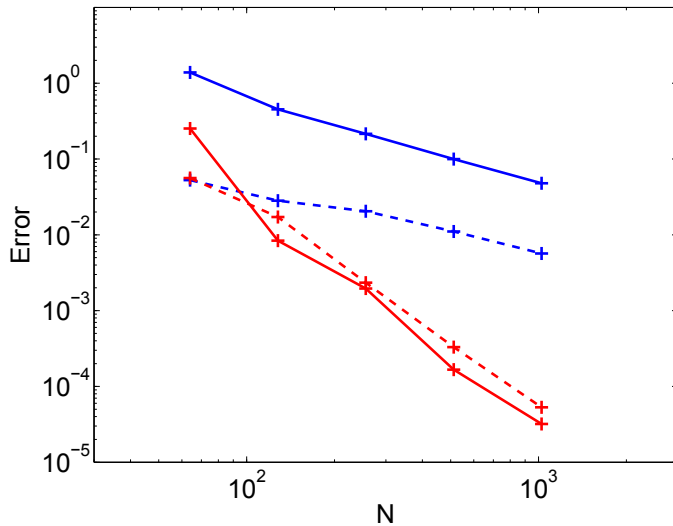


Figure 2.29: Errors for the particles 1 and 2 in the isentropic vortex test. The blue solid (dashed) line is for particle 1 (2) and Euler’s method for time integration. The red solid (dashed) line is for particle 1 (2) computed with the RK2 method. Note that the lines show the expected convergence slopes (1st for Euler and 2nd for RK2).

2.4.4 Parallel implementation

The 3D Cartesian domain (in which the particles are advected) is partitioned via cubical domain decomposition (see subsection 2.1.7). As tracers are advected with the fluid, they may leave their (initial) host process for an adjacent (in physical space) process. Hence one important step in the implementation is that of transferring (efficiently) particles from one process to another as they move. Furthermore, since the number of tracer particles on a particular process at a given time is not known in advance, the particles have to be stored in dynamically allocated storage.

As a dynamic data structure, we have opted for a so-called doubly-linked list that consists of a set of sequentially linked records. Each record contains the data for a particular particle and two links, that point to the previous and next particle record in the list [38]:

```
particle_list particle{
  id    % unique identification
  r     % position
  v     % velocity
  data  % particle properties (e.g. density, temperature, ...)
  prev  % pointer to previous particle in list
  next  % pointer to next particle in list
}
```

A leaving (the local process) particle can therefore be easily extracted out of the list. The dynamical allocatable particle storage has also the advantage, that particles can be injected at any time during a simulation (e.g. based on certain criteria like being in the ejecta of the supernova).

For the transfer of the particles, we have tested several implementations in MPI. The easiest uses collective communication routines. Each process checks for leaving particles from his (particles) list, removes them and stores them in a communication buffer. All processes then exchange their leaving particles among each other (`MPI_ALLGATHERV`). Each process can then catch the particles entered in his (local) domain and append it to his particle list. However, this implementation proved to be inefficient when a large number of particles had to be transferred each time step. This is for example the case in the CCSN simulations involving rotation of the progenitor.

A second implementation used (non-blocking) point-to-point communication between all the neighbours (in 3D there are 26!). The major limiting factor of this implementation was the communication latency, i.e. the start of a send/receive operation to a particular neighbour (especially corners) could take longer than the actual sending/receiving of the data.

The third implementation also uses point-to-point communications, but in a directionally split manner. Here particles are only transferred to neighbours along a coordinate direction, but eventually a particle is transferred more than once (see figure 2.30 for a schematic 2D explanation). This implementation has proven to be the most efficient (of the former two alternatives), i.e. in CCSN simulations (also with rotation) involving 100'000 particles uses only $\sim 2 - 3\%$ of the total CPU-time of a MHD step. The same communication algorithm is implemented in FLASH [50].

2.5 Angular momentum and magnetic field boundary conditions

Rotation and magnetic fields play an essential role in the MHD CCSN explosion mechanism. There is considerable observational evidence that rotation and magnetic fields are present in the progenitor and the compact remnant [155, 76, 43].

However, the detailed distribution of rotation and the magnetic field in the progenitor are observationally hidden so far. From the theoretical side, stellar evolution calculations have been performed including the effects of rotation and/or magnetic fields [64, 65, 69]. While including highly sophisticated treatments of rotation and magnetic fields, the stellar evolution calculations are performed in 1D spherical symmetry and might therefore

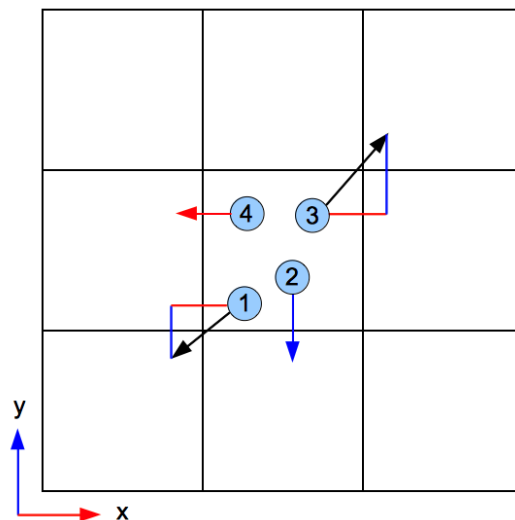


Figure 2.30: 2D illustration of the dimensionally split inter process transfer of particles. First, the particles are exchanged along the x -direction (red): particles 1,4 are transferred to the left process and 3 to the right. For particle 4, we already reached the destination process and it is therefore added to the process's particle list. Second, the particles are exchanged in y -direction (blue). Particles 1 and 3 are only transiting temporarily on the process they were sent to in x -direction and they reach only after the y -direction transfer their destination process (where they are added to the process's particle list). Particle 2 reaches directly its destination process in the y sweep.

miss the inherently multi-dimensional character of the phenomena they try to model. Recently, multi-dimensional stellar evolution calculations have started (see [6] and references therein).

With all these current limitations in mind, we have taken a parametric approach by constructing the initial distributions of rotation and/or magnetic field using analytical expressions in our simulations.

As outlined in 1.3, our simulation setup consists of a 3D Cartesian domain, evolving the central parts of the star, which is embedded in a larger 1D spherically symmetric domain, evolving the outer parts. While in the 3D domain, we can follow consistently rotation and magnetic fields, we encounter consistency problems in the spherically symmetric 1D domain. Therefore we need some approximation of the evolution of rotation and magnetic field in the spherically symmetric domain in order to get reasonably accurate boundary conditions for the 3D domain. In the following subsections, we describe this evolution in detail.

2.5.1 Evolution of rotation

Here we describe the approximate evolution of rotation in the 1D spherically symmetric domain. We assume that the rotation law is symmetric around the axis of rotation and is given in the form

$$\Omega = \Omega(r, \theta), \tag{2.156}$$

where Ω is the angular velocity as a function of radius r and polar angle θ . We have implemented several rotation laws found in the literature:

1. Solid body rotation [87]:

$$\Omega(r, \theta) = \Omega_0, \quad (2.157)$$

where Ω_0 is the constant angular velocity.

2. Shellular rotation [115]:

$$\Omega(r, \theta) = \Omega_{0,c} \frac{R_0^2}{r^2 + R_0^2}, \quad (2.158)$$

where r is the spherical radius, R_0 is a constant that controls the degree of differential rotation and $\Omega_{0,c}$ is the central angular velocity.

3. Cylindrical rotation I [45]:

$$\Omega(r, \theta) = \Omega_{0,c} \frac{X_0}{r \sin(\theta) + X_0}, \quad (2.159)$$

where X_0 is a constant that controls the degree of differential rotation (as a function of distance from the rotation axis) and $\Omega_{0,c}$ is the central angular velocity.

4. Cylindrical rotation II [45]:

$$\Omega(r, \theta) = \Omega_{0,c} \frac{X_0^2}{r^2 \sin^2(\theta) + X_0^2}, \quad (2.160)$$

where the constants have the same meaning as for the cylindrical rotation I.

5. Cylindrical rotation III [79]:

$$\Omega(r, \theta) = \Omega_{0,c} \frac{X_0^2}{r^2 \sin^2(\theta) + X_0^2} \frac{Z_0^4}{r^4 \cos^4(\theta) + Z_0^4}, \quad (2.161)$$

where $\Omega_{0,c}$, X_0 have the same meaning as for the cylindrical rotation I, II and Z_0 controls the degree of differential rotation (as a function of distance from the equatorial plane).

For the theoretical motivation of the different rotation profiles we refer to the respective references given above. See figure 2.31 for a graphical representation of the different rotation laws.

The collapse of the stellar core in the 1D spherically symmetric domain is simulated by the time-implicit hydrodynamics code **AGILE** [101] that computes radial profiles for various quantities (e.g. density, velocity, ...). The 1D collapse code does not include rotation.

At the beginning of a collapse simulation, we generate an axisymmetric 2D grid of the domain ($r \in [0, R_{\text{AGILE}}] \times (\theta \in [0, \pi])$) with N_r and N_θ cells in r - and θ -direction. Here R_{AGILE} is the maximum radial extent covered by the 1D domain initially. Cell interfaces, denoted by half-integer indices, are given by

$$\begin{aligned} r_{l+1/2}^0 &= l \Delta r_l^0, \quad l = 0, \dots, N_r \\ \theta_{m+1/2} &= m \Delta \theta, \quad m = 0, \dots, N_\theta, \end{aligned} \quad (2.162)$$

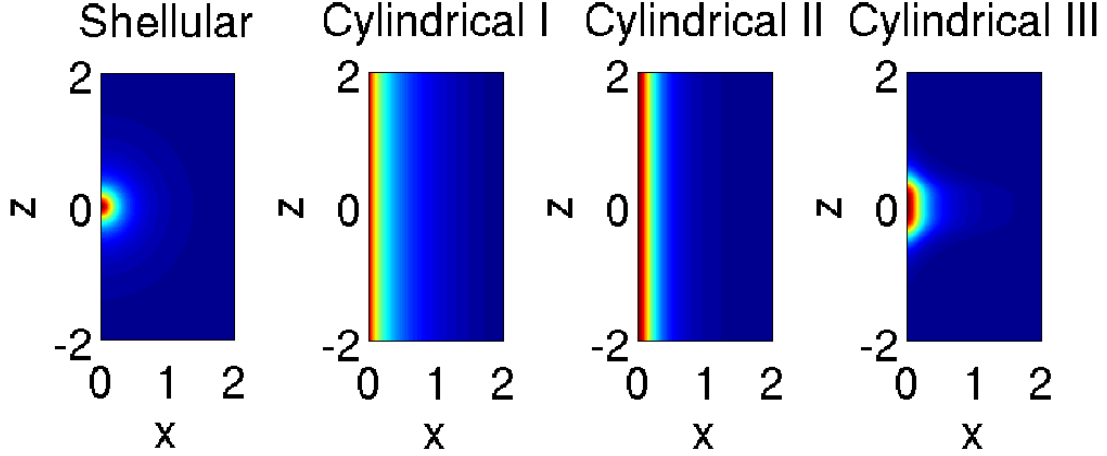


Figure 2.31: Angular velocity profiles for a domain $x \in [0, L_x]$, $z \in [-L_z/2, L_z/2]$ with $L_x = L_z = 2$: Shellular ($R_0 = 0.1L_x$), cylindrical I and II $X_0 = 0.1L_x$, cylindrical III ($X_0 = 0.1L_x$, $Z_0 = 0.1L_z$). The color scale ranges from the central angular velocity $\Omega_{0,c} = \pi$ (red) to zero (blue).

where the increments are given by

$$\begin{aligned} \Delta r_l^0 &= \frac{R_{\text{AGILE}}}{N_r} \\ \Delta \theta &= \frac{\pi}{N_\theta}. \end{aligned} \quad (2.163)$$

Cell centres, denoted by integer indices, are given by

$$\begin{aligned} r_l^0 &= \frac{1}{2} \left(r_{l-1/2}^0 + r_{l+1/2}^0 \right), \quad l = 1, \dots, N_r \\ \theta_m &= \frac{1}{2} \left(\theta_{m-1/2} + \theta_{m+1/2} \right), \quad m = 1, \dots, N_\theta. \end{aligned} \quad (2.164)$$

The superscript on the radial coordinate denotes the time step (initially $t^0 = 0$). The polar coordinate remains static in time. For each radial cell interface, we also store the respective mass coordinate given by the 1D code `AGILE` at the start of the simulation. We use this mass coordinate (a Lagrangian coordinate) to move the radial cell interfaces according to the collapse at each time step. Hence the radial coordinate of the 2D grid moves in time.

On this 2D grid we initialise the rotation profile. The rotation profile is then evolved in time by assuming that the specific angular momentum is conserved

$$\Omega(r_l^n, \theta_m) = \left(\frac{r_l^0}{r_l^n} \right)^2 \Omega(r_l^0, \theta_m). \quad (2.165)$$

The r_l^0 and r_l^n represent the initial and evolved cell centre at time step t^n of the shell's mass coordinate, respectively. Note that we also assume that the rotation profile does not evolve in θ -direction, i.e. we neglect all lateral angular momentum transport.

The 2D rotation profile is then used to set the boundary conditions for the 3D Cartesian domain. In figure 2.32 we show the total angular momentum contained in the biggest

enclosed sphere in the 3D domain as a function of enclosed mass at core bounce (crosses) together with the initial angular momentum distribution over the full (1D and 3D) domain (solid line). For the figure, we have used a $15M_{\odot}$ star from [64] with shellular rotation ($R_0 = 1000\text{km}$), cylindrical rotation II ($X_0 = 1000\text{km}$) and cylindrical rotation III ($X_0 = Z_0 = 1000\text{km}$). We note that the angular momentum in the 3D domain agrees well with what would be expected of angular momentum conservation. Furthermore, we note that the angular momentum profile in the 3D domain agrees well with the initial profile. Hence no significant angular momentum redistribution has occurred on the collapse time scale.

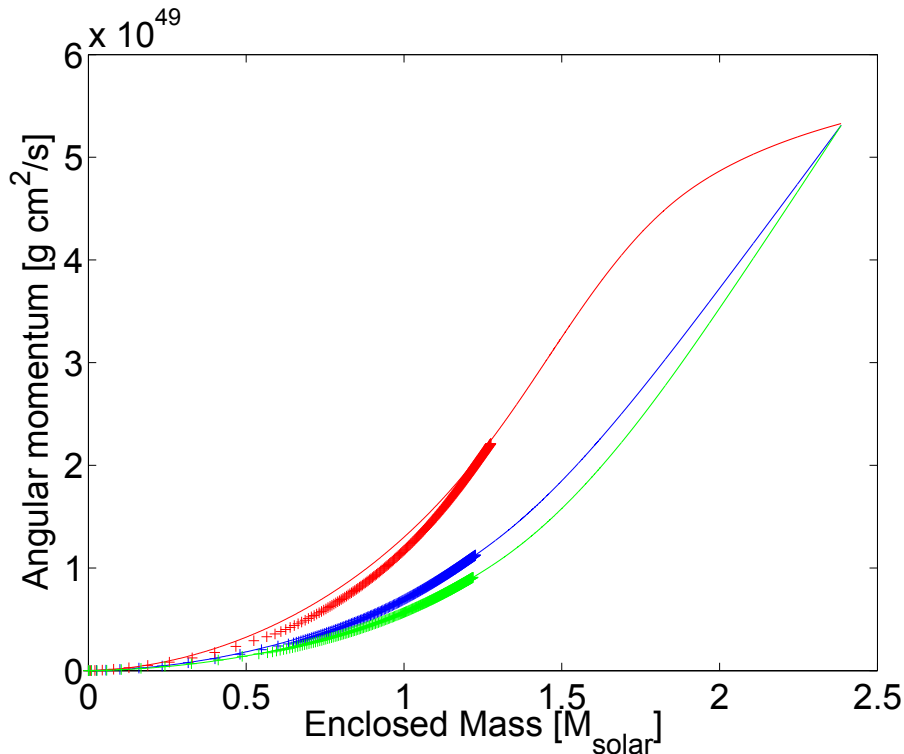


Figure 2.32: Total initial angular momentum of the collapsing core as a function of mass for shellular (solid blue), cylindrical II (solid green) and cylindrical III (solid red). Crosses represent the total angular momentum as a function of enclosed mass in the biggest enclosed sphere in the 3D Cartesian domain at core bounce. The analytical and numerical profiles agree rather well.

2.5.2 Evolution of the magnetic field

In this subsection we describe the approximate evolution of the magnetic field in the 1D spherically symmetric domain. We assume that we are given the magnetic field in the same axisymmetric 2D domain as the rotation of previous subsection:

$$\mathbf{B}(r, \theta) = B^r(r, \theta)\mathbf{e}_r + B^\phi(r, \theta)\mathbf{e}_\phi + B^\theta(r, \theta)\mathbf{e}_\theta, \quad (2.166)$$

where B^r , B^ϕ , B^θ are the components of the magnetic field and the \mathbf{e}_r , \mathbf{e}_ϕ , \mathbf{e}_θ the unit vectors in spherical coordinates.

We have currently implemented 2 magnetic field initial conditions:

1. Uniform poloidal and toroidal field:

$$\mathbf{B}(r, \theta) = B_{\text{pol}} (\cos(\theta)\mathbf{e}_r - \sin(\theta)\mathbf{e}_\theta) + B_{\text{tor}}\mathbf{e}_\phi, \quad (2.167)$$

where B_{pol} and B_{tor} are the constant poloidal and toroidal field strengths, respectively.

2. Decaying with radius poloidal and toroidal field:

$$\mathbf{B}(r, \theta) = \nabla \times \mathbf{A} + B_{\text{tor}} \frac{R_0^2}{r^2 + R_0^2} \mathbf{e}_\phi, \quad (2.168)$$

where R_0 is a constant regulating the decay and a vector potential given by

$$\mathbf{A}(r, \theta) = \left[0, \frac{B_{\text{pol}}}{2} \frac{R_0^3}{r^3 + R_0^3} r \sin(\theta), 0 \right]^T. \quad (2.169)$$

For $r < R_0$, the magnetic field strength is approximately uniform and for $r > R_0$ the magnetic field strength diminishes monotonically.

To evolve the magnetic field in the 1D spherically symmetric domain, we use the same 2D axisymmetric grid as for the rotation.

As mentioned in the previous subsection, the 2D grid moves radially in time according to the mass coordinate from the 1D code **AGILE**. In polar direction, the grid is fixed in time. In order to follow the field evolution, we use a flux conserving constrained transport algorithm. This requires a staggered placement of the magnetic field components on the 2D grid: $B_{l+1/2,m}^r$, $B_{l,m+1/2}^\phi$, $B_{l,m}^\theta$. Here, integer and half-integer indices denote cell centres and cell interfaces, respectively. For the radial and polar components, we have only to take into account the area changes between consecutive time steps:

$$B_{l+1/2,m}^{r,n} \left[2\pi(r_{l+1/2}^n)^2 \sin(\theta_m) \Delta\theta \right] = B_{l+1/2,m}^{r,n+1} \left[2\pi(r_{l+1/2}^{n+1})^2 \sin(\theta_m) \Delta\theta \right] \quad (2.170)$$

$$B_{l,m+1/2}^{\theta,n} \left[2\pi(r_l^n) \sin(\theta_{m+1/2}) \Delta r_l^n \right] = B_{l,m+1/2}^{\theta,n+1} \left[2\pi(r_l^{n+1}) \sin(\theta_{m+1/2}) \Delta r_l^{n+1} \right],$$

where the expressions in square brackets are the areas of the cell faces. This takes into account the magnetic field changes due to compression. By construction, the transport scheme also ensures the (discrete) conservation of the zero divergence of the magnetic field (if it is zero initially).

The azimuthal component does not only change by compression, but also by winding due to differential rotation. The induction equation in spherical coordinates for the ϕ -component of the magnetic field is given by

$$\frac{\partial B^\phi}{\partial t} = \frac{1}{r} \left[\frac{\partial}{\partial r} \left(r \left(v^\phi B^r - v^r B^\phi \right) \right) - \frac{\partial}{\partial \theta} \left(v^\theta B^\phi - v^\phi B^\theta \right) \right]. \quad (2.171)$$

This equation is then solved in time by simple finite differencing. The azimuthal velocity v^ϕ is obtained by interpolation in the angular velocity profile. Since we allow only radial motion, i.e. the motion given by the 1D code **AGILE**, $v^\theta = 0$ and we obtain the radial velocity by interpolation in the **AGILE** profiles.

The magnetic field on the 2D axisymmetric domain grid is used to set the boundary conditions of the 3D Cartesian domain by simple interpolation. The just described simplified

evolution of the magnetic field takes only into account the magnetic field changes induced by compression and winding. Furthermore, the magnetic field has no influence on the 1D spherically symmetric domain simulated by **AGILE**. This is justified by the reasonable assumption that the magnetic field is not dominating the dynamics in the outer layers of the star.

We note also that the scheme described here does not guarantee that the magnetic field boundary setup is exactly divergence free. The divergence error is of the order of the truncation error made in interpolating from the 2D axisymmetric grid to the 3D Cartesian domain. However, since the flow is expected to be smooth in the outer layers of the star and in the 3D boundary domain, the truncation errors remain small.

2.6 Electron neutrino leakage scheme in 3D

The inclusion of neutrino physics is an essential ingredient of CCSN simulations. An overwhelming fraction ($\sim 99\%$) of the by the collapse liberated gravitational binding energy is converted into neutrinos of all flavours. Neutrino losses make the shock stall in the early phase after bounce. On a longer time scale hot neutrinos from the innermost regions of the forming neutron star are thought to deposit some of their energy in the region behind the shock, thereby initiating the supernova explosion. This is the so-called delayed neutrino-driven explosion mechanism. Furthermore, the neutrinos also influence the matter composition, making the regions below the shock very neutron rich. Some of this neutron rich matter is expelled in the explosion and thereby setting the stage for the synthesis of the heavy elements and the implied galactic chemical evolution. Especially the MHD CCSN mechanism is believed to be a promising site for r-process nucleosynthesis in the early chemical evolution of the universe.

To date, the most micro-physically complete study of MHD CCSN explosion mechanism was performed by Burrows et al. [30]. They present 2D axisymmetric simulations in Newtonian gravity employing a progenitor from stellar evolution calculations [65] and the microphysical equation of state (EoS) of Lattimer and Swesty (LS) [86]. The neutrino transport is approximated by multi-group flux limited diffusion (MGFLD). According to their findings, the neutrino heating effect is subdominant in the computed models. Neutrinos only contribute $\sim 10\text{-}25\%$ to the final explosion energy.

While neutrino heating may so be neglected as a first approximation, the neutrino cooling cannot. Neutrino cooling is responsible for the shock stall and for the neutronisation of the matter below the shock, which is so crucial for the nucleosynthesis yields.

In order to capture (approximately) the most important neutrino cooling effects, we have coupled a sophisticated spectral leakage scheme for electron neutrinos and anti-neutrinos to our 3D MHD code. The spectral leakage scheme was developed by A. Perego. The accuracy of the scheme was verified in 1D spherical symmetry by comparison against state-of-the-art simulations of CCSN with Boltzmann neutrino transport [97]. Excellent agreement was obtained for both pre- and postbounce (~ 100 ms) phases (A. Perego, private communication). Later on, neutrino heating effects and also cooling by μ and τ neutrino flavours become important. While a leakage scheme for μ and τ neutrinos is available in 1D (also developed by A. Perego), we have not included it into our 3D code so far. However, this is planned in future upgrades.

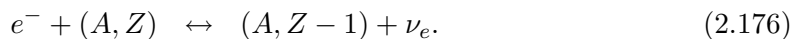
The idea of a leakage scheme is to accurately estimate the effects of neutrino cooling with high computational efficiency. Deep inside the forming neutron star, the neutrinos and the fluid are tightly coupled (nearly in equilibrium), i.e. they are trapped. On their way

out of the high density regions, neutrinos go from a (nearly) isotropic diffuse regime to the uncoupled (with matter) free streaming regime. Where the neutrinos are trapped in matter, they evolve in a hydrodynamic manner and slowly drain by diffusion. The fluid advects a neutrino particle number fraction Y_ν and an associated specific energy Z_ν according to advection equations

$$\frac{\partial \rho Y_\nu}{\partial t} + \nabla \cdot (\mathbf{v} \rho Y_\nu) = (\rho \dot{Y}_\nu) \quad (2.172)$$

$$\frac{\partial (\rho Z_\nu)^{3/4}}{\partial t} + \nabla \cdot (\mathbf{v} (\rho Z_\nu)^{3/4}) = (\rho \dot{Z}_\nu)^{3/4}, \quad (2.173)$$

where ν denotes ν_e and $\bar{\nu}_e$. The right hand side of the equations represent local source (particle/energy creation) or sink (particle/energy absorption or drain out) of trapped neutrinos. For the exact definition and the motivation of these equations we refer to [127, 102]. These source terms are estimated on the basis of local production and diffusion rates and the associated time scales. In regions where neutrinos stream freely, the created neutrinos simply escape and $Y_\nu \sim Z_\nu \sim 0$. The production rates depend only on the local thermodynamic state of matter and the locally present trapped neutrino fractions (blocking effects). On the other hand, the diffusion rates depend simultaneously on local and global quantities. The local quantity is the mean free path (of neutrino propagation) and the global quantity is the optical depth. In the intermediate semi-transparent regime, between diffusion and free streaming, an effective emission rate is computed by a smoothed minimum between production and diffusion rates. The leakage scheme also provides the source terms which enter in the equation of (magneto-) hydrodynamics: an electron fraction, an energy and a momentum (due to neutrino radiation stress) change rates. For the exact details of the leakage scheme we refer to [127] and references therein. Currently, the leakage scheme incorporates only neutral and charged weak interaction processes that are expected to play a dominant role. For the neutrino absorption and emission, the following charged current reactions are included:



Here (A, Z) denotes a nuclei with mass number A and charge Z . For the neutrino scattering, the following neutral and charged current reactions are included:



Here N denotes a free neutron or proton and ν denotes an electron neutrino or anti-neutrino. As already stated, only the reactions expected to have a predominant role are included in the current version of the leakage scheme. For a complete list of reactions and their discussion in the CCSN context we refer to [26, 108] and references therein. Note that the considered reactions are highly energy dependent on the neutrino energy [26] and therefore a spectral treatment is adopted in the leakage scheme. The scheme avoids the usage of mean energies for the determination of neutrino source functions or opacities. In the following, we describe the multi-dimensional implementation of the leakage scheme. The only quantities that do not readily translate to more than one dimension is the non-local optical depth and the neutrino stress. Since we are here primarily interested in

the simulation of MHD CCSN, involving a large degree of rotation, we shall reduce the dimensionality by exploiting the (approximate) symmetry around the rotational axis (as we already did for the gravitational potential in section 2.3).

Therefore we perform a mapping of the 3D Cartesian domain onto an axisymmetric polar grid, encompassing the biggest enclosed sphere in the 3D domain, by averaging the relevant quantities. The polar grid has then a series of radial grids along each discrete polar angle: a so-called ray. The optical depth is then calculated along each ray. Note that this is performed in a spectral manner: for each energy bin separately. Also the neutrino stresses are evaluated along the rays based on the recipe given in [96]. For the application of the leakage scheme in 3D, we then simply interpolate to the respective position the optical depth and the neutrino stress. Then the scheme can be applied, giving all the change rates for the hydrodynamic quantities. Therefore, the scheme is full 3D, apart from the computation of the optical depth and the acceleration due to neutrino stresses.

2.6.1 Verification of the implementation

In this subsection, we verify the 3D implementation of the leakage scheme. We compare a 3D simulation to a state-of-the-art 1D spherically symmetric general relativistic simulation performed with AGILE-BOLTZTRAN [97].

For the comparison, we use a solar-metallicity $15M_{\odot}$ star from [64]. The reference simulation was kindly performed by A. Perego. The 1D simulations used 103 adaptive spatial zones ranging from the centre of the progenitor star to about 7000 km. A constant-pressure boundary condition was used at the barely moving surface. The neutrino energy was resolved with 20 geometrically increasing energy groups, the first centred at 3 MeV and the last at 300 MeV. The propagation angle has been discretised with six angles suitable for Gaussian quadrature. The nuclear and weak interaction physics input is the same as in [100].

The multi-dimensional simulation consists of a inner 3D Cartesian domain of size 600^3 km³ discretised uniformly by 600^3 cells, i.e. the constant resolution is 1 km. No rotation and magnetic fields were set up. In the 3D leakage scheme, the neutrino energy was resolved with 12 geometrically increasing energy groups, the first centred at 3 MeV and the last at 200 MeV. For the computation of the optical depth, we have used a polar grid with uniform 1 km radial spacing and 30 uniform angular rays covering the full $[0, \pi]$. Like the 1D simulation, we used the LS EoS with incompressibility modulus $K = 180$. We have used the effective potential to mimic general relativistic effects 2.3.

We note that the neutrino reactions used in the 1D reference simulation are much more complete (see [100] for a complete list). We have found empirically, that the additional neutrino physics may be mimicked by simply switching off the acceleration due to neutrino stresses in the 3D simulation. This results in a reduced expansion of the shock and a shock stall at smaller radii, which is beneficial for the limited radial extent (~ 300 km) of the 3D domain. Therefore we neglect neutrino stresses in the 3D domain in the following comparison.

Figures 2.33, 2.34, 2.35, show the 3D simulation (spherically averaged) profiles (blue) together with the reference 1D simulation profiles (red) at time -1, 0, 2, 5, 10 and 50 ms with respect to bounce, respectively.

Figure 2.33 compares the 3D (spherically averaged) profiles (solid blue) with the reference 1D solution (solid red) for selected quantities a time slices -1 ms (left) and 0 ms (right) with respect to bounce. We notice the the reference solution depletonises a bit more, i.e. the electron fraction Y_e is somewhat overestimated in the 3D simulation. Beside Y_e , all

other quantities match very well. Also the sock positions are nearly identical 1 ms after bounce.

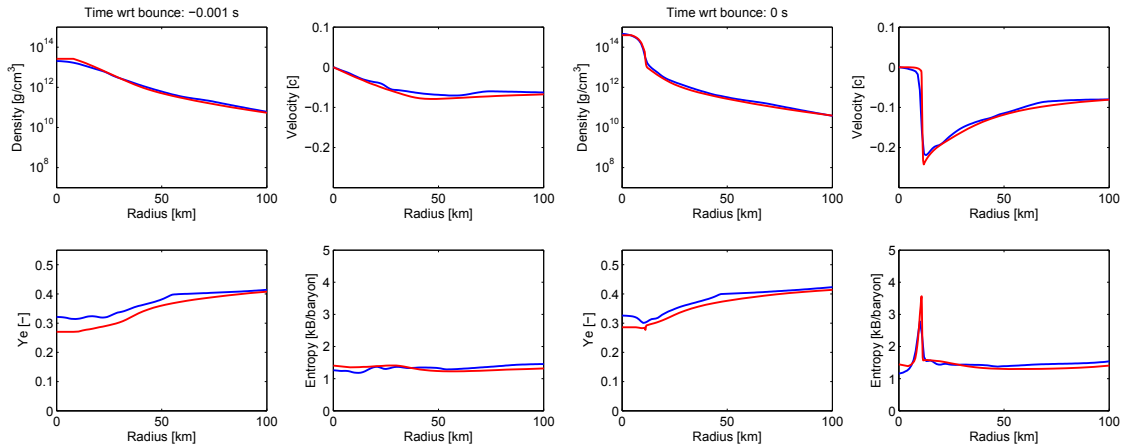


Figure 2.33: Density, velocity, electron fraction and entropy as functions of radius from a simulation with the 3D leakage (solid blue line) and a reference simulation based on Boltzmann neutrino transport (solid red line). The comparison is shown at two different time instances: at 1 ms (left) before core bounce and at bounce (right). Significant differences are only visible in the electron fraction profiles: the deleptonisation during collapse is slightly underestimated in the leakage simulation.

Figure 2.34 compares the profiles at time 2 ms (left) and 5 ms (right) postbounce. At 2 ms, we observe that the shock in the reference solution propagated ~ 10 km further in radius as in the 3D leakage simulation. The reference solution also started the neutrino burst (dip in Y_e) and these emitted neutrinos lead to some neutrino absorption ahead of the shock (manifest in the small peak at ~ 50 km). In the 5 ms postbounce time slice, on the other hand, in the 5 ms time slice, the shock position in the 3D profiles is ~ 10 km ahead of the reference solution. The neutrino burst has also started to deleptonise the 3D solution, however, somewhat less than in the reference solution. This lower energy loss may explain the faster shock propagation.

In figure 2.35, profiles at 20 ms (left) and 50 ms (right) are shown. At 20 ms, the 3D leakage has caught up with the postshock deleptonisation, i.e. the Y_e profile nearly matches the reference solution. The 3D solution shock is still ~ 10 km ahead of the shock in the reference solution. The 50 ms time slice shows that the leakage somehow overestimates the neutrino cooling. Hence the lower electron fraction profile. Furthermore, the postshock region (~ 50 -100 km) is cooler (lower entropy) in the 3D solution than in the reference solution due to the overestimated cooling. This also causes the difference in the shock location of ~ 10 km.

Figure 2.36 gives a short overview of the comparison in the form of shock trajectories and neutrino luminosities for the approximate 3D leakage simulation (blue) and the reference 1D Boltzmann neutrino transport simulation (red). The left panel shows the shock trajectories. As stated before, the very early postbounce phase ($\lesssim 3 - 4$ ms) shows nice agreement in the shock position. At later times, the shock radius in the 3D leakage simulation is first overestimated by ~ 10 km ($\sim 5 - 35$ ms), followed by an underestimation by $\lesssim 30$ km and an overestimation again by ~ 30 km (40-200 ms). The right panel shows the neutrino luminosities measured at 300 km for electron neutrinos (solid lines) and anti-

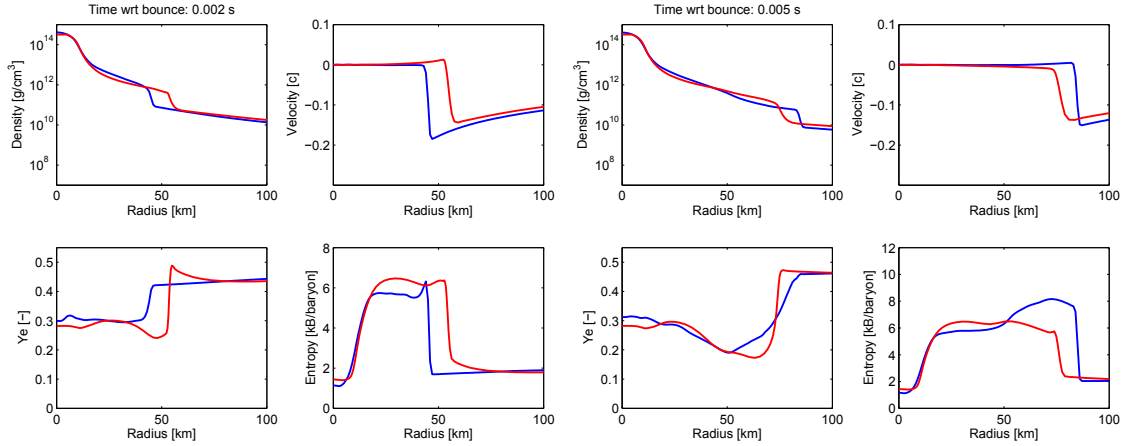


Figure 2.34: Same presentation as in figure 2.33. Here the comparison is shown at two later time instances: at 2 ms (left) after bounce and 5 ms (right) after bounce. The 3D leakage simulation underestimates the shock position at 2 ms, and overestimates it a bit at 5 ms after bounce. The neutrino burst deleptonisation is also somewhat delayed in the approximate 3D simulation.

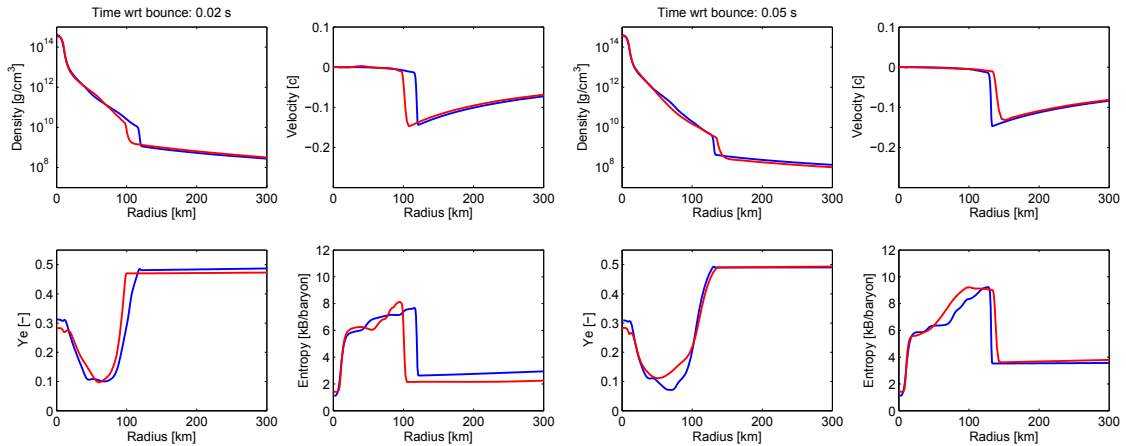


Figure 2.35: Same presentation as in figure 2.33. Here the comparison is shown at two later time instances: at 20 ms (left) after bounce and 50 ms (right) after bounce. In the 20 ms time slice, the profiles agree rather well. At 50 ms, the leakage overestimates the cooling by neutrino emission and this results in a lower electron fraction profile.

neutrinos (dashed lines). In the reference solution (red), the luminosities are measured in the comoving frame. In the 3D leakage (blue), we have also corrected for the redshift. We observe that in the collapse phase the approximate 3D simulation underestimates the luminosity. Therefore the deleptonisation is less pronounced and this is consistent with the observation (in figure 2.33) that the Y_e profile is a bit higher. The peak luminosity (in electron neutrinos) is also overestimated by $\sim 15\%$. Later on, the luminosity is overestimated until ~ 70 ms. This increased energy loss in the 3D solution may explain the rapid slow down of the shock propagation. It also explains the lower Y_e profile in the left panel of figure 2.35. At times $\gtrsim 80$ ms, the luminosity of the electron neutrinos agree more or less. We note that also the electron anti-neutrino luminosity is nicely reproduced, though

that it is somewhat lower in the 3D leakage simulation for times $\gtrsim 40$ ms.

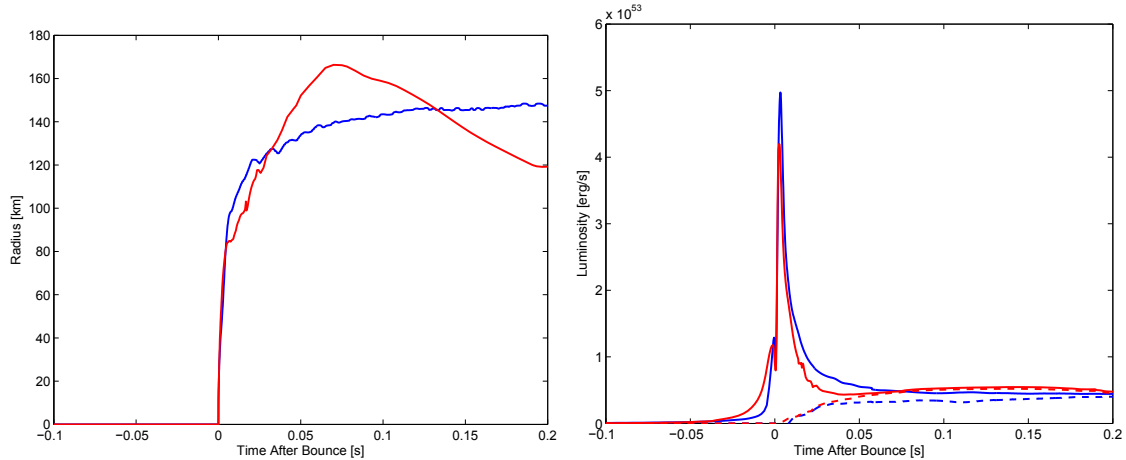


Figure 2.36: The left panel shows the shock position as a function of time for the 3D leakage simulation (solid blue) and the reference Boltzmann solution (solid red). The right panel shows the electron neutrino (solid line) and anti-neutrino (dashed line) luminosities as a function of time with same colour convention as the left panel.

In summary, we believe that we have complemented our 3D MHD CCSN model with (dominant) neutrino physics in the form of a 3D spectral leakage scheme. We have confirmed the ability of the scheme to (qualitatively) reproduce the effects of neutrino cooling: deleptonisation during collapse, neutrino trapping, neutronisation burst and the postbounce deleptonisation. The scheme gives also access to observable in the form of neutrino luminosities. While the magnitude of the signal may show some deviations, we believe that characteristic features from multidimensional effects may well be extracted. Furthermore, even that the electron fraction can be underestimated, we think that it still can be used as input for detailed nucleosynthetic analysis. The 3D leakage scheme offers a computationally efficient approach to the modelling of CCSN in multi-dimension. These simulations may serve as a first filter to identify interesting effects which can then be studied more in depth by more refined multidimensional neutrino transport approximation like the isotropic diffusion source approximation (IDSA) [102].

As already stressed, the spectral leakage scheme currently includes only reactions thought to play a dominant role. During the collapse phase, we are missing inelastic electron-neutrino electron scattering, which thermalises the neutrinos very effectively [26]. This leads to enhanced neutrino losses, because the neutrino mean free paths vary inversely with the square of the neutrino energy. This may partly explain our higher central value of Y_e in the 3D leakage simulation when compared to the Boltzmann reference. Furthermore, the cooling by μ and τ neutrinos and anti-neutrinos has so far been neglected. The inclusion of these effects will be addressed in subsequent work.

Chapter 3

Simulation of Magneto-Rotational Core-Collapse

3.1 Introduction

Shortly after the discovery of pulsars, it was reasonable to explore the influence of rotation and magnetic fields (associated with pulsars) on the CCSN explosion mechanism [19, 87, 110, 124, 151]. These pioneering studies came to the conclusion, that the typical pulsar dipole fields of $\sim 10^{12}$ G and rotation periods of several to several tens of milliseconds could not produce strong and robust magneto-rotationally induced explosions and seemed thus unlikely.

However, several factors led to a need to reconsider this conclusion. There is growing observational evidence that CCSN are asymmetric and are substantially directed along a single direction in space [167, 168, 169]. Observation also suggest, that it is the explosion mechanism itself that is responsible for this asymmetry: the asymmetry rises as a function of time as the ejecta expand and one looks more deeply into the core material. But most importantly, the magneto-rotational CCSN (MHD-CCSN) explosion mechanism gained again in weight with the discovery and the interpretation of anomalous X-ray pulsars and soft gamma-ray repeaters as magnetars: strongly magnetised neutron stars with (dipolar) magnetic field strengths of $\sim 10^{15}$ G [44, 80, 157]. Indeed, while modern multi-dimensional models of the explosion of CCSN are very asymmetrical (due to multi-dimensional fluid instabilities), MHD-CCSN models are fundamentally so.

In the MHD-CCSN explosion mechanism, the explosion is powered by the free energy stored in differential rotation. The typical rotational kinetic energy of a proto-neutron star (PNS) may be estimated to

$$T_{\text{rot}} = \frac{1}{2} I_{\text{PNS}} \Omega_{\text{PNS}}^2 \approx 1 \times 10^{51} \text{ erg} \times \left(\frac{M_{\text{PNS}}}{1.5 M_{\odot}} \right) \left(\frac{P_{\text{PNS}}}{2 \text{ ms}} \right)^{-2} \left(\frac{R_{\text{PNS}}}{10 \text{ km}} \right)^2, \quad (3.1)$$

where M_{PNS} is the mass, R_{PNS} the radius, P_{PNS} the period, Ω_{PNS} the angular velocity and I_{PNS} the moment of inertia of the PNS. The amount of free energy in differential rotation is typically a fraction of the rotational kinetic energy. Hence, for enough rapid rotation combined with an efficient way of extracting this free energy in differential rotation robust explosions can in principle be obtained. The efficient extraction mechanism is provided by the magnetic field, which may be sufficiently amplified and result in a strong magnetic stress blowing off the matter in the vicinity of the PNS thereby driving an explosion.

From the above estimate, it becomes clear that a viable MHD-CCSN model requires rapid rotation, which the currently stellar evolution models including magnetic fields do not have [65]. In these models, the phenomenologically included magnetic fields significantly slow down the core’s rotation making it inadequate for powering an explosion. However, can we take these one-dimensional stellar evolution calculations as granted? Or does there still exist the possibility to produce supernova progenitors with fast rotation, but that only a smaller subset of massive stars take this evolutionary path? The low-metallicity models of Woosley & Heger [176], some of which they suggest as GRB progenitors, have much faster rotation rates. Moreover, Woosley & Heger suggest that these progenitors may represent only a fraction, perhaps 1%, of all the massive stars. Hence MHD driven explosions are still possible, but it might be that not all CCSN explode by this mechanism. This is also in accord with the suggestion that MHD-CCSN explosions present a promising site for r-process nucleosynthesis [110, 112, 147]. The large scatter observed in the r-process element abundances at low metallicities suggests that only a small subset of events have produced that pattern.

The classical way of magnetic field amplification in a differential rotating environment is magnetic winding [171, 172]. However, the magnetic field grows only linearly in time by field winding. If the initial field is low, the amplification process may have to last for a long time to reach a dynamical importance and by then the explosion may already have been initiated by another mechanism (e.g. delayed neutrino heating) or a black hole may have formed. An amplification process which can amplify the magnetic field exponentially in time was introduced into supernova theory by Akiyama et al. [1]: the so-called magneto-rotational instability (MRI) [12, 11, 128]. The MRI is driven by the negative angular velocity gradients which are unavoidable in the context of CCSN [125] and has the capability to amplify the magnetic field to dynamical importance. The growth of the magnetic field is exponential in time with a characteristic timescale of the rotational period and this whatever the strength of initial seed field.

The possibility to amplify the magnetic field sufficiently rapidly (by the MRI or, eventually by some other dynamo process) together with the discovery of magnetars relaunched the interest in the MHD-CCSN explosion mechanism [4, 3, 2, 30, 79, 82, 114, 145, 153, 154, 181, 122, 34]. However, only few of MHD-CCSN numerical investigations have been performed in a three-dimensional setting [114, 140]. Furthermore, these studies have been performed with simplified input physics employing a gamma-law gas and no neutrino transport.

In the present chapter, we will add up all the components described in the previous chapter and apply them to the simulation of MHD-CCSN. In section 3.2, we describe our simulation setup, initial conditions and model parameters. We also discuss some of the model’s merits and drawbacks. Section 3.3 is then devoted to the discussion of the simulations outcome, including the magnetic field amplification mechanism, the formation and propagation of the bipolar outflow and the explosion energy, ejected mass and its composition.

3.2 Initial setup and model parameters

We performed the calculations presented here with the computational setup as described in 1.3. The implementation details are described in chapter 2. The central 3D Cartesian domain spans 600^3 km^3 and is uniformly discretised by 600^3 cells, resulting in a resolution of 1 km. The magnetic fluid is evolved with the ideal MHD code `FISH`. The gravitational potential is approximated from an effective axisymmetric mass distribution that includes radial general relativistic (GR) monopole corrections (see 2.3 and [106]). For the EoS we

have used the Lattimer & Swesty EoS [86] with nuclear compressibility 180 MeV. The transport of the electron and anti-electron neutrinos is approximated by a 3D spectral leakage scheme based on a microphysical and energy dependent axisymmetric ray-by-ray approximation of the optical depth (see 2.6). The neutrino energy was discretised with 12 geometrically increasing energy groups spanning the range $E_\nu = 3 - 200$ MeV. For the computation of the optical depth, we have used a polar grid encompassing the full 3D Cartesian domain discretised uniformly with 1 km radial spacing and 30 uniformly spaced angular rays covering the full $[0, \pi]$ realm. Thus, we can only follow neutrino cooling effects. However, the up to now microphysically most complete 2D axisymmetric study of MHD-CCSN with multigroup flux-limited diffusion neutrino transport performed by Burrows et al. [30] have shown, that neutrino heating contributes only 10 – 25% to the explosion energy and is therefore subdominant. This justifies our pragmatic approach at first.

The progenitor employed for the simulations presented here is the rotating $15M_\odot$ model of Heger et al. [64] (s15.0). We have computed five models with varying analytical rotation laws (see 2.5.1). The detailed parameters for the setup of rotation is shown in table 3.1. All models have, however, the same initial amount of angular momentum. Only the spatial distribution of angular momentum and the with it associated degree of differential rotation is varied. In figure 3.1, we show the angular momentum distribution and the with it associated ratio of rotational kinetic energy to gravitational binding energy. As one can see, the solidly rotating model A has the lowest energy and the differentially rotating models have roughly a decade more rotational energy. This illustrates the evident fact that solid-body rotation is the lowest energy state. This energy excess in differential rotation can be tapped by the magnetic field as will be illustrated in the following.

For the magnetic field, we have assumed a homogeneous distribution of purely poloidal field throughout the computational domain of strength 5×10^{12} G. The parameters for the magnetic setup are summarised in table 3.2.

Note that model A is non-rotating, non-magnetic and serves as a reference for identifying effects from rotation and the magnetic field (this is the model used in the verification of the leakage scheme in 2.6).

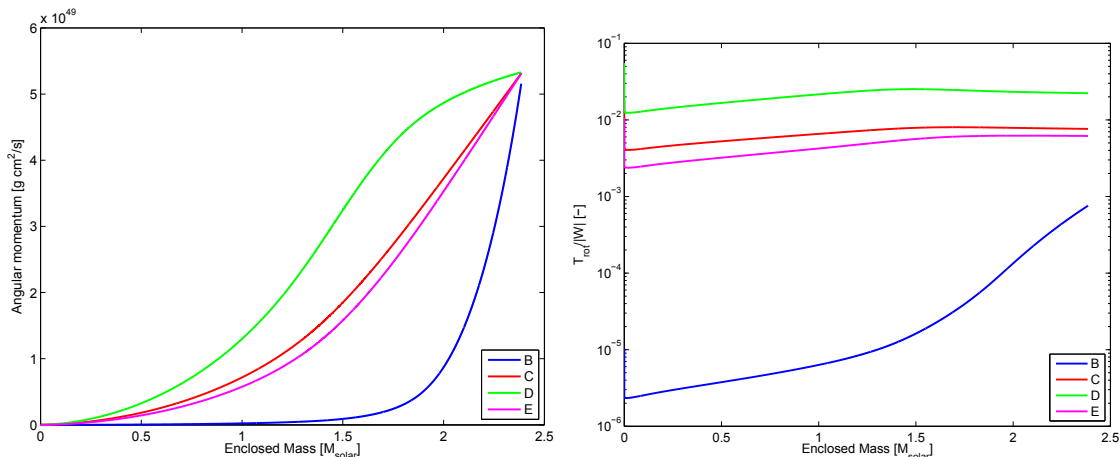


Figure 3.1: Initial angular momentum distribution (left) and ratio of rotational kinetic energy to gravitational binding energy (right) for all rotating models $T_{\text{rot}}/|W|$.

Given our parameters, a few comments are in order. We note that Heger et al. have

Model	Rot. type	R_0 [km]	X_0 [km]	Z_0 [km]	$\Omega_{0,c}$	P_0 [s]	$T_{\text{rot}}/ W $
A	-	-	-	-	0	∞	0
B	solid	-	-	-	0.074	84.91	7.58×10^{-4}
C	shellular	1000	-	-	π	2	7.63×10^{-3}
D	cylindrical III	-	1000	1000	5.47	1.15	2.23×10^{-2}
E	cylindrical II	-	1000	-	2.40	2.62	6.17×10^{-3}

Table 3.1: Parameters of the initial rotation for all computed models: the rotational law and the with it associated differential rotation parameters (R_0, X_0, Z_0), the initial angular velocity $\Omega_{0,c}$, the initial period P_0 and the initial ratio of rotational kinetic energy to gravitational binding energy $T_{\text{rot}}/|W|$.

Model	Mag. type	B_{pol} [G]	B_{tor} [G]	$T_{\text{mag}}/ W $
A	-	0	0	0
B	uniform	5×10^{12}	0	2.63×10^{-8}
C	uniform	5×10^{12}	0	2.63×10^{-8}
D	uniform	5×10^{12}	0	2.63×10^{-8}
E	uniform	5×10^{12}	0	2.63×10^{-8}

Table 3.2: Parameters of the initial magnetic fields for all computed models: the magnetic field type, the poloidal field strength B_{pol} , the toroidal field strength B_{tor} and the ratio of magnetic energy to gravitational binding energy $T_{\text{mag}}/|W|$.

also computed a series of models including magnetic fields [65]. The magnetic version of the employed progenitor in the present study is m15b2. The iron core structure of this progenitor is very similar to the one used here. However, these magnetic models experience a significant magnetic spin-down during stellar evolution and generally result in slowly rotating iron cores with central periods of $\sim 30 - 50$ s. The resulting rotational kinetic energies at bounce are consequently inadequate to power a supernova explosion. The models also predict toroidal field strengths of only few $\sim 10^9$ G and roughly three decades smaller poloidal field strengths. Moreover, their models have also the merit to produce neutron stars with rotational velocities at birth in the upper range values given by observation (periods of $\sim 10 - 15$ ms). On the other hand, stellar evolution calculations not including magnetic fields, i.e. ignoring magnetic torques, give rotational velocities which are in agreement with the values used here [64, 69].

The above said, how do we explain or justify the seemingly unrealistic initial rotation rates and magnetic fields we adopt here? The usual argument found in the literature, underlines the fact that current state-of-the-art stellar evolution models are computed in 1D spherical symmetry employing ("only" theoretically) well-motivated prescriptions for rotation and magnetic fields. So how well do these manifestly dimensionally restrained calculations model the inherently multidimensional character of rotation and magnetic fields? Can we "trust" the rotation and magnetic field distributions from these models? These questions are of course difficult to answer definitively and can ultimately only be resolved once multidimensional stellar evolution models become available.

The line of argument in the preceding paragraph, however, does not acknowledge all the merits of these stellar evolution calculations and may therefore be too simplistic [105]. More conservatively, one can suppose that there might be a subset of supernova progenitors that feature rapid rotation and (strong) magnetic fields. For example, the low-metallicity

models of Woosley & Heger [176], some of which they suggest as GRB progenitors, have much faster spinning cores at collapse even when magnetic fields are included in the evolution calculations. The total angular momentum of the iron core at the onset of collapse derived there is comparable to the one used here. Moreover, they speculate that roughly 1% of all stars above $10M_{\odot}$ might have the here desired properties.

The MHD-CCSN explosion mechanism has been suggested to be a promising site for r-process nucleosynthesis acting already in the early galaxy. This rarity of progenitors with these special conditions is also consistent with the observed scatter of r-process elements abundances at low metallicity indicating that these elements have been produced in relatively scarce events [147]. Therefore, the (eventually rare) progenitor configurations used here could provide an r-process site in agreement with observations of the early galaxy and this possibility is explored on the basis of the models computed here by C. Winteler [174].

However, another few comments are in order concerning our initial very strong magnetic field strength. Currently, the aim to perform global 3D numerical simulations of CCSN and the aim to simulate the local flow instabilities leading to magnetic field amplification (e.g. MRI, dynamo, ...) seem mutually excluding objectives [123]. Given this difficulty, we shall follow here the common approach in the literature by taking sufficiently strong initial magnetic fields. By doing so, it is hypothesised that there is a physical process that can sufficiently quickly amplify the magnetic field to dynamic importance by extracting the free rotational energy in differential rotation. Furthermore, it is assumed that the resulting MHD jet structure has lost the memory of the exact initial distribution of the magnetic fields. This motivates our choice of initial poloidal field strength, which by flux compression and rotational winding leads to magnetic fields whose magnitudes roughly agree with those expected from the physical amplification process. This physical process may be the MRI and/or some other dynamo process. The estimates given in [1, 30] show, that for the MRI and the here used rotational velocities a field strength of several 10^{15} G can be achieved within 100-200 ms with a weak dependence on the initial magnetic field.

3.3 Numerical results

3.3.1 Global dynamics

All the computed models undergo gravitational collapse and experience core-bounce due to the stiffening of the EoS above nuclear densities ($\rho_{\text{nu}} \approx 2 \times 10^{14}$ g/cm³). Several physical properties are listed in table 3.3. No model undergoes bounce dominated by centrifugal forces nor magnetic pressure.

Model	$\rho_{\text{max}}/10^{14}$ [g/cm ³]	$T_{\text{rot}}/ W $	$T_{\text{mag}}/ W $
A	4.57	0	0
B	4.56	9.86×10^{-5}	2.21×10^{-4}
C	4.15	6.81×10^{-2}	3.02×10^{-4}
D	3.31	1.46×10^{-1}	3.13×10^{-4}
E	4.34	4.68×10^{-2}	2.18×10^{-4}

Table 3.3: Bounce characteristics for all computed models: the maximum density ρ_{max} , the ratio of rotational kinetic energy to gravitational binding energy $T_{\text{rot}}/|W|$ and ratio of magnetic energy to gravitational binding energy $T_{\text{mag}}/|W|$.

All rotating models have the same initial total angular momentum, but with differing spatial distributions (see figure 3.1). The distribution then determines how much total angular momentum is present in the interior of the core that collapses nearly homologously $v \propto r$ (the so-called inner core), which then sets the relative importance of centrifugal forces at bounce. The relative importance of centrifugal forces is then directly reflected in the maximum density at bounce. The solidly rotating model B bounces at the same maximum density as the non-rotating model A. The angular momentum distribution in model C and E is very similar. This explains that both models bounce at similar ρ_{\max} with slightly higher density for model B, which is consistent with the initial angular momentum distribution (see figure 3.1). The inner core of model D possesses significantly more angular momentum and therefore bounces at lower ρ_{\max} than all other models. But note that the maximal density of model D is still above nuclear saturation density and therefore this is not a centrifugal bounce per definition. The same trend is also reflected in the ratio of rotational kinetic energy T_{rot} to gravitational binding energy $|W|$ as can be seen in table 3.3.

In figure 3.2, we show the evolution of the maximum density for all computed models. The non-rotating model A and the slowly rotating model B show a very similar progression. The models C, D and E show, after relaxation of the bounce oscillations, a gradual increase in density. This is due to magnetic stresses, which gradually redistributes angular momentum causing a spin-down of the PNS.

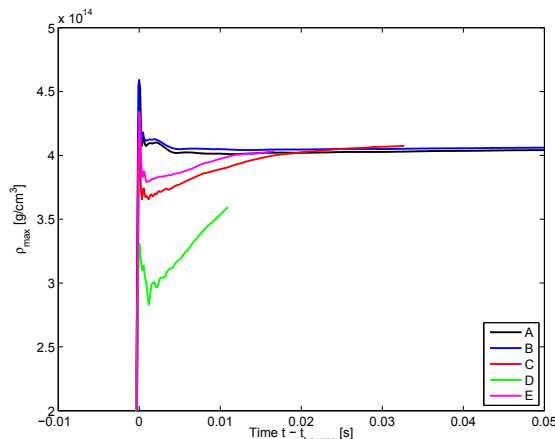


Figure 3.2: Evolution of the maximum density for all models. Note that the solidly rotating model B has a bit higher maximum density than the non-rotating model A, which may seem counterintuitive. We attribute this very small difference to differing code versions used for the two computations (a more recent code version was used for model B). However, the differences are very small.

Conservation of angular momentum in combination with the gravitational collapse leads to a massive spin-up and hence rotational deformation of the core. In figure 3.3, we show density contours for all rotating models at ~ 5 ms after core bounce. Due to the very low rotation, model B shows (upper left panel) no sign of deformation and is actually very similar to the non-rotating model A (not shown.) However, model C, D and E show significant rotationally induced deformations. The high density regions are more and more oblate, where the degree of deformation is set by the enclosed amount of angular momentum. These deformation show, that an axisymmetric gravitational potential as

described in 2.3.2 is necessary.

We note, however, that a 3D Poisson solver should be incorporated into our models. This is currently in development and preliminary results look promising (N. Vasset, private communication). As shown in [141, 82], non-axisymmetric motions and their associated non-axisymmetric gravitational potential may have interesting interaction and feedback onto the global dynamics of the high density regions.

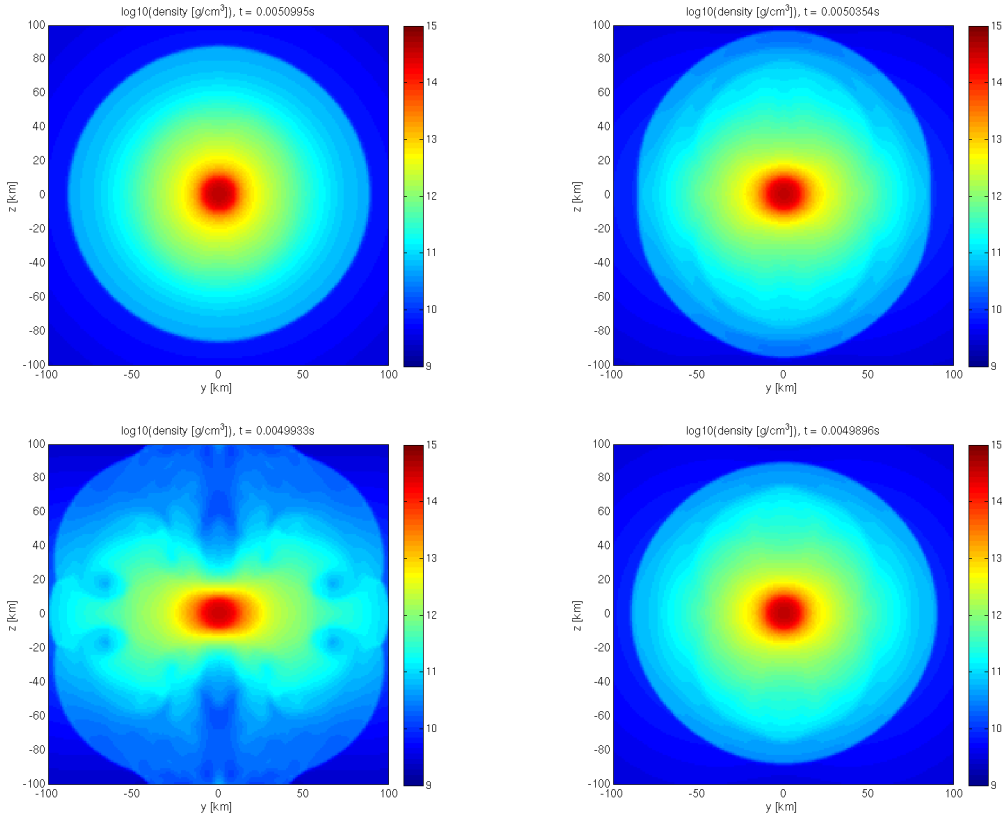


Figure 3.3: Density contour in the yz -plane ~ 5 ms after core bounce for all rotating models: Upper left B, upper right C, lower left D and lower right E.

In figure 3.4, we show entropy contours for all rotating models. From the figure, it is apparent that the different rotation laws alter also the shape of the shock wave and the strength of the shock wave. This is visible by the magnitude of the entropy of the shocked material. While for the solidly rotating model B the shock is very spherical (actually very similar to the non-rotating model A, which is not shown), the differentially rotating models C, D, and E significantly deviate from spherical symmetry and feature also higher entropies. As pointed out in [49, 79], the polar regions reach higher entropies than equatorial regions because of a stronger bounce in the poles. Along the poles, where centrifugal support is negligible, much higher infall velocities are achieved than in the equatorial regions. This effect seems to be particularly strong for model D. In this model differential rotation is very strong and with it associated conversion of poloidal field to toroidal field leads to a strong increase in magnetic pressure along the rotational axis. This already launches a bipolar jet along the rotational axis. For models C and E, however, it is clearly seen that higher entropies are generated along the poles than in the equatorial regions.

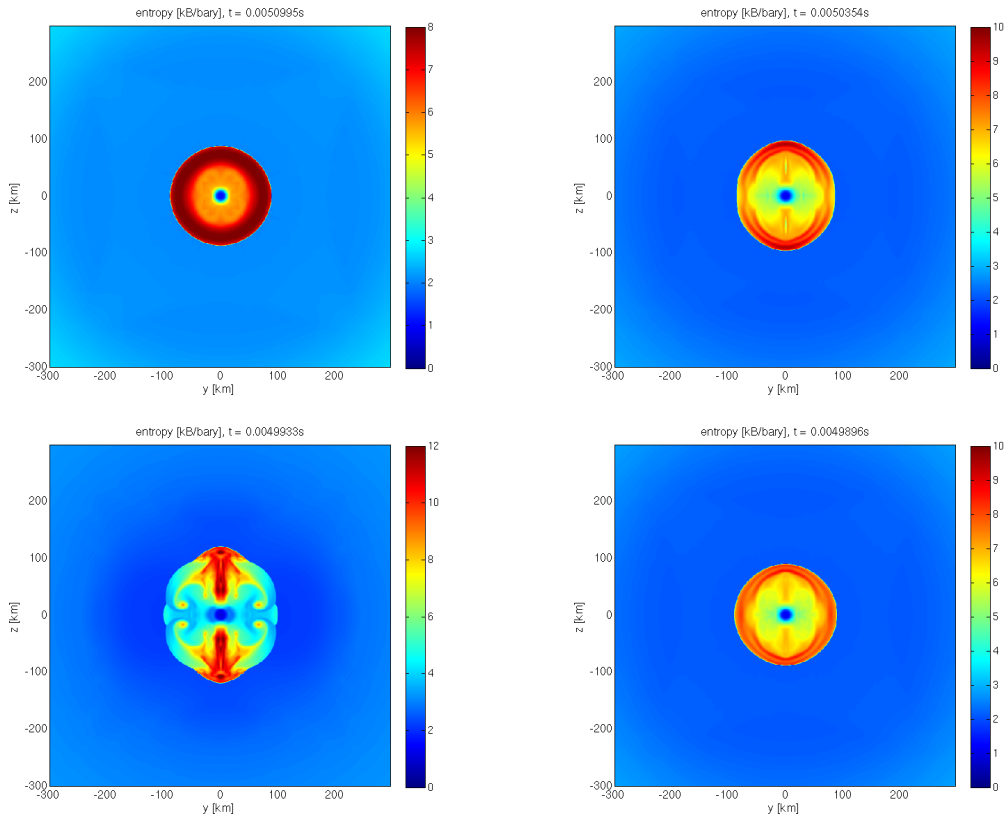


Figure 3.4: Entropy contour in the yz -plane ~ 5 ms after core bounce for all rotating models: Upper left B, upper right C, lower left D and lower right E.

3.3.2 Magnetic field amplification

In this subsection, we discuss the magnetic field amplification in detail. In figure 3.5, we show the evolution of the maximum poloidal and toroidal field strength as a function of maximum density during collapse up to core bounce. The figure displays all rotating models. Note that we define the poloidal and toroidal field components from the Cartesian components as follows

$$\begin{aligned}
 B_{\text{pol}} &= \left(B_x^2 \frac{x^2}{x^2 + y^2} + B_y^2 \frac{y^2}{x^2 + y^2} + B_z^2 \right)^{1/2} \\
 B_{\text{tor}} &= -B_x \frac{y}{\sqrt{x^2 + y^2}} + B_y \frac{x}{\sqrt{x^2 + y^2}}.
 \end{aligned}
 \tag{3.2}$$

During the collapse phase, the magnetic field is amplified gradually. Since our computational model is based on ideal MHD, the magnetic flux is conserved and the magnetic field lines are frozen into the magnetic fluid. Hence, from flux conservation, one easily derives that the magnetic field strength should increase as $B_{\text{max}} \propto \rho^{2/3}$ by compression alone. As apparent in the left panel of figure 3.5, this relation holds over several decades of density increase for the poloidal field strength. In the panel, the black line is a reference curve proportional to $\rho^{2/3}$. Note that all curves show a very similar trajectory, indicating that the detailed angular momentum distribution in the core does not alter significantly the amplification of the poloidal field during collapse. Accordingly, the poloidal field ampli-

fication is compression dominated. Only at densities above $2 \times 10^{14} \text{ g/cm}^3$, i.e. close to bounce, the poloidal field increases slightly faster.

The right panel of figure 3.5 shows that the maximum toroidal field trajectory differs from model to model. This is because the toroidal field not only grows by compression, but also by winding of poloidal into toroidal field by differential rotation. Hence the toroidal field grows slightly faster than $\rho^{2/3}$ as shown in [145]. Note also that all rotating models start with vanishing toroidal field and the different starting values in the right panel are because we only show B_{tor} for densities $\gtrsim 5 \times 10^{10} \text{ g/cm}^3$. The progenitor maximum density at onset of collapse is $\rho \approx 5 \times 10^9 \text{ g/cm}^3$. Therefore, the starting values differ due to the model's rotation law and with it associated differential rotation. Then the evolution of the toroidal field for all rotating models may be divided in three maximum density regimes. In the first regime, with $\rho_{\text{max}} \approx 5 \times 10^{10} - 10^{12} \text{ g/cm}^3$, we observe that the toroidal field increase significantly deviates from the expected growth by compression alone (compare to the black reference line $\propto \rho^{2/3}$). This density increase happens in the early stage of collapse and lasts for a relatively long duration of $\approx 40 \text{ ms}$. Thus differential rotation and winding amplification dominate in this regime, explaining the difference from the scaling relation by pure compression. In the second regime, with $\rho_{\text{max}} \approx 10^{12} - 2 \times 10^{14} \text{ g/cm}^3$, all curves evolve more or less parallel to the $\rho^{2/3}$ reference curve. Note that this density increase happens within only 4 ms and field winding is acting negligibly. In the third and last regime, we are close to bounce and the rotation is now strongly differential and the toroidal field increases again faster due to winding of the strong poloidal field. The same behaviour is observed by Shibata et al. [145]. Also note, that even the solidly rotating model A has some differential rotation apparent from the rapid increase due to winding shortly before core bounce. Hence, even for solid body rotation differential rotation is generated during the collapse by angular momentum conservation, since the inner regions collapse smaller relative distances than the outer regions [1, 125].

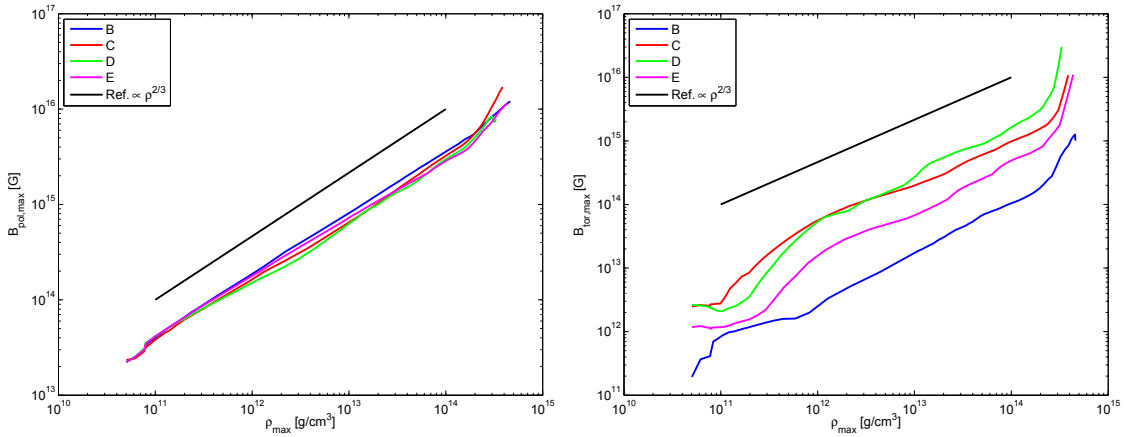


Figure 3.5: Evolution of the maximum poloidal (left) and toroidal (right) field strength as a function of central density for all rotating models. The black line depicts the relation expected from flux conservation $B_{\text{max}} \propto \rho^{2/3}$ in both panels.

In figure 3.6, we show the time evolution of the ratio of rotational kinetic energy T_{rot} to gravitational binding energy $|W|$ (left panel), the ratio of magnetic energy T_{mag} to $|W|$ (middle panel) and the ratio of poloidal $T_{\text{mag,pol}}$ and toroidal $T_{\text{mag,tor}}$ energy to $|W|$ (right panel) for all rotating models. From the left panel, we see that during collapse $T_{\text{rot}}/|W|$ monotonically increases, reaches a global maximum for models C, D, E and a

local maximum for model B. From the figure, we also observe that model E holds the highest amount of rotational energy followed by models C and E. Model B has the lowest rotational energy, because the material with high angular momentum has yet not accreted. This material should eventually accrete onto the PNS, but the simulation is yet not that advanced in time. In figure 3.7 is displayed the angular velocity around the rotational axis (here the z -axis) for all models at ≈ 5 ms after core bounce. From the figure, the hierarchy of $T_{\text{rot}}/|W|$ for the models becomes clear. Also note that the high angular velocity ($\log_{10}(\Omega_z) \gtrsim 3/2$) in model B is actually more due to violent prompt convection than the progenitor rotation itself. However, for models C, D, E we see that the inner regions have gained a large angular velocity with significant differential rotation. Thus, there is free energy available in differential rotation $T_{\text{rot,free}}$, which is the difference between the rotational kinetic energy T_{rot} and the kinetic energy for solid-body rotation $T_{\text{rot,solid}}$ at the same total angular momentum L_{tot}

$$T_{\text{rot,free}} = T_{\text{rot}}(L_{\text{tot}}) - T_{\text{rot,solid}}(L_{\text{tot}}). \quad (3.3)$$

Here the free energy is computed by determining the rotational kinetic energy of the PNS and subtracting from it the rotational kinetic energy from the same object if in solid-body rotation at the same angular momentum. The density profile in both cases is assumed to be identical and therefore this procedure is only approximate [30]. The amount of free rotational energy for material with $\rho > 10^{10}$ g/cm³ as a function of time is depicted in figure 3.8. From the figure, we observe that models C, D and E have significantly more energy stored in differential rotation than model B. Again, this is due to the fact, that the high angular momentum material in model B has not yet accreted. Note that the free energies for models C, D and E are as high as several 10^{51} erg. Therefore, there is ample energy to power a supernova. Our results for the free energy of rotation compare well to the ones observed by Burrows et al. [30] (see their figure 15).

The free energy in differential rotation is then immediately tapped by the magnetic field. The poloidal component is wound up into toroidal field. This is reflected in the rapid growth of the magnetic energy T_{mag} and the simultaneous decrease of the rotational energy (see figure 3.6). More specifically, the toroidal field energy grows by nearly two orders of magnitude within the first ~ 10 ms after core bounce. This reduces the amount of total rotational kinetic energy by extracting the free rotational energy, i.e. this reduces the degree of differential rotation by progressively forcing the material into solid-body rotation as it is reflected in the decrease of $T_{\text{rot,free}}$ (see figure 3.8). Note that the poloidal field energy changes only little, reflecting the fact that only the toroidal field is affected by differential rotation.

In figure 3.9, we show the contour of the free rotational energy density

$$e_{\text{rot,free}} = e_{\text{rot}}(L_{\text{tot}}) - e_{\text{rot,solid}}(L_{\text{tot}}) \quad (3.4)$$

in the upper panels and the contour of the toroidal field strength in the lower panels for models C, D and E. The figure shows a clear spatial correlation between the toroidal field strength and the amount of free rotational energy density.

From the above, we conclude that the poloidal magnetic field is amplified by compression during collapse. The toroidal magnetic field, which is initially zero, grows first by winding of poloidal field by the action of differential rotation and then subsequently also by flux conservation during collapse. The differential rotation is either already present in the initial rotation profile (as for models C, D, E) or is naturally generated by the nature of the collapse. After bounce, the large amount of free energy in differential rotation of

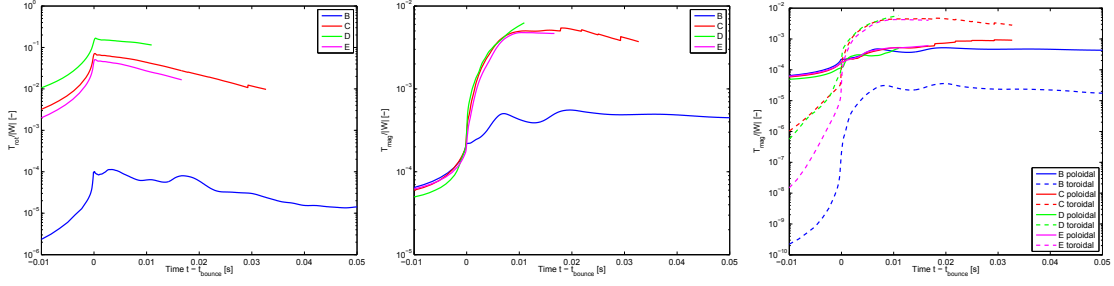


Figure 3.6: Evolution of the ratio of rotational kinetic energy T_{rot} to gravitational binding energy $|W|$ (left panel), the ratio of magnetic energy T_{mag} to $|W|$ (middle panel) and the ratio of poloidal $T_{\text{mag,pol}}$ and toroidal $T_{\text{mag,tor}}$ energy to $|W|$ (right panel) for all rotating models. Note the small humps in model C (red line) in all panels. These humps are due to the enlargement of the 3D computational domain to follow the propagation of the jet further in time and space.

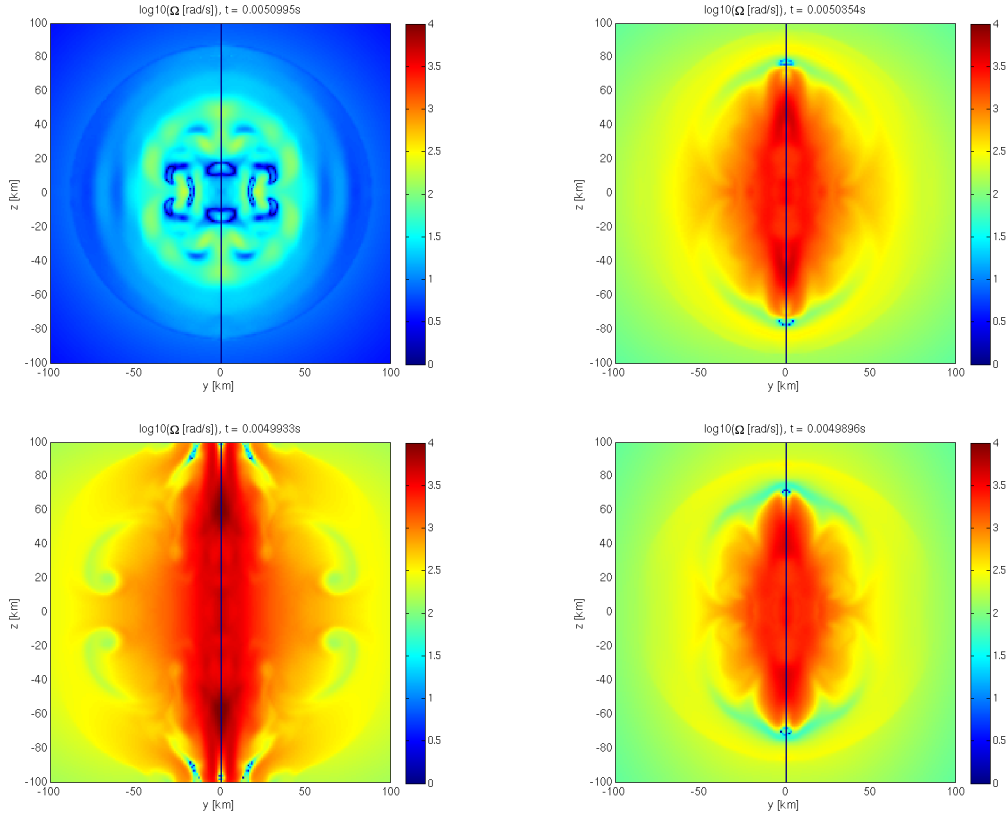


Figure 3.7: Angular velocity Ω_z contour in the yz -plane ~ 5 ms after core bounce for all rotating models: Upper left B, upper right C, lower left D and lower right E. Note that Ω_z is not well-defined along the rotational axis and is represented in dark blue.

models C, D and E is tapped by the magnetic field, increasing the magnetic energy at the expense of the former by winding poloidal field into toroidal. This is clearly seen in the strong increase of the toroidal magnetic energy in figure 3.6. For the initially solidly rotating model, there is roughly 3 orders of magnitude lower energy in differential rotation

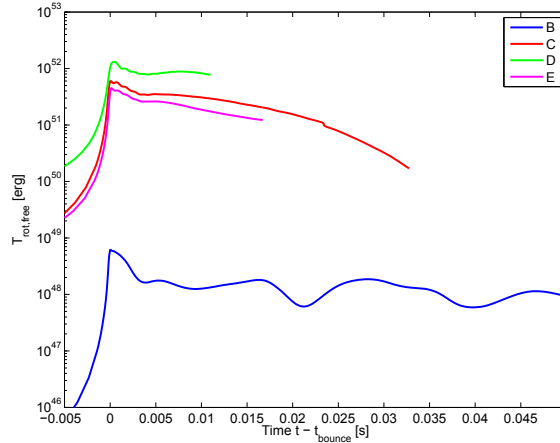


Figure 3.8: Free energy stored in differential rotation as a function of time for all rotating models for material with $\rho > 10^{10}$ g/cm³. Observe that the initially solidly rotating model B has indeed differential rotation, but a very low amount.

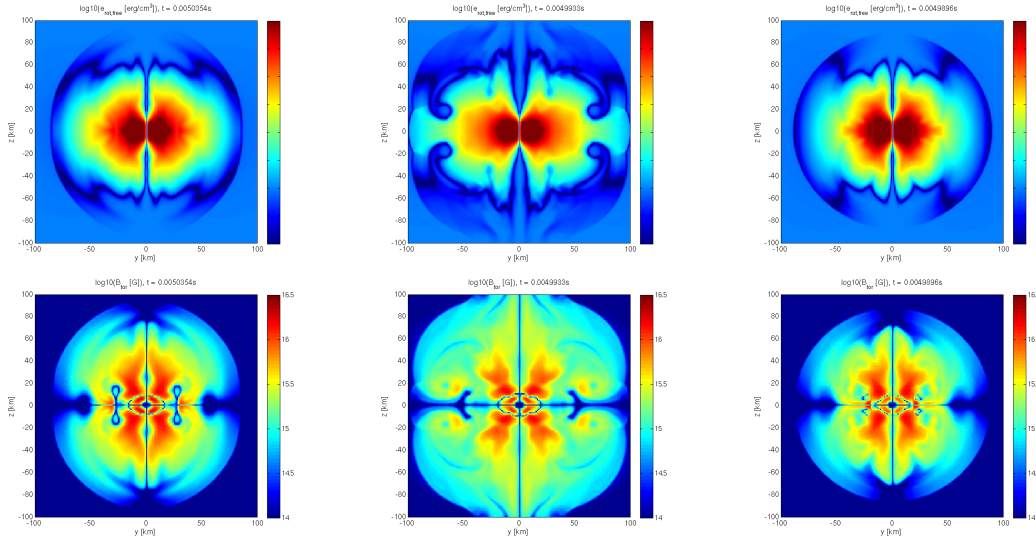


Figure 3.9: The upper panels show a contour of the free rotational energy in the yz -plane for the rotating models: Left C, middle D and right E. The lower panels show a contour of the toroidal field strength in the yz -plane for the rotating models: Left C, middle D and right E. Note that the absolute number of the free rotational energy is not relevant for the visualisation that the local free rotational energy density is spatially correlated with the regions of high toroidal field amplification.

available. Although, also for model B a strong increase in the toroidal magnetic energy is observed, this increase is, however, not strong enough yet to alter the dynamics. This might change once the further out material, holding a large angular momentum, accretes. Though, the simulation is currently not so far.

On the other hand, the poloidal magnetic energy grows not significantly after core bounce. This may indicate, that the MRI is not acting due to our limited spatial resolution, since the poloidal field should then also grow. But, since the field strength is already very high,

it could equally be, that the poloidal field has already reached saturation field strength (and this mostly by compression during collapse) [82, 122, 123, 145, 114]. This issue, however, can only be resolved by performing a (computationally) demanding resolution study which is beyond of the present work here and is postponed to a later study.

3.3.3 Formation and driving mechanism of bipolar outflow

In all our differential rotating models the bipolar jet outflow is initiated in a similar manner and thus we present mainly one representative model C. Furthermore, we have also used this model to study the jet propagation up to a radius of 700 km. Model B has not launched any jet during the time of the simulation which we stopped ~ 70 ms after bounce. This is mainly due to the short time evolution of the model, because the material with high angular momentum has yet not entered the 3D domain.

Hence, we focus now on model C. After bounce, the strong differential rotation winds the poloidal field very quickly into a very strong toroidal field increasing the magnetic energy and hence the magnetic pressure. As a consequence, strongly magnetised regions appear along the rotational axis. This triggers an increase in magnetic pressure, which quickly reaches and exceeds that of the local matter pressure. Then the outflow mechanism may be understood by considering the equation of motion

$$\rho \frac{d\mathbf{v}}{dt} = -\nabla p - \rho \nabla \phi - \mathbf{b} \times (\nabla \times \mathbf{b}), \quad (3.5)$$

where the terms on the right hand side come from the matter pressure force, the gravitational force and the magnetic force, i.e the Lorentz force. The Lorentz forces are the agencies of jet propulsion, and their direction explains the underlying dynamics. In figure 3.10 is shown a contour of the ratio of the matter pressure to magnetic pressure together with the direction of the Lorentz force at ~ 10 ms after bounce (lower panel). From the figure we see that along the rotational axis a region develops where the magnetic pressure becomes comparable and even exceeds the matter pressure. The Lorentz force then becomes dynamically important and the matter near the axis is lifted from the PNS along the rotational axis. As the directions of the vectors make clear, the vertical component of the Lorentz force along the rotational axis are pointing outward. This then drives the bipolar outflow along the rotational axis, i.e. the jets are launched. Additionally, the horizontal component of the Lorentz force points inward towards the rotational axis and thus partially confines the jet at this early stage.

In figure 3.11 the 3D magnetic field lines are shown at several time slices: ~ 14 ms, ~ 25 ms and ~ 31 ms after core bounce. In order to follow the jet propagation for longer times, we expanded the computational domain continuously from the standard 600^3 km up to $700 \times 700 \times 1400$ km. Thus we followed the jet propagation up to ~ 700 km in radius. The strong twisting of the field lines due to rotational winding behind the shock is clearly seen. This outflow structure resembles a tower, and hence is called a magnetic tower jet [104, 164]. Alternatively, the magnetic tower jet mechanism is also called the magneto-spring jet mechanism due to the tightly coiled spring like shape of the magnetic field lines. The energy in differential energy is consumed to wind up the poloidal field into toroidal field which increases the magnetic energy continuously within the shocked material. This can be seen in the left panel of figure 3.12. The magnetic energy, or equivalently the magnetic pressure, becomes dominant all along the rotational axis. This pushes matter predominantly along the poles leading to outward directed velocities: an explosion is initiated.

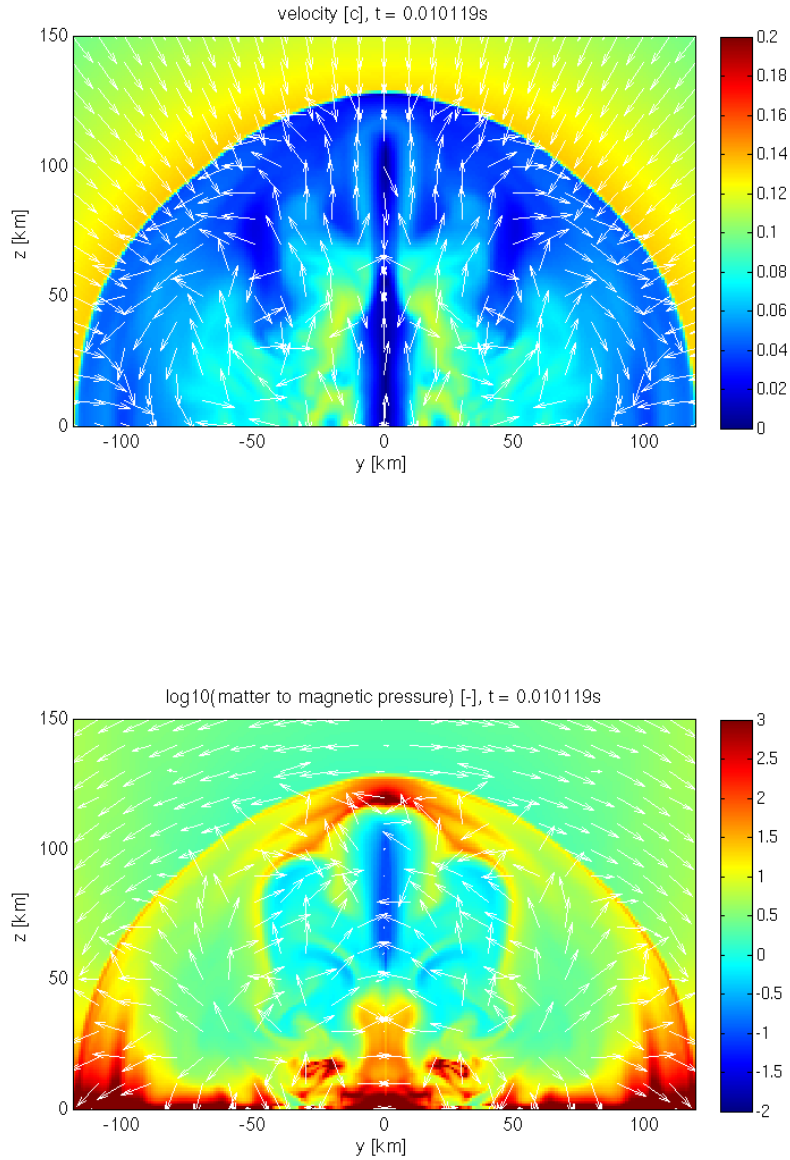


Figure 3.10: In the upper panel, a velocity contour with arrows indicating the direction of the velocity. In the lower panel a contour of the ratio of the matter pressure to magnetic pressure with arrows showing the direction of the Lorentz force.

While matter is pushed along the poles, toroidal field is stretched into poloidal field again. This can be seen in figure 3.11. Close to the PNS, the field is tightly wound and the toroidal field component clearly dominates. However, with increasing radius along the poles, a poloidal component becomes clearly visible in the increasingly helix-like magnetic field line trajectories. It has been proposed by Shibata et al. [145] on the basis of 2D

axisymmetric GR numerical simulations and more recently by Kuroda & Umeda [82] on the basis of 3D Newtonian and GR computations, that the jet driving mechanism transitions from a magnetic tower mechanism to a magneto-centrifugal supported mechanism. This mechanism is also known after the name of their inventors Blandford & Payne [20]. In this mechanism, matter is flung out along open magnetic field lines by the centrifugal force. In our simulations, this mechanism seems not to operate in accordance with [30]. However, we cannot exclude that the Blandford-Payne mechanism operates eventually at a later stage. For this we have to further advance our simulation in time and we postpone this to future investigations.

3.3.4 Explosion energy, ejected mass and its composition

The quickly expanding bipolar jets transport energy and stellar material outward against the gravitational attraction of the PNS, and, eventually escape it. In order to approximately determine the explosion energy and the amount of ejected matter, we define that a fluid parcel is ejected, if its specific total energy, i.e. the sum of specific internal energy, specific radial kinetic energy, specific magnetic energy and the gravitational potential is positive. In addition, we consider only fluid cells which have an outward pointing radial velocity component. Then the ejection criterion reads

$$\epsilon = e_{\text{int}} + \frac{v^2}{2} + \frac{b^2}{2\rho} + \phi > 0 \quad (3.6)$$

$$v_r > 0.$$

The total explosion energy and the ejected mass are then computed by simply integrating this criterion over the full 3D domain. These numbers are summarised in table 3.4.

Model	t_f [ms]	M_{ej} [M_{\odot}]	E_{exp} [erg]
C	33	6.72×10^{-3}	8.45×10^{49}

Table 3.4: Summary of the explosion characteristics: t_f indicates the final time of the simulation relative to core bounce, M_{ej} is the total ejected mass and E_{exp} the total explosion energy at end of the simulation. These number are computed as described in the text.

However, we stress here that our calculation of the explosion energy and the ejected mass are based on a very crude estimate. This numbers were still growing when the simulation was stopped and therefore may underestimate the actual values. Note that, if we compare the here estimated explosion energy $E_{\text{exp}} \sim 8.45 \times 10^{49}$ erg to the canonically observed $\sim 10^{51}$ erg, our estimate seems nevertheless reasonable.

In the right panel of figure 3.12 is shown a contour in the yz -plane of the explosion criteria eq. (3.6). The colorscale gives the asymptotic escape velocity v_{∞} , which is computed from the specific total energy (3.6) assuming that it is entirely converted into kinetic energy. An asymptotic escape velocity of zero indicates that the ejection criteria is not fulfilled. From the figure, we see that these outflow velocities can reach as high as 20% of the speed of light. This may question the validity our non-relativistic MHD approach and implies that a relativistic treatment may be necessary for the longer evolution of the jets.

As already repeatedly stated, the high velocity expanding jets are believed to be a promising site for r-process nucleosynthesis. In the middle panel of figure 3.12 is shown a contour of the electron abundance Y_e in the yz -plane. From the figure, we see that very neutron rich matter, due to the postbounce deleptonisation, is carried away in the jet and some of

this matter is ejected (according the criteria (3.6)). In the left panel of figure 3.13 is shown a histogram of the electron fraction and the with it associated ejected mass from the simulation. From the panel, we see that a significant amount of mass is indeed very neutron rich. In the right panel is shown the integrated mass fraction of the elements produced by detailed nucleosynthesis calculations on the basis of the present simulation (model C also featured $\sim 20'000$ tracer particles). From the figure it is seen, that the abundance distribution in the ejecta of our simulation fits the solar abundance very well in the mass region $120 < A < 200$. These nucleosynthesis calculations have been performed by C. Winteler and we refer to [174] for a detailed discussion of these results. Furthermore, these results agree with previous studies performed in 2D axisymmetry [120].

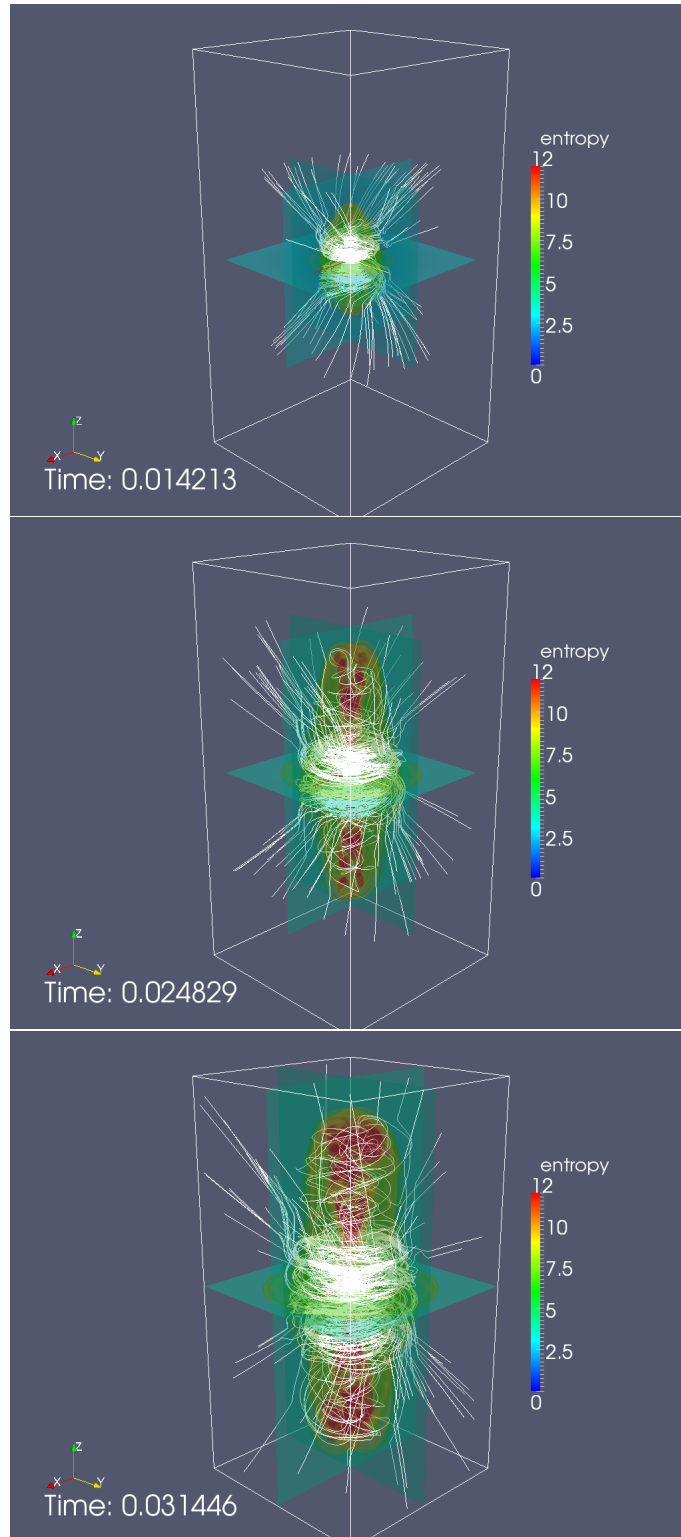


Figure 3.11: Three-dimensional plots of entropy contours spanning the coordinate planes with magnetic field lines. The time slices are ~ 14 ms, ~ 25 ms and ~ 31 ms after core bounce in the upper, middle and lower panel, respectively. The three-dimensional Cartesian domain was continuously expanded from 600^3 km³, $600 \times 600 \times 1000$ km³ and finally $700 \times 700 \times 1400$ km³. The white wire box shows the largest domain size in all panels. The very tightly wound toroidal field is clearly visible in all three time slices. Also note that the magnetic field in the accreting unshocked regions is of mainly poloidal character, which demonstrates that the winding mechanism is not acting very strongly during the collapse. As the jet propagates, the toroidal magnetic field lines are gradually stretched into poloidal ones and the field becomes more and more helical.

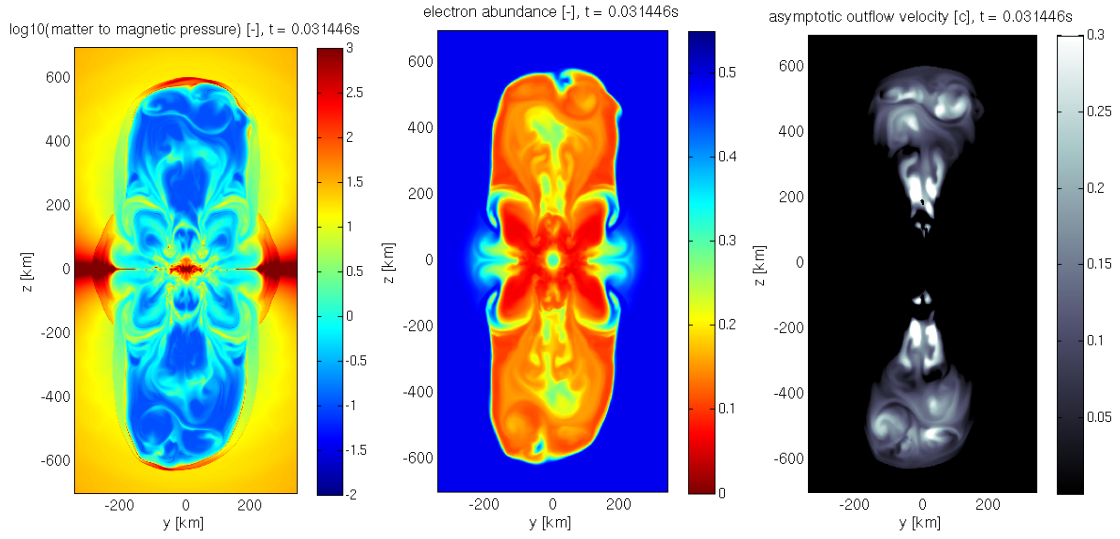


Figure 3.12: Contour in the yz -plane ~ 31 ms after core bounce: ratio of matter to magnetic pressure (left), electron abundance (middle) and asymptotic escape velocity (right). A zero value for the asymptotic escape velocity indicates that the ejection criteria is not fulfilled.

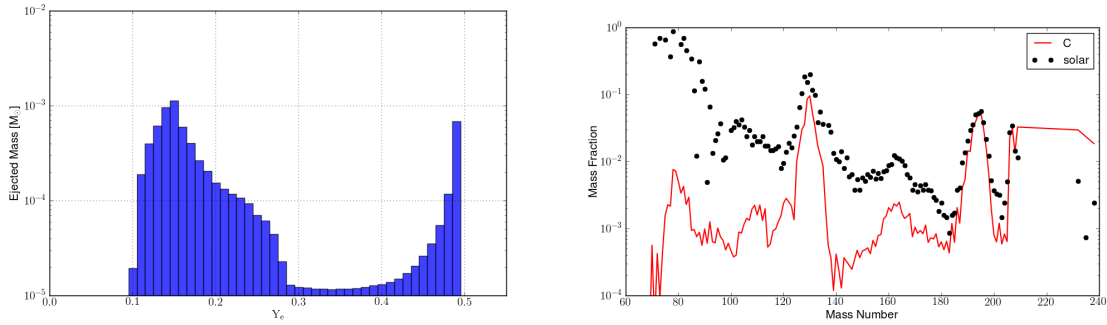


Figure 3.13: Left panel: mass distribution with respect to electron abundance Y_e for the matter fulfilling the ejection criteria. Right panel: Integrated mass fractions obtained by analytic expansion and nuclear-network post-processing on the simulation data (solid red line) and the solar r-process element distribution (black dots) scaled to fit the graph at $A = 162$. These figures are courtesy of C. Winteler.

Chapter 4

Summary and conclusions

We have applied the developed computational model described in the previous chapters to the study of the MHD-CCSN explosion mechanism. We have presented a series of 5 models exploring magneto-rotational supernova core collapse, bounce and jet formation with an approximate treatment of neutrino transport in the form of a spectral leakage scheme.

We have investigated the influence of 4 different rotational laws with the same amount of total angular momentum. In agreement with previous studies, we have found that initially solid-body rotation also results in differential rotation due to the nature of the collapse [1, 87, 125]. However, the generated differential rotation was not enough to trigger any significant MHD effects and the developed dynamics resembled the non-magnetic and non-rotating reference model. This is mainly due to the short simulation time, since the outer material featuring large angular momentum has not entered the 3D domain when the simulation was stopped. On the other hand, the rotation laws with initial differential rotation show significant rotationally induced deformation of the mass distribution.

In accord with previous studies, we find that the magnetic field is mostly amplified by compression during collapse up to bounce. While the poloidal field is also transformed to toroidal field by differential rotation during the collapse, the poloidal magnetic field remains dominant. Conservation of angular momentum in combination with the gravitational collapse leads to a massive spin-up of the core. For the initially differentially rotating models, the rotation becomes highly differential. After bounce, a large amount of free rotational energy is stored between the PNS and the sock wave. This free energy is immediately tapped by the magnetic field in winding poloidal to toroidal field and thus reducing the differential rotation. This leads to a rapid increase in the (toroidal) magnetic energy and magnetic pressure dominated regions are formed along the rotational axis. In these regions, the Lorentz force dominates the dynamics and this launches a strong out-flow along the poles. In the mean time, the continued accretion of differentially rotating material continuously makes new free energy available. However, because this mechanism is taking place on a very short time scale in our simulations (actually in a near prompt fashion), we could not observe the quasi-steady state evolution of this mechanism as observed by [30]. This is a vestige of the very high initial poloidal field strength adopted in our simulations for reasons to be explained below.

In one model, we have followed the jet for a longer time and distance by extending our 3D domain up to 700 km in radius along the jet. The jet rapidly propagated along the rotational axis. We identify the driving mechanism to be the so-called magnetic-tower or magneto-spring mechanism that may be only little aided by the Blandford-Payne magneto-centrifugal effect. This simulation resulted in an (early) estimate of the explosion energy

and the associated ejected mass. The ejecta was composed of very neutron rich matter and the outcome of the simulation was the basis for detailed nucleosynthesis calculations in a post-processing step [174]. These calculations revealed that the prevailing conditions could reproduce the global solar r-process pattern. The results also show a good qualitative agreement with 2D axisymmetric simulations [120].

However, the MHD-CCSN may not be the standard explosion mechanism of CCSN. This mechanism might be at work for only a small subset of massive stars, since it requires rather extreme conditions for rotation and magnetic fields. Furthermore, from the here computed ejected mass and its r-process nucleosynthesis [174], these numbers can only be brought in agreement with the nowadays observed abundance pattern if only a fraction (perhaps 0.1 – 1%) of CCSN explode with the MHD mechanism. This also agrees with the observed large star-to-star scatter of r-process element abundances in very old halo stars indicating the scarcity of these events [147].

The presented numerical simulations also revealed some deficiencies. First, we observed in all simulations a strong loss of angular momentum. This is shown in figure 4.1 depicting the integrated angular momentum distribution as function of enclosed mass for two simulations with similar initial conditions as model C, but with a lower initial poloidal field magnetic strength $B_{\text{pol}} = 10^{12}$ G. This has the effect to delay the generation of the jets. The blue line is the initial angular momentum profile, the red lines show the simulation performed with an older code version and the green lines with a new version. The difference between the newer and older version relies in the fluid advection scheme. The new version employs the scheme developed in 2.1 together with the approximately well-balanced reconstruction and gravity source term integration 2.2. From the figure we observe that the old code version has spuriously dissipated $\sim 20\%$ of the total angular momentum within 49 ms after core bounce. Unfortunately, the simulations presented here have been performed with the older code version. This explains, at least from a practical standpoint, why we had to impose the strong initial fields: the magnetic effects should happen rapidly enough so that the angular momentum losses are not so severe.

Second, we have observed spurious entropy decreases in regions where the magnetic pressure exceeds the matter pressure. The origin of this problem is yet not fully understood. The problem actually happens at ratios of $p/p_{\text{mag}} \lesssim 0.1$, which in the presented test problems in 2.1.8 posed no major problems. Currently, we suppose that this may be linked to the EoS, but this will need further investigations. In order to practically fix this problem, we have implemented also an advection equation for the entropy. In case the entropy computed standardly from the total energy equation strongly decreases in regions dominated by the magnetic pressure, we use the result from the entropy advection equation. Since this switch is applied only in regions (highly) dominated by the magnetic field, we don't expect a severe violation of total energy conservation and also the shock speeds.

The resolution of these two issues should enable us to perform MHD-CCSN simulations covering a longer stretch of physical time with more reasonable initial conditions.

In summary, the physical and numerical aspects of our simulations that distinguish them from previous studies of the MHD-CCSN explosion mechanism includes the following:

1. They are fully 3D and therefore no dimensional restriction is applied.
2. The use of a microphysical EoS state. All previous studies devoted only to MHD-CCSN performed in 3D employed a gamma-law EoS.
3. The approximate treatment of neutrino transport in the form of a multidimensional spectral leakage scheme. This allows us to follow the deleptonisation during collapse

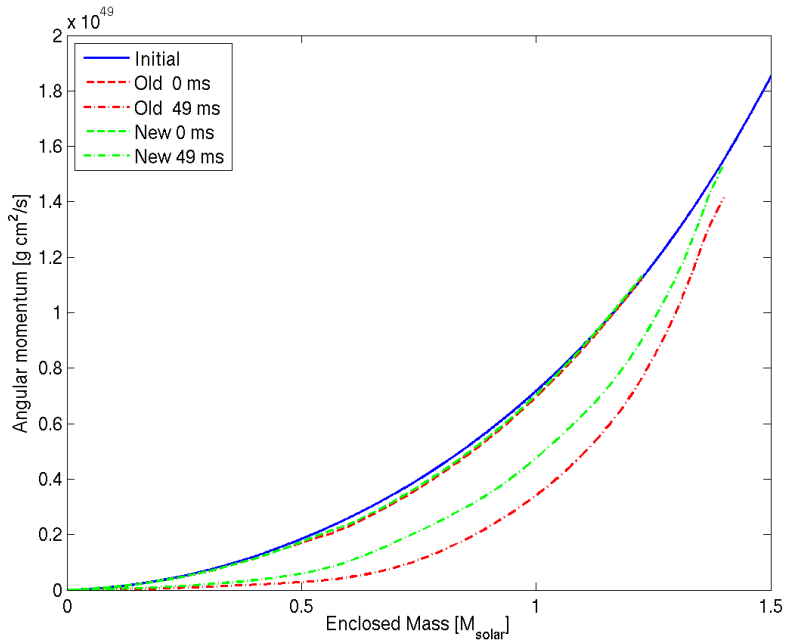


Figure 4.1: Total angular momentum profile as function of enclosed mass. The solid blue line is the initial distribution, the red lines are computed with an older code version and the green lines with a newer code version. The dashed lines show the total angular momentum profile in the biggest enclosed sphere in the 3D domain at bounce and the dash-dotted lines ~ 49 ms after core bounce. We see that at bounce both code version agree well and that no significant angular momentum transport has occurred during collapse. At 49 ms, we see that the angular momentum has been redistributed (this is due to magnetic stresses). We also see that the older code version has lost $\sim 20\%$ of enclosed angular momentum while the new version agrees well with the expected value. The lost angular momentum has been spuriously numerically dissipated.

and after core bounce resulting in a neutron rich environment.

4. The approximate inclusion of general relativity by an effective gravitational potential mimicking the deeper gravitational well of the relativistic case.
5. Last but not least, the expel of very neutron rich mater along the bipolar outflow was shown to be a promising site for r-process nucleosynthesis.

The major limitations of our simulations are as follows:

1. The relatively short postbounce simulation time due to spurious angular momentum losses. This limits the detailed study of jet formation on a longer time scale.
2. The strong initial magnetic fields, which are necessary to observe a quickly developing jet-like explosion before angular momentum losses inhibit it.
3. Our limited spatial resolution (1 km), which inhibits the development of fast magnetic field amplification mechanism like the MRI and/or dynamo action. This also forces us to use strong initial magnetic fields.

4. The approximate neutrino transport with a spectral leakage scheme accounting only for neutrino cooling. Even though, that neutrino heating may only add fractional contribution to the explosion, neutrino heating can change the neutron to proton ratio and thus alter the outcome of the nucleosynthesis.
5. The non-relativistic MHD approach and the only approximate treatment of general relativity.

We currently think that we have resolved issue 1 and 2. For issue 4, we can eventually integrate into our model the approximate neutrino transport provided by the computationally efficient isotropic diffusion source approximation [102]. Generalising `FISH` to special relativity would resolve partially issue 5 and we have already started this task with encouraging, yet only 1D, preliminary results. However, issue 3 may be difficult to resolve by brute force computational power and/or adaptive grids (like adaptive mesh refinement). Perhaps the usage of a MHD subgrid turbulence model could relax this issue. These steps go beyond the scope of this thesis and will be addressed in subsequent work.

Bibliography

- [1] S. Akiyama, J. C. Wheeler, D. L. Meier, and I. Lichtenstadt. The magnetorotational instability in core-collapse supernova explosions. *ApJ*, 584:954–970, February 2003.
- [2] N. V. Ardeljan, G. S. Bisnovatyi-Kogan, and S. G. Moiseenko. Collapse of a Magnetized Rotating Cloud 2D Numerical Simulations. *Ap&SS*, 274:389–397, October 2000.
- [3] N. V. Ardeljan, G. S. Bisnovatyi-Kogan, and S. G. Moiseenko. Nonstationary magnetorotational processes in a rotating magnetized cloud. *A&A*, 355:1181–1190, March 2000.
- [4] N. V. Ardeljan, G. S. Bisnovatyi-Kogan, and S. G. Moiseenko. Magnetorotational supernovae. *MNRAS*, 359:333–344, May 2005.
- [5] D. Arnett. *Supernovae and nucleosynthesis: an investigation of the history of matter, from the big bang to the present*. Princeton series in astrophysics. Princeton University Press, 1996.
- [6] W. D. Arnett and C. Meakin. Toward Realistic Progenitors of Core-collapse Supernovae. *ApJ*, 733:78–+, June 2011.
- [7] M. Arnould, S. Goriely, and K. Takahashi. The r-process of stellar nucleosynthesis: Astrophysics and nuclear physics achievements and mysteries. *Phys. Rep.*, 450:97–213, September 2007.
- [8] Emmanuel Audusse, François Bouchut, Marie-Odile Bristeau, Rupert Klein, and Benoît Perthame. A fast and stable well-balanced scheme with hydrostatic reconstruction for shallow water flows. *SIAM Journal on Scientific Computing*, 25(6):2050–2065, 2004.
- [9] W. Baade and F. Zwicky. Cosmic Rays from Super-novae. *Proceedings of the National Academy of Science*, 20:259–263, May 1934.
- [10] W. Baade and F. Zwicky. On Super-novae. *Proceedings of the National Academy of Science*, 20:254–259, May 1934.
- [11] S. A. Balbus and J. F. Hawley. A Powerful Local Shear Instability in Weakly Magnetized Disks. IV. Nonaxisymmetric Perturbations. *ApJ*, 400:610–621, December 1992.
- [12] S. A. Balbus and J. F. Hawley. Instability, turbulence, and enhanced transport in accretion disks. *Reviews of Modern Physics*, 70:1–53, January 1998.

- [13] Dinshaw S. Balsara and Daniel S. Spicer. A staggered mesh algorithm using high order godunov fluxes to ensure solenoidal magnetic fields in magnetohydrodynamic simulations. *J. Comput. Phys.*, 149(2):270–292, March 1999.
- [14] J. Barnes and P. Hut. A hierarchical $O(N \log N)$ force-calculation algorithm. *Nature*, 324:446–449, December 1986.
- [15] E. Baron and J. Cooperstein. The effect of iron core structure on supernovae. *ApJ*, 353:597–611, April 1990.
- [16] P. Batten, N. Clarke, C. Lambert, and D. M. Causon. On the choice of wavespeeds for the hllc riemann solver. *SIAM Journal on Scientific Computing*, 18(6):1553–1570, 1997.
- [17] H. A. Bethe. Supernova mechanisms. *Reviews of Modern Physics*, 62:801–866, 1990.
- [18] H. A. Bethe and J. R. Wilson. Revival of a stalled supernova shock by neutrino heating. *ApJ*, 295:14–23, August 1985.
- [19] G. S. Bisnovatyi-Kogan, I. P. Popov, and A. A. Samokhin. The magnetohydrodynamic rotational model of supernova explosion. *Ap&SS*, 41:287–320, June 1976.
- [20] R. D. Blandford and D. G. Payne. Hydromagnetic flows from accretion discs and the production of radio jets. *MNRAS*, 199:883–903, June 1982.
- [21] N. Botta, R. Klein, S. Langenberg, and S. L. tzenkirchen. Well balanced finite volume methods for nearly hydrostatic flows. *Journal of Computational Physics*, 196(2):539 – 565, 2004.
- [22] J. U. Brackbill and D. C. Barnes. The effect of nonzero [backward difference] · b on the numerical solution of the magnetohydrodynamic equations. *J. Comput. Phys.*, 35(3):426–430, May 1980.
- [23] W.L. Briggs, V.E. Henson, and S.F. McCormick. *A multigrid tutorial*. Miscellaneous Bks. Society for Industrial and Applied Mathematics, 2000.
- [24] E. F. Brown, A. C. Calder, T. Plewa, P. M. Ricker, K. Robinson, and J. B. Gallagher. Type Ia Supernovae: Simulations and Nucleosynthesis. *Nuclear Physics A*, 758:451–454, July 2005.
- [25] G. E. Brown, H. A. Bethe, and G. Baym. Supernova theory. *Nuclear Physics A*, 375:481–532, February 1982.
- [26] S. W. Bruenn. Stellar core collapse - Numerical model and infall epoch. *ApJS*, 58:771–841, August 1985.
- [27] S. W. Bruenn, K. R. De Nisco, and A. Mezzacappa. General Relativistic Effects in the Core Collapse Supernova Mechanism. *ApJ*, 560:326–338, October 2001.
- [28] R. Buras, H.-T. Janka, M. Rampp, and K. Kifonidis. Two-dimensional hydrodynamic core-collapse supernova simulations with spectral neutrino transport. II. Models for different progenitor stars. *A&A*, 457:281–308, October 2006.
- [29] A. Burrows. Supernova explosions in the Universe. *Nature*, 403:727–733, February 2000.

- [30] A. Burrows, L. Dessart, E. Livne, C. D. Ott, and J. Murphy. Simulations of Magnetically Driven Supernova and Hypernova Explosions in the Context of Rapid Rotation. *ApJ*, 664:416–434, July 2007.
- [31] A. Burrows, W. B. Hubbard, J. I. Lunine, and J. Liebert. The theory of brown dwarfs and extrasolar giant planets. *Reviews of Modern Physics*, 73:719–765, July 2001.
- [32] A. Burrows, E. Livne, L. Dessart, C. D. Ott, and J. Murphy. A New Mechanism for Core-Collapse Supernova Explosions. *ApJ*, 640:878–890, April 2006.
- [33] A. Burrows, E. Livne, L. Dessart, C. D. Ott, and J. Murphy. Features of the Acoustic Mechanism of Core-Collapse Supernova Explosions. *ApJ*, 655:416–433, January 2007.
- [34] P. Cerdá-Durán, J. A. Font, and H. Dimmelmeyer. General relativistic simulations of passive-magneto-rotational core collapse with microphysics. *A&A*, 474:169–191, October 2007.
- [35] G. Chabrier and I. Baraffe. Theory of Low-Mass Stars and Substellar Objects. *ARA&A*, 38:337–377, 2000.
- [36] J. Chadwick. Possible Existence of a Neutron. *Nature*, 129:312–+, February 1932.
- [37] S. Chandrasekhar. *An introduction to the study of stellar structure*. New York: Dover, 1967.
- [38] Stephen J. Chapman. *FORTRAN 90/95 for Scientists and Engineers*. McGraw Hill Higher Education, 2003.
- [39] S. A. Colgate and R. H. White. The Hydrodynamic Behavior of Supernovae Explosions. *ApJ*, 143:626–+, March 1966.
- [40] Stirling A. Colgate and Montgomery H. Johnson. Hydrodynamic origin of cosmic rays. *Phys. Rev. Lett.*, 5(6):235–238, Sep 1960.
- [41] R. Courant, K. Friedrichs, and H. Lewy. über die partiellen differenzgleichungen der mathematischen physik. *Mathematische Annalen*, 100(1):32–74, December 1928.
- [42] Wenlong Dai and Paul R. Woodward. A simple finite difference scheme for multidimensional magnetohydrodynamical equations. *J. Comput. Phys.*, 142(2):331 – 369, 1998.
- [43] J.-F. Donati and J. D. Landstreet. Magnetic Fields of Nondegenerate Stars. *ARA&A*, 47:333–370, September 2009.
- [44] R. C. Duncan and C. Thompson. Formation of very strongly magnetized neutron stars - Implications for gamma-ray bursts. *ApJ*, 392:L9–L13, June 1992.
- [45] Y. Eriguchi and E. Mueller. A general computational method for obtaining equilibria of self-gravitating and rotating gases. *A&A*, 146:260–268, May 1985.
- [46] C. R. Evans and J. F. Hawley. Simulation of magnetohydrodynamic flows - a constrained transport method. *ApJ*, 332:659–677, September 1988.

- [47] A. V. Filippenko. Optical Spectra of Supernovae. *ARA&A*, 35:309–355, 1997.
- [48] T. Fischer, I. Sagert, G. Pagliara, M. Hempel, J. Schaffner-Bielich, T. Rauscher, F. -. Thielemann, R. Käppeli, G. Martínez-Pinedo, and M. Liebendörfer. The revival of an explosion mechanism of massive stars - the quark hadron phase transition during the early post bounce phase of core collapse supernovae. *ArXiv e-prints*, November 2010.
- [49] C. L. Fryer and M. S. Warren. The Collapse of Rotating Massive Stars in Three Dimensions. *ApJ*, 601:391–404, January 2004.
- [50] B. Fryxell, K. Olson, P. Ricker, F. X. Timmes, M. Zingale, D. Q. Lamb, P. MacNeice, R. Rosner, J. W. Truran, and H. Tufo. FLASH: An Adaptive Mesh Hydrodynamics Code for Modeling Astrophysical Thermonuclear Flashes. *ApJS*, 131:273–334, November 2000.
- [51] F.G. Fuchs, A.D. McMurry, S. Mishra, N.H. Risebro, and K. Waagan. High order well-balanced finite volume schemes for simulating wave propagation in stratified magnetic atmospheres. *Journal of Computational Physics*, 229(11):4033 – 4058, 2010.
- [52] Franz G. Fuchs, Kenneth H. Karlsen, Siddharta Mishra, and Nils H. Risebro. Stable upwind schemes for the magnetic induction equation. *M2AN Math. Model. Numer. Anal.*, 43(5):825–852, 2009.
- [53] T. A. Gardiner and J. M. Stone. An unsplit Godunov method for ideal MHD via constrained transport. *J. Comput. Phys.*, 205:509–539, May 2005.
- [54] Thomas A. Gardiner and James M. Stone. An unsplit godunov method for ideal mhd via constrained transport in three dimensions. *J. Comput. Phys.*, 227(8):4123–4141, April 2008.
- [55] N. A. Gentile, M. B. Aufderheide, G. J. Mathews, F. D. Swesty, and G. M. Fuller. The QCD phase transition and supernova core collapse. *ApJ*, 414:701–711, September 1993.
- [56] S. K. Godunov. A difference method for numerical calculation of discontinuous solutions of the equations of hydrodynamics. *Mat. Sb. (N.S.)*, 47 (89):271–306, 1959.
- [57] P. Goldreich and S. V. Weber. Homologously collapsing stellar cores. *ApJ*, 238:991–997, June 1980.
- [58] L Greengard and V Rokhlin. A fast algorithm for particle simulations. *Journal of Computational Physics*, 73(2):325 – 348, 1987.
- [59] W. Gropp, E. Lusk, and A. Skjellum. *Using MPI*. Number Bd. 2 in Scientific and engineering computation. MIT Press, 1999.
- [60] M. Hamuy. Review on the Observed and Physical Properties of Core Collapse Supernovae. *ArXiv Astrophysics e-prints*, December 2003.

- [61] Ami Harten, Björn Engquist, Stanley Osher, and Sukumar R. Chakravarthy. Uniformly high-order accurate essentially nonoscillatory schemes. III. *J. Comput. Phys.*, 71(2):231–303, 1987.
- [62] Amiram Harten, Peter D. Lax, and Bram van Leer. On upstream differencing and godunov-type schemes for hyperbolic conservation laws. *SIAM Review*, 25(1):35–61, 1983.
- [63] A. Heger, C. L. Fryer, S. E. Woosley, N. Langer, and D. H. Hartmann. How Massive Single Stars End Their Life. *ApJ*, 591:288–300, July 2003.
- [64] A. Heger, N. Langer, and S. E. Woosley. Presupernova Evolution of Rotating Massive Stars. I. Numerical Method and Evolution of the Internal Stellar Structure. *ApJ*, 528:368–396, January 2000.
- [65] A. Heger, S. E. Woosley, and H. C. Spruit. Presupernova Evolution of Differentially Rotating Massive Stars Including Magnetic Fields. *ApJ*, 626:350–363, June 2005.
- [66] M. Hempel, T. Fischer, J. Schaffner-Bielich, and M. Liebendörfer. New equations of state in core-collapse supernova simulations. *ArXiv e-prints*, August 2011.
- [67] M. Herant, W. Benz, W. R. Hix, C. L. Fryer, and S. A. Colgate. Inside the supernova: A powerful convective engine. *ApJ*, 435:339–361, November 1994.
- [68] W. Hillebrandt and J. C. Niemeyer. Type ia supernova explosion models. *ARA&A*, 38:191–230, 2000.
- [69] R. Hirschi, G. Meynet, and A. Maeder. Stellar evolution with rotation. XII. Pre-supernova models. *A&A*, 425:649–670, October 2004.
- [70] W. Iwakami, K. Kotake, N. Ohnishi, S. Yamada, and K. Sawada. Three-Dimensional Simulations of Standing Accretion Shock Instability in Core-Collapse Supernovae. *ApJ*, 678:1207–1222, May 2008.
- [71] John David Jackson. *Classical Electrodynamics Third Edition*. Wiley, 1998.
- [72] H.-T. Janka, K. Langanke, A. Marek, G. Martínez-Pinedo, and B. Müller. Theory of core-collapse supernovae. *Phys. Rep.*, 442:38–74, April 2007.
- [73] H.-T. Janka and E. Mueller. Neutrino heating, convection, and the mechanism of Type-II supernova explosions. *A&A*, 306:167–+, February 1996.
- [74] S. Jin and Z. Xin. The relaxation schemes for systems of conservation laws in arbitrary space dimensions. *Comm. Pure and Appl. Math.*, 48:235–276, 1995.
- [75] R. Käppeli, S. C. Whitehouse, S. Scheidegger, U.-L. Pen, and M. Liebendörfer. FISH: A Three-dimensional Parallel Magnetohydrodynamics Code for Astrophysical Applications. *ApJS*, 195:20–+, August 2011.
- [76] S.D. Kawaler, I.D. Novikov, and G. Srinivasan. *Stellar remnants*. Number Bd. 25, Teil 1995 in Saas-Fee advanced course ... lecture notes. Springer, 1997.
- [77] F. S. Kitaura, H.-T. Janka, and W. Hillebrandt. Explosions of O-Ne-Mg cores, the Crab supernova, and subluminal type II-P supernovae. *A&A*, 450:345–350, April 2006.

- [78] K. Kotake, K. Sato, and K. Takahashi. Explosion mechanism, neutrino burst and gravitational wave in core-collapse supernovae. *Reports of Progress in Physics*, 69:971–1143, April 2006.
- [79] K. Kotake, H. Sawai, S. Yamada, and K. Sato. Magnetorotational Effects on Anisotropic Neutrino Emission and Convection in Core-Collapse Supernovae. *ApJ*, 608:391–404, June 2004.
- [80] C. Kouveliotou, S. Dieters, T. Strohmayer, J. van Paradijs, G. J. Fishman, C. A. Meegan, K. Hurley, J. Kommers, I. Smith, D. Frail, and T. Murakami. An X-ray pulsar with a superstrong magnetic field in the soft γ -ray repeater SGR1806 - 20. *Nature*, 393:235–237, May 1998.
- [81] R.M. Kulsrud. *Plasma physics for astrophysics*. Princeton series in astrophysics. Princeton University Press, 2005.
- [82] T. Kuroda and H. Umeda. Three-dimensional Magnetohydrodynamical Simulations of Gravitational Collapse of a 15 M_{sun} Star. *ApJS*, 191:439–466, December 2010.
- [83] Lev D. Landau and Evgenij M. Lifschitz. *Lehrbuch der theoretischen Physik, 10 Bde., Bd.8, Elektrodynamik der Kontinua*. Deutsch (Harri), 1991.
- [84] Lev D. Landau, Evgenij M. Lifschitz, and Wolfgang Weller. *Lehrbuch der theoretischen Physik, 10 Bde., Bd.6, Hydrodynamik*. Deutsch (Harri), 1991.
- [85] Culbert B. Laney. *Computational Gasdynamics*. Cambridge University Press, 1998.
- [86] J. M. Lattimer and F. D. Swesty. A generalized equation of state for hot, dense matter. *Nuclear Physics A*, 535:331–376, December 1991.
- [87] J. M. LeBlanc and J. R. Wilson. A Numerical Example of the Collapse of a Rotating Magnetized Star. *ApJ*, 161:541–+, August 1970.
- [88] Dongwook Lee and Anil E. Deane. An unsplit staggered mesh scheme for multidimensional magnetohydrodynamics. *Journal of Computational Physics*, 228(4):952 – 975, 2009.
- [89] Randall LeVeque. A well-balanced path-integral f-wave method for— hyperbolic problems with source terms. *Journal of Scientific Computing*, pages 1–18, 2010. 10.1007/s10915-010-9411-0.
- [90] Randall J. LeVeque. *Numerical Methods for Conservation Laws*. Birkhäuser, 1992.
- [91] Randall J. LeVeque. Balancing source terms and flux gradients in high-resolution godunov methods: The quasi-steady wave-propagation algorithm. *J. Comput. Phys.*, 146(1):346–365, October 1998.
- [92] Randall J. LeVeque. *Finite Volume Methods for Hyperbolic Problems (Cambridge Texts in Applied Mathematics)*. Cambridge University Press, 1 edition, 8 2002.
- [93] Randall J. LeVeque and Derek S. Bale. Wave-propagation methods for conservation laws with source terms. *Proc. 7th Intl. Conf. on Hyperbolic Problems*, 1998.
- [94] Randall J. LeVeque, Dimitri Mihalas, and E. A. Dorfi. *Computational Methods for Astrophysical Fluid Flow*. Springer, Berlin, 2005.

- [95] Randall J. LeVeque and Marica Pelanti. A class of approximate riemann solvers and their relation to relaxation schemes. *J. Comput. Phys.*, 172(2):572–591, September 2001.
- [96] M. Liebendörfer. A Simple Parameterization of the Consequences of Deleptonization for Simulations of Stellar Core Collapse. *ApJ*, 633:1042–1051, November 2005.
- [97] M. Liebendörfer, O. E. B. Messer, A. Mezzacappa, S. W. Bruenn, C. Y. Cardall, and F.-K. Thielemann. A Finite Difference Representation of Neutrino Radiation Hydrodynamics in Spherically Symmetric General Relativistic Spacetime. *ApJS*, 150:263–316, January 2004.
- [98] M. Liebendörfer, A. Mezzacappa, F.-K. Thielemann, O. E. Messer, W. R. Hix, and S. W. Bruenn. Probing the gravitational well: No supernova explosion in spherical symmetry with general relativistic boltzmann neutrino transport. *Phys. Rev. D*, 63(10):103004–+, May 2001.
- [99] M. Liebendörfer, U. Pen, and C. Thompson. Approaching the dynamics of hot nucleons in supernovae. *Nucl. Phys. A*, 758:59–62, July 2005.
- [100] M. Liebendörfer, M. Rampp, H.-T. Janka, and A. Mezzacappa. Supernova simulations with boltzmann neutrino transport: A comparison of methods. *ApJ*, 620:840–860, February 2005.
- [101] M. Liebendörfer, S. Rosswog, and F.-K. Thielemann. An adaptive grid, implicit code for spherically symmetric, general relativistic hydrodynamics in comoving coordinates. *ApJS*, 141:229–246, July 2002.
- [102] M. Liebendörfer, S. C. Whitehouse, and T. Fischer. The Isotropic Diffusion Source Approximation for Supernova Neutrino Transport. *ApJ*, 698:1174–1190, June 2009.
- [103] P. Londrillo and L. Del Zanna. On the divergence-free condition in godunov-type schemes for ideal magnetohydrodynamics: the upwind constrained transport method. *J. Comput. Phys.*, 195(1):17–48, March 2004.
- [104] D. Lynden-Bell. Magnetic collimation by accretion discs of quasars and stars. *MNRAS*, 279:389–401, March 1996.
- [105] A. Maeder. *Physics, Formation and Evolution of Rotating Stars*. 2009.
- [106] A. Marek, H. Dimmelmeier, H.-T. Janka, E. Müller, and R. Buras. Exploring the relativistic regime with newtonian hydrodynamics: an improved effective gravitational potential for supernova simulations. *A&A*, 445:273–289, January 2006.
- [107] A. Marek and H.-T. Janka. Delayed Neutrino-Driven Supernova Explosions Aided by the Standing Accretion-Shock Instability. *ApJ*, 694:664–696, March 2009.
- [108] G. Martínez-Pinedo, M. Liebendörfer, and D. Frekers. Nuclear input for core-collapse models. *Nuclear Physics A*, 777:395–423, October 2006.
- [109] M. M. May and R. H. White. Hydrodynamic Calculations of General-Relativistic Collapse. *Physical Review*, 141:1232–1241, January 1966.

- [110] D. L. Meier, R. I. Epstein, W. D. Arnett, and D. N. Schramm. Magnetohydrodynamic phenomena in collapsing stellar cores. *ApJ*, 204:869–878, March 1976.
- [111] O. E. B. Messer, S. W. Bruenn, J. M. Blondin, W. R. Hix, and A. Mezzacappa. Multidimensional, multiphysics simulations of core-collapse supernovae. *Journal of Physics Conference Series*, 125(1):012010–+, July 2008.
- [112] B. S. Meyer. The r-, s-, and p-Processes in Nucleosynthesis. *ARA&A*, 32:153–190, 1994.
- [113] A. Mezzacappa. ASCERTAINING THE CORE COLLAPSE SUPERNOVA MECHANISM: The State of the Art and the Road Ahead. *Annual Review of Nuclear and Particle Science*, 55:467–515, December 2005.
- [114] H. Mikami, Y. Sato, T. Matsumoto, and T. Hanawa. Three-dimensional Magnetohydrodynamical Simulations of a Core-Collapse Supernova. *ApJ*, 683:357–374, August 2008.
- [115] R. Mönchmeyer and E. Müller. Core collapse with rotation and neutron star formation. In H. Ögelman & E. P. J. van den Heuvel, editor, *Timing Neutron Stars*, pages 549–+, 1989.
- [116] T. C. Mouschovias and E. V. Paleologou. Magnetic braking of an aligned rotator during star formation - an exact, time-dependent solution. *ApJ*, 237:877–899, May 1980.
- [117] T. C. Mouschovias and E. V. Paleologou. The angular momentum problem and magnetic braking during star formation - Exact solutions for an aligned and a perpendicular rotator. *Moon and Planets*, 22:31–45, February 1980.
- [118] B. Müller, H. Dimmelmeier, and E. Müller. Exploring the relativistic regime with Newtonian hydrodynamics. II. An effective gravitational potential for rapid rotation. *A&A*, 489:301–314, October 2008.
- [119] J. W. Murphy and A. Burrows. Criteria for Core-Collapse Supernova Explosions by the Neutrino Mechanism. *ApJ*, 688:1159–1175, December 2008.
- [120] S. Nishimura, K. Kotake, M.-a. Hashimoto, S. Yamada, N. Nishimura, S. Fujimoto, and K. Sato. r-Process Nucleosynthesis in Magnetohydrodynamic Jet Explosions of Core-Collapse Supernovae. *ApJ*, 642:410–419, May 2006.
- [121] Sebastian Noelle, Yulong Xing, and Chi-Wang Shu. High-order well-balanced finite volume weno schemes for shallow water equation with moving water. *Journal of Computational Physics*, 226(1):29 – 58, 2007.
- [122] M. Obergaulinger, M. A. Aloy, and E. Müller. Axisymmetric simulations of magneto-rotational core collapse: dynamics and gravitational wave signal. *A&A*, 450:1107–1134, May 2006.
- [123] M. Obergaulinger, P. Cerdá-Durán, E. Müller, and M. A. Aloy. Semi-global simulations of the magneto-rotational instability in core collapse supernovae. *A&A*, 498:241–271, April 2009.

- [124] J. P. Ostriker and J. E. Gunn. Do Pulsars Make Supernovae? *ApJ*, 164:L95+, March 1971.
- [125] C. D. Ott, A. Burrows, T. A. Thompson, E. Livne, and R. Walder. The Spin Periods and Rotational Profiles of Neutron Stars at Birth. *ApJS*, 164:130–155, May 2006.
- [126] U.-L. Pen, P. Arras, and S. Wong. A free, fast, simple, and efficient total variation diminishing magnetohydrodynamic code. *ApJS*, 149:447–455, December 2003.
- [127] Albino Perego. A spectral neutrino leakage scheme. in preparation.
- [128] M. E. Pessah and D. Psaltis. The Stability of Magnetized Rotating Plasmas with Superthermal Fields. *ApJ*, 628:879–901, August 2005.
- [129] M. M. Phillips. The absolute magnitudes of Type IA supernovae. *ApJ*, 413:L105–L108, August 1993.
- [130] B. Povh, K. Rith, C. Scholz, and F. Zetsche. *Povh, B: Teilchen und Kerne.: Eine Einführung in die physikalischen Konzepte*. Springer-Lehrbuch. Springer, 2004.
- [131] W. H. Press, S. A. Teukolsky, W. T. Vetterling, and B. P. Flannery. *Numerical recipes in FORTRAN. The art of scientific computing*. Cambridge: University Press, 2nd edition, 1992.
- [132] R. Rabenseifner, G. Hager, and G. Jost. Hybrid mpi/openmp parallel programming on clusters of multi-core smp nodes. In *Parallel, Distributed and Network-based Processing, 2009 17th Euromicro International Conference on*, pages 427–436, feb. 2009.
- [133] P. L. Roe. Approximate riemann solvers, parameter vectors, and difference schemes. *J. Comput. Phys.*, 43(2):357–372, October 1981.
- [134] Roe, P. L. and Balsara, D. S. Notes on the eigensystem of magnetohydrodynamics. *SIAM Journal on Applied Mathematics*, 56(1):57–67, feb 1996.
- [135] Benedict D. Rogers, Alistair G. L. Borthwick, and Paul H. Taylor. Mathematical balancing of flux gradient and source terms prior to using roe’s approximate riemann solver. *Journal of Computational Physics*, 192(2):422 – 451, 2003.
- [136] James A. Rossmannith. An unstaggered, high-resolution constrained transport method for magnetohydrodynamic flows. *SIAM J. Sci. Comput.*, 28(5):1766–1797, 2006.
- [137] Y. Saad. *Iterative methods for sparse linear systems*. Society for Industrial and Applied Mathematics, 2003.
- [138] I. Sagert, T. Fischer, M. Hempel, G. Pagliara, J. Schaffner-Bielich, A. Mezzacappa, F.-K. Thielemann, and M. Liebendörfer. Signals of the QCD Phase Transition in Core-Collapse Supernovae. *Physical Review Letters*, 102(8):081101–+, February 2009.
- [139] L. Scheck, H.-T. Janka, T. Foglizzo, and K. Kifonidis. Multidimensional supernova simulations with approximative neutrino transport. II. Convection and the advective-acoustic cycle in the supernova core. *A&A*, 477:931–952, January 2008.

- [140] S. Scheidegger, R. Käppeli, S. C. Whitehouse, T. Fischer, and M. Liebendörfer. The influence of model parameters on the prediction of gravitational wave signals from stellar core collapse. *A&A*, 514:A51+, May 2010.
- [141] Simon Scheidegger. *Gravitational waves from 3D MHD core-collapse supernova simulations with neutrino transport*. PhD thesis, University of Basel, 2010.
- [142] H.R. Schwarz and N. K. ”ockler. *Numerische Mathematik*. Teubner, 2006.
- [143] Susana Serna. A characteristic-based nonconvex entropy-fix upwind scheme for the ideal magnetohydrodynamic equations. *J. Comput. Phys.*, 228(11):4232 – 4247, 2009.
- [144] S.L. Shapiro and S.A. Teukolsky. *Black holes, white dwarfs, and neutron stars: the physics of compact objects*. Physics textbook. Wiley, 1983.
- [145] M. Shibata, Y. T. Liu, S. L. Shapiro, and B. C. Stephens. Magnetorotational collapse of massive stellar cores to neutron stars: Simulations in full general relativity. *Phys. Rev. D*, 74(10):104026–+, November 2006.
- [146] Chi-Wang Shu and Stanley Osher. Efficient implementation of essentially non-oscillatory shock-capturing schemes, ii. *J. Comput. Phys.*, 83(1):32–78, July 1989.
- [147] C. Sneden, J. J. Cowan, and R. Gallino. Neutron-Capture Elements in the Early Galaxy. *ARA&A*, 46:241–288, September 2008.
- [148] James M. Stone, Thomas A. Gardiner, Peter Teuben, John F. Hawley, , and Jacob B. Simon. Athena: A new code for astrophysical mhd. *ApJS*, 178(1):137–177, 2008.
- [149] G. Strang. On the construction and comparison of difference schemes. *SIAM J. Num. Anal.*, 5:506, 1968.
- [150] P. K. Sweby. High resolution schemes using flux limiters for hyperbolic conservation laws. *SIAM Journal on Numerical Analysis*, 21(5):995–1011, 1984.
- [151] E. M. D. Symbalisty. Magnetorotational iron core collapse. *ApJ*, 285:729–746, October 1984.
- [152] M. Takahara and K. Sato. Phase Transitions in the Newly-Born Neutron Star and Neutrino Emissions from SN1987A. *Progress of Theoretical Physics*, 80:861–867, November 1988.
- [153] T. Takiwaki, K. Kotake, S. Nagataki, and K. Sato. Magneto-driven Shock Waves in Core-Collapse Supernovae. *ApJ*, 616:1086–1094, December 2004.
- [154] T. Takiwaki, K. Kotake, and K. Sato. Special Relativistic Simulations of Magnetically Dominated Jets in Collapsing Massive Stars. *ApJ*, 691:1360–1379, February 2009.
- [155] J.-L. Tassoul. *Stellar Rotation*. 2007.
- [156] R. Teyssier, S. Fromang, and E. Dormy. Kinematic dynamos using constrained transport with high order Godunov schemes and adaptive mesh refinement. *Journal of Computational Physics*, 218:44–67, October 2006.

- [157] C. Thompson and R. C. Duncan. The Soft Gamma Repeaters as Very Strongly Magnetized Neutron Stars. II. Quiescent Neutrino, X-Ray, and Alfvén Wave Emission. *ApJ*, 473:322–+, December 1996.
- [158] E. F. Toro, M. Spruce, and W. Speares. Restoration of the contact surface in the HLL-Riemann solver. *Shock Waves*, 4:25–34, July 1994.
- [159] Eleuterio F. Toro. *Riemann Solvers and Numerical Methods for Fluid Dynamics. A Practical Introduction*. Springer-Verlag GmbH, 1997.
- [160] M. Torrilhon and M. Fey. Constraint-preserving upwind methods for multidimensional advection equations. *SIAM J. Num. Anal.*, 42(4):1694–1728, 2004.
- [161] G. Tóth. The $\nabla \cdot \mathbf{b} = 0$ constraint in shock-capturing magnetohydrodynamics codes. *J. Comput. Phys.*, 161:605–652, July 2000.
- [162] U. Trottenberg, C.W. Oosterlee, and A. Schüller. *Multigrid*. Academic Press, 2001.
- [163] M. Turatto. Classification of Supernovae. In K. Weiler, editor, *Supernovae and Gamma-Ray Bursters*, volume 598 of *Lecture Notes in Physics*, Berlin Springer Verlag, pages 21–36, 2003.
- [164] D. A. Uzdensky and A. I. MacFadyen. Stellar Explosions by Magnetic Towers. *ApJ*, 647:1192–1212, August 2006.
- [165] Bram van Leer. Towards the ultimate conservative difference scheme. v. a second-order sequel to godunov’s method. *J. Comput. Phys.*, 32(1):101–136, July 1979.
- [166] Marcel Vinokur. An analysis of finite-difference and finite-volume formulations of conservation laws. *J. Comput. Phys.*, 81:1–52, 1989.
- [167] L. Wang, D. A. Howell, P. Höflich, and J. C. Wheeler. Bipolar Supernova Explosions. *ApJ*, 550:1030–1035, April 2001.
- [168] L. Wang and J. C. Wheeler. Spectropolarimetry of Supernovae. *ARA&A*, 46:433–474, September 2008.
- [169] L. Wang, J. C. Wheeler, P. Höflich, A. Khokhlov, D. Baade, D. Branch, P. Challis, A. V. Filippenko, C. Fransson, P. Garnavich, R. P. Kirshner, P. Lundqvist, R. McCray, N. Panagia, C. S. J. Pun, M. M. Phillips, G. Sonneborn, and N. B. Suntzeff. The Axisymmetric Ejecta of Supernova 1987A. *ApJ*, 579:671–677, November 2002.
- [170] N. N. Weinberg and E. Quataert. Non-linear saturation of g-modes in proto-neutron stars: quieting the acoustic engine. *MNRAS*, 387:L64–L68, June 2008.
- [171] J. C. Wheeler, D. L. Meier, and J. R. Wilson. Asymmetric Supernovae from Magnetocentrifugal Jets. *ApJ*, 568:807–819, April 2002.
- [172] J. C. Wheeler, I. Yi, P. Höflich, and L. Wang. Asymmetric Supernovae, Pulsars, Magnetars, and Gamma-Ray Bursts. *ApJ*, 537:810–823, July 2000.
- [173] Gerald Beresford Whitham. *Linear and Nonlinear Waves (Pure and Applied Mathematics)*. Wiley-Interscience, 1974.

- [174] Christian Winteler. *Light Element Production in the Big Bang and the Synthesis of Heavy Elements in 3D MHD Jets from Core-Collapse Supernovae*. PhD thesis, University of Basel, 2011.
- [175] S. E. Woosley and J. S. Bloom. The Supernova Gamma-Ray Burst Connection. *ARA&A*, 44:507–556, September 2006.
- [176] S. E. Woosley and A. Heger. The Progenitor Stars of Gamma-Ray Bursts. *ApJ*, 637:914–921, February 2006.
- [177] S. E. Woosley, A. Heger, and T. A. Weaver. The evolution and explosion of massive stars. *Reviews of Modern Physics*, 74:1015–1071, November 2002.
- [178] S. E. Woosley and T. A. Weaver. The physics of supernova explosions. *ARA&A*, 24:205–253, 1986.
- [179] Yulong Xing and Chi-Wang Shu. High order finite difference weno schemes with the exact conservation property for the shallow water equations. *Journal of Computational Physics*, 208(1):206 – 227, 2005.
- [180] A. Yahil. Self-similar stellar collapse. *ApJ*, 265:1047–1055, February 1983.
- [181] S. Yamada and H. Sawai. Numerical Study on the Rotational Collapse of Strongly Magnetized Cores of Massive Stars. *ApJ*, 608:907–924, June 2004.
- [182] H.C Yee, N.D Sandham, and M.J Djomehri. Low-dissipative high-order shock-capturing methods using characteristic-based filters. *Journal of Computational Physics*, 150(1):199 – 238, 1999.

Curriculum Vitae

Personal Details

Name	Roger Käppeli
Date of birth	22.11.1983
Citizenship	Swiss
Place of origin	Wynau/BE (CH)

Education

2008 - 2011	PhD in Theoretical Physics University of Basel, Switzerland Thesis: <i>Numerical Methods for 3D Magneto-Rotational Core-Collapse Supernova Simulation with Jet Formation</i>
2002 - 2008	Master of Science in Physics University of Basel, Switzerland Thesis: <i>3D Hydrodynamics with Adaptive Mesh for Supernova Models</i>
1999 - 2002	Baccalauréat (Swiss Highschool Diploma) Lycée cantonal de Porrentruy, Switzerland

During my studies I heard lectures by the following people:

G. Baur, B. Binggeli, C. Bruder, H. Burkhardt, R. Buser, S. Goedecker, M. Grote, K. Hencken, H.-J. Hug, H.-C. Im Hof, E. Kolbe, B. Krusche, M. Liebendörfer, D. Loss, C. Luchsinger, D. Masser, E. Meyer, E. Parlow, T. Rauscher, C. Schönberger, I. Sick, L. Tauscher, F.-K. Thielemann, D. Trautmann

Acknowledgements

The results obtained in this dissertation would not have been possible without the close collaboration and support of a variety of persons. My thanks go to

- Prof. Dr. M. Liebendoerfer (University of Basel) for advising the course of my PhD thesis, his steady support and encouragement.
- Prof. F.-K. Thielemann (University of Basel) for co-supervising my dissertation and giving me the possibility to do this thesis in the very stimulating working environment of the Astroparticle group.
- Prof. Dr. S. Mishra (ETH Zürich) for the newly established collaboration from which I could profit extensively. Furthermore, I appreciate his willingness to be the external expert for my dissertation.
- C. Winteler who was willing to post-process my data.
- A. Perego for providing me his sophisticated leakage scheme and the support whenever I needed it.
- Dr. S. Scheidegger & U. Frischknecht (University of Basel) for loads of useful and useless discussions. It was a unique time of sharing with them an apartment for three years at Oetlingerstasse 194, 4057 Basel.
- N. Vasset for the proof-reading of some parts of this thesis.
- the National Foundation for granting financial support for my PhD project.
- Dr. T. Fischer, PD Dr. A. Aste, Dr. C. von Arx, PD Dr. T. Rauscher, Dr. S.C. Withehouse, present and past members of the Astroparticle group of the University of Basel, for a cordial work ambiance.
- J. Biddiscombe (Swiss Supercomputing Center CSCS) for his support on computational issues, the visualization of simulations and related topics.
- Comp-Star, a research networking programme of the European Science Foundation.
- my family for the constant, altruistic support.